

## DOCTOR OF PHILOSOPHY

### Computer simulation studies of frustrated spin systems

Kumar, Ravinder

*Award date:*  
2019

*Awarding institution:*  
Coventry University  
Universität Leipzig

[Link to publication](#)

#### **General rights**

Copyright and moral rights for the publications made accessible in the public portal are retained by the authors and/or other copyright owners and it is a condition of accessing publications that users recognise and abide by the legal requirements associated with these rights.

- Users may download and print one copy of this thesis for personal non-commercial research or study
- This thesis cannot be reproduced or quoted extensively from without first obtaining permission from the copyright holder(s)
- You may not further distribute the material or use it for any profit-making activity or commercial gain
- You may freely distribute the URL identifying the publication in the public portal

#### **Take down policy**

If you believe that this document breaches copyright please contact us providing details, and we will remove access to the work immediately and investigate your claim.

COVENTRY UNIVERSITY  
LEIPZIG UNIVERSITY

DOCTORAL THESIS

---

# Computer simulation studies of frustrated spin systems

---

*Directors of study:*  
Dr. Martin Weigel

*Author:*  
Ravinder Kumar

Prof. Dr. Wolfhard Janke

*Supervisor:*  
Dr. Nikolaos Fytas

A THESIS SUBMITTED IN PARTIAL FULFILMENT OF THE REQUIREMENTS  
FOR THE DEGREE OF DOCTOR OF PHILOSOPHY/DOCTOR RERUM  
NATURALIUM

IN THE

FACULTY OF PHYSICS AND EARTH SCIENCES, LEIPZIG UNIVERSITY  
AND

FACULTY OF ENGINEERING, ENVIRONMENT AND COMPUTING,  
COVENTRY UNIVERSITY

May 1, 2019



Some materials have been removed from this thesis due to Third Party Copyright. Pages where material has been removed are clearly marked in the electronic version. The unabridged version of the thesis can be viewed at the Lanchester Library, Coventry University



# Computer simulation studies of frustrated spin systems

Der Fakultät für Physik und Geowissenschaften

der Universität Leipzig

eingereichte

DISSERTATION

zur Erlangung des akademischen Grades

Doktorgrade doctor rerum naturalium

Dr. rer. nat.

vorgelegt

von M.Sc. Ravinder Kumar

geboren am 01.04.1983 in Solan (Indien)

Leipzig, den May 1, 2019



## **Statement of Authorship**

I Ravinder Kumar, declare that this thesis titled, 'Computer simulation studies of frustrated spin systems' and the work presented in it are my own. I confirm that:

- This work was done while in candidature for a cotutelle research degree at Coventry University and Leipzig University.
- Where any part of this thesis has previously been submitted for a degree or any other qualification at this University or any other institution, this has been clearly stated.
- Where I have consulted the published work of others, this is always clearly attributed.
- Where I have quoted from the work of others, the source is always given. With the exception of such quotations, this thesis is entirely my own work.
- I have acknowledged all main sources of help.
- Where the thesis is based on work done by myself jointly with others, I have made clear exactly what was done by others and what I have contributed myself.

Some materials have been removed from this thesis due to Third Party Copyright. Pages where material has been removed are clearly marked in the electronic version. The unabridged version of the thesis can be viewed at the Lanchester Library, Coventry University





## **Certificate of Ethical Approval**

Applicant:

Ravinder Kumar

Project Title:

Computer simulation of spin glasses

This is to certify that the above named applicant has completed the Coventry University Ethical Approval process and their project has been confirmed and approved as Low Risk

Date of approval:

27 August 2015

Project Reference Number:

P36229



This thesis is dedicated to my wife and children.

**Bibliographische Beschreibung:**

Kumar, Ravinder

Computer simulation studies of frustrated spin systems

Universität Leipzig, Dissertation

115 S., 225 Lit., 47 Abb.

**Referat:**

Das Zufallsfeld-Potts-Modell und das Spin-Glass-Modell sind zwei prominente Beispiele für NP-schwere Probleme in der statistischen Physik. Wegen des Mangels an effizienten Berechnungsmethoden wurde das Zufallsfeld-Potts-Modell noch nicht im Detail untersucht. In der vorgelegten Arbeit entwickeln wir einen Algorithmus zur Untersuchung von Potts-Modellen mit Zufallsfeld unter Verwendung einer Graph-Cut-Methode. Es garantiert nicht den Grundzustand, aber tiefliegenden Zustände können signifikant schneller gefunden werden. Die Übereinstimmung mit dem Grundzustand beträgt mehr als 80%. Es gibt einige Behauptungen, dass unter-frustrierte zweidimensionale Spin-Glas-Systeme eine Spin-Glas-Phase bei endlicher Temperatur haben könnten. Um dieses Modell zu untersuchen, führen wir zunächst eine Implementierung des "parallel tempering" und Houdayer-Cluster-Algorithmus auf GPUs ein. Die Simulationsergebnisse weisen darauf hin, dass das unterfrustrierte Spin-Glas zur selben Universalklasse gehört wie das stochastische Spin-Glas und es keine Spin-Glas-Phase bei endlicher Temperatur gibt.

**Abstract:**

The random-field Potts model and spin-glass models are two prominent examples of NP-hard problem in statistical physics. If investigated numerically, extensive computer simulations are required to study these models. Because of the lack of efficient computational methods, the random-field Potts model has not been studied broadly yet. Here we develop an algorithm to study the random-field Potts model using a graph-cut method. It does not guarantee to find a ground state but the lowest states can be found very efficiently. We also determined the overlap of the lowest states found by the graph-cut method with the ground states found by a parallel tempering method. It is found that the lowest states found by the graph cut method have more than 80% overlap with the ground states. For the larger system sizes, the graph-cut method is much more efficient than parallel tempering method. Two-dimensional Edward-Anderson spin-glass model has been examined broadly in many previous studies. Here we focus on the phase transition of under-frustrated spin-glasses with Gaussian and bimodal couplings. There are some claims that under-frustrated two-dimensional spin-glass systems might have a spin-glass phase at finite temperatures. To study this model, we first introduce an implementation of parallel tempering and a cluster update on GPUs. The simulation results give hints that the under-frustrated spin-glass belongs to the same universality class as stochastic spin-glass and there exists no spin-glass phase at finite temperature.

## Acknowledgements

Foremost, I would like to express my sincere gratitude to my PhD advisors Dr Martin Weigel and Prof. Wolfhard Janke for the continuous support of my study and research, for their patience, motivation, enthusiasm, and immense knowledge. Their guidance helped me in all the time of study and writing of this thesis. This project would not have been possible without your continuous support throughout these years. Besides my advisors, I would also like to thank my second advisor Dr Nikos Fytas for constant support and motivation. Many thanks to Coventry University, Leipzig University and the German-French Graduate College "Statistical Physics of Complex Systems" which funded this project.

My gratitude also goes to Henrik Christiansen, Chirag Saraswati, Robin de Regt for proofreading of my thesis. My sincere thanks to people who were involved in my research projects for their support and discussions: Manoj Kumar, Prof. Sanjay Puri, Prof. Varsha Banerjee and Sanjay Kumar. Many thanks to my friend and colleague Dr Eren Metin Elçi and Dr Jonathan Gross, who invested a lot of time to discuss physics and computational techniques with me and has been constantly motivating me during my PhD. I had the chance to work with lovely people from Coventry and Leipzig with whom I discussed Physics and all other matters of the world during all these years. I would like to thank my PhD fellows from Coventry and Leipzig who were supportive all the time: Robin de Regt, Anthony Rouquier, Gerasimos Politis, Joseph Yose, Dr Suman Majumder, Hamid Khoshbakht, Henrik Christiansen, Fabio Müller, Sanjay Singh, Dr Emilio J. Flores, Dr Thierry, Platini, Dr Bogdan Teaca.

I am grateful to my family for the support, especially my wife Andrea Keßler and my children Himani and Taran who had to spend a lot of time without me. I am also thankful to my parents Manohar Lal and Meena Gautam for supporting me during my PhD.



# List of Figures

2.1	A sketch of a phase diagram for random-field Ising model . . . . .	12
2.2	A sketch of a phase diagram for random-field Potts model . . . . .	15
2.3	De Almeida-Thouless (dAT) line . . . . .	19
2.4	Replica symmetry breaking . . . . .	20
2.5	Schematic representation of replica symmetry breaking. . . . .	22
3.1	Schematic diagram of energy histogram overlap . . . . .	31
3.2	Tunnelling events vs $L/N_T$ . . . . .	31
3.3	Tunnelling time equilibration . . . . .	32
3.4	Optimal values of $N_T/\phi$ vs. $L$ . . . . .	33
3.5	A lattice in spin-overlap space . . . . .	35
4.1	Moore's law . . . . .	38
4.2	Schematic diagram of NVIDIA graphics processing unit (GPUs) . . .	39
4.3	Schematic diagram of a thread block of graphics processing unit (GPU)	41
4.4	Mapping of two replicas ( $C_1, C_2$ ) onto one replica ( $C_{12}$ ) in overlap space. . . . .	42
4.5	Benchmarking results of simulations on graphics processing units . .	44
4.6	Simulation for 2d spin-glass with bimodal couplings on graphics processing units (GPUs) . . . . .	46
4.7	Simulation of 2d spin-glass with Gaussian couplings on graphics processing unit (GPU) . . . . .	47
4.8	Simulations 3d spin-glass with bimodal couplings on graphics processing units (GPUs) . . . . .	48
4.9	The cost of parallel tempering calculated per spin. . . . .	49

5.1	Schematic diagram for bench-marking ground state of random-field Potts model from parallel tempering simulations . . . . .	55
5.2	Onset times $t_0$ for finding the ground states of the $d = 2$ random-field Potts model from parallel tempering simulations . . . . .	56
5.3	Energy histograms of final states obtained from graph-cut method . . . . .	57
5.4	Variation of the standard deviation of energy vs disorder amplitude $\Delta$ . . . . .	58
5.5	$\sigma_E$ vs. $q$ for the $d = 2$ random-field Potts model . . . . .	59
5.6	The probability of finding the ground state from graph-cut method and parallel tempering simulations . . . . .	60
5.7	Accuracy $\varepsilon$ of the ground state of random-field Potts model for graph-cut method and parallel tempering simulations . . . . .	61
5.8	Overlap between the lowest states from graph-cut method and parallel tempering simulations with ground state . . . . .	62
5.9	Run-time of the simulations for graph-cut method and parallel tempering method . . . . .	63
5.10	Run-time $r$ for determining the final state by the application of the $\alpha$ -expansion graph-cut method . . . . .	64
5.11	The breakup length . . . . .	65
6.1	Variable frustration in two dimensional spin glass . . . . .	70
6.2	Averaged minimum distance to next frustrated plaquette: (a) minimum averaged distance for $L = 16$ and (b) for $L = 32$ . . . . .	71
6.3	Logarithmic binning and equilibration . . . . .	73
6.4	Averaged energies and Binder cumulant for spin-glass system with Gaussian interactions . . . . .	75
6.5	Spin-glass susceptibility and the correlation length for spin-glass system with Gaussian interactions . . . . .	76
6.6	The defect energy from zero temperature study for spin-glass with Gaussian interactions . . . . .	77
6.7	Universality in two dimensional spin-glass with Gaussian interactions . . . . .	78
6.8	Binder cumulant scaling spin-glass with Gaussian couplings . . . . .	79
6.9	Scaling of spin-glass susceptibility with Gaussian couplings . . . . .	81
6.10	Correlation length scaling for spin-glass with Gaussian couplings . . . . .	81
6.11	Benchmarking the average energies and the Binder cumulant of spin-glass system with bimodal couplings . . . . .	83

6.12	Benchmarking the correlation and the susceptibility of spin-glass system with bimodal couplings . . . . .	84
6.13	The defect energy from zero temperature study for spin-glass with bimodal interactions. . . . .	85
6.14	Freezing temperature $T_f(L)$ as estimated from the inflection point of the correlation length. . . . .	87
6.15	Universality in bimodal spin-glass . . . . .	90
6.16	Binder cumulant collapse for bimodal spin-glass . . . . .	91
6.17	Scaling of the correlation length for the bimodal case. Figs. 6.17(a) and 6.17(b) show the data for stochastic and under-frustrated systems respectively. . . . .	92
6.18	Scaling of the spin-glass susceptibility. Figs. 6.18(a) and 6.18(b) show the data for stochastic and under-frustrated systems respectively. . . . .	93



# List of Tables

3.1	Table of fit parameters for $N_T$ and $\phi$ . . . . .	34
5.1	PT tuning parameters . . . . .	54
6.1	Collapse parameters for spin sglass system with Gaussian couplings .	80
6.2	Collapse parameters for the correlation length. . . . .	80
6.3	Collapse parameters for the spin glass susceptibility. . . . .	82
6.4	Fit variables for the freezing temperature using the logarithmic ansatz.	88
6.5	Fit variables for the freezing temperature using the logarithmic ansatz.	88
6.6	Fit variables for the freezing temperature using the power ansatz $T_f(L) = aL^{\theta_s}$ from the temperatures at inflection point. . . . .	88
6.7	Fit variables for the freezing temperature using the power ansatz . . .	89
6.8	Fit values from the Binder cumulant. . . . .	91
6.9	Fit values from the correlation length. . . . .	92
6.10	Fit values from the spin glass susceptibility. . . . .	93



# Contents

<b>1</b>	<b>Introduction</b>	<b>1</b>
1.1	Organisation and research questions . . . . .	2
<b>2</b>	<b>Theoretical background</b>	<b>5</b>
2.1	The Ising model . . . . .	5
2.1.1	Partition function . . . . .	6
2.1.2	Order of phase transition . . . . .	7
2.1.3	Observables . . . . .	7
2.1.4	Phase transitions, criticality & scaling relations . . . . .	9
2.1.5	Finite-size scaling . . . . .	10
2.2	Systems with quenched disorder . . . . .	11
2.2.1	Random-field Ising model (RFIM) . . . . .	11
2.2.1.1	Phase transition and critical behaviour . . . . .	12
2.2.2	Random-field Potts model (RFPM) . . . . .	14
2.2.2.1	Phase-transition and critical behaviour . . . . .	15
2.2.3	Spin-glass model . . . . .	16
2.2.3.1	Edwards–Anderson (EA) model . . . . .	17
2.2.3.2	Mean-field picture . . . . .	18
2.2.3.2.1	The Parisi solution . . . . .	20
2.2.3.3	The droplet picture . . . . .	23
2.3	Summary . . . . .	24

<b>3</b>	<b>Computational methods</b>	<b>25</b>
3.1	Monte-Carlo methods . . . . .	25
3.1.1	Metropolis algorithm . . . . .	26
3.1.1.1	Equilibration . . . . .	27
3.1.2	Auto-correlation times and error analysis . . . . .	27
3.2	Parallel Tempering . . . . .	28
3.2.1	Selection of the optimum set of temperatures . . . . .	30
3.3	Houdayer cluster algorithm . . . . .	34
3.4	Summary . . . . .	36
<b>4</b>	<b>Performing spin glass simulations on GPUs</b>	<b>37</b>
4.1	Hardware, optimization and implementation . . . . .	38
4.2	Verification of the physical results . . . . .	44
4.3	Performance . . . . .	45
4.3.1	Two-dimensional system with bimodal couplings . . . . .	45
4.3.2	Two-dimensional system with Gaussian couplings . . . . .	47
4.3.3	Three-dimensional system with bimodal couplings . . . . .	48
4.3.4	Parallel tempering on CPU . . . . .	49
4.4	Summary . . . . .	49
<b>5</b>	<b>Approximate ground states in the random-field Potts model</b>	<b>51</b>
5.1	Model and methodology . . . . .	51
5.1.1	Random-field Potts model . . . . .	52
5.1.2	Graph-cut method . . . . .	53
5.1.3	Parallel-tempering . . . . .	54
5.2	Benchmarks . . . . .	56
5.2.1	Approximate ground states from GC . . . . .	57
5.2.2	Comparisons with PT . . . . .	59
5.2.3	Run times and computational complexity . . . . .	62
5.3	Scaling of the breakup length . . . . .	65
5.4	Summary . . . . .	66

<b>6</b>	<b>Spin glass with variable frustration</b>	<b>69</b>
6.1	Under and over-frustrated spin glass . . . . .	69
6.2	Observables . . . . .	72
6.3	Simulation parameters and equilibration . . . . .	74
6.4	Under-frustrated spin glass with Gaussian interactions . . . . .	74
6.4.1	Benchmarking the physical quantities . . . . .	76
6.4.2	Phase transition and scaling . . . . .	77
6.4.2.1	Defect energy . . . . .	77
6.4.2.2	Finite size scaling (FSS) analysis . . . . .	77
6.5	Under-frustrated spin glass with bimodal couplings . . . . .	82
6.5.1	Benchmarking the physical quantities . . . . .	83
6.5.2	Phase transition and scaling . . . . .	85
6.5.2.1	Defect energy . . . . .	85
6.5.2.2	The freezing temperature . . . . .	86
6.5.2.3	Finite size scaling (FSS) analysis . . . . .	89
6.6	Summary . . . . .	93
<b>7</b>	<b>Conclusions</b>	<b>95</b>



# Chapter 1

## Introduction

Understanding the static and dynamic properties of complex physical systems is a highly challenging problem of current research in physics, chemistry and biology. Spin-glasses and structural glasses are prominent examples of complex systems in condensed matter physics. Computational developments in biophysics increased the applicability of statistical models normally used in physics to biology. One of the most prominent examples of complex systems in biology is the protein folding problem. Concepts in physics describing the behaviour of spin-glasses are similar, however biological systems show a huge diversity. Still, all these models have a rugged energy landscape and many joint features, which make a common statistical treatment promising for current and future scientific developments. In this thesis, different models of magnetic systems exhibiting disorder are investigated. Why is one interested in studying such systems? There are not many perfect crystals in nature, therefore, to explain experiments on real materials requires understanding the effect of disorders. Moreover, there are phenomena in disordered systems which are absent in the perfect crystals.

The two main models studied in this thesis are random-field Potts model and spin-glass model. However, gaining the fundamental understanding of these systems is an arduous task. Spin-glasses help us understand many very hard real world problems in everyday life and nature. The atoms in a window glass seem to be disordered. There are many fundamental questions, like, why is a window glass solid? The spin-glass model plays a significant role in understanding gaps in solid state physics. There are many other systems which can be described mathematically by the spin-glass model, e.g. protein folding, optimisation problems etc. The random-field spin models also play a vital role in understanding the criticality and phase transition in alloys. In the same way as spin-glass, applications of the random-field model also exist in many other fields like optimisation problems in computer science or condensed matter. Therefore understanding these systems would help in understanding many puzzles in the real world.

Disordered systems are very hard to understand theoretically. Therefore computational methods are used to study the phase transitions and other physical properties of such systems. In section 1.1, organisation and research questions raised in this dissertation are discussed.

## 1.1 Organisation and research questions

The theory of disordered systems is a topic of research by itself, and there are many well-established methods which have been accepted widely by researchers. In Chap. 2, the theoretical background is discussed. Theories which describe spin-glass and random-field spin models are discussed from the point of view of computational and statistical physics. In this thesis, topics like criticality, phase transitions and the ground state of the spin systems etc. are investigated. Therefore, these topics are addressed in detail, and their relation to research questions is established. It is challenging to tackle these systems mathematically. Therefore, this thesis makes use of a well established computational method for these studies. In Chap. 2, computational methods are introduced. The simulations are done using Monte-Carlo methods. Algorithms like Metropolis, parallel tempering and spin-glass specific cluster algorithm (Houdayer cluster algorithm) are briefly introduced.

The first research question is discussed in Chap. 4. It was mentioned earlier that it is a very complicated task to tackle disordered systems theoretically. However, the simulations of such systems are also computational very demanding. The current state of computers allows for the simulation of only systems of certain, but finite lattice sizes. This introduces finite size effects in these studies. Therefore, there is a need to study larger system sizes. The system size is not the only problem associated with these simulations. Disordered systems require a large number of computer cores, and the simulated quantities have to be averaged over many disorder realisations to get reliable physical results.

The number of computer cores available, and the time required to simulate such systems grow with the system size. Moreover, the larger the system size, the longer one needs to simulate for equilibration. Therefore, one requires new computational approaches to study such systems. One of the new methods is the use of Graphics Processing Units (GPUs) for simulations. In recent years, the use of GPUs for simulations is continuously increasing. However, implementation of cluster algorithms on GPUs is still a hard task. Hence, these difficulties and a new method to simulate disordered systems on GPUs are introduced in Chap. 4. This technique is compared with the known algorithms on GPUs and CPUs. The central question is the efficiency of the algorithm and the code with an additional question, how does the cluster-algorithm behave on GPUs?

The second research question is discussed in Chap. 5. In this chapter, the properties of the random-field Potts model are studied. The random-field Potts model has

many applications in the real world. Some notable examples are magnetic grains, an-isotropic orientational glasses, randomly diluted molecular crystals, structural transitions in SrTiO<sub>3</sub> crystals, and phase transitions in type I anti-ferromagnetic (such as NdSb, NdAs, CeAs) in a uniform field. Theoretical background of this model is given in Chap. 3.

Many aspects such as critical behaviour and finite size scaling etc. of the  $q$  state random-field Potts model are not very well understood yet. The main reason that the ground states of the random-field Potts model are not extensively studied is the NP-hardness of the problem. There is still a lack of computational methods to study such problems. Monte Carlo methods require huge computational time. This makes the study of such systems very challenging. Therefore there is a need for alternative efficient methods to study such systems. Exact methods based on graph theory, such as the graph cut method can find the ground state of the random-field Ising model exactly. Finding the ground state can help in understanding the critical behaviour and phase transitions of such systems. The current state of the information available for the random-field Potts model is not enough at understanding its thermodynamics and phases. There are very few studies which tried to do some estimates, but the studies are limited in the system size and number of disorders. Therefore, there is an interest in understanding these systems in more detail. Hence, a comparative study using parallel tempering and graph cut method is done to establish the possibility of finding the ground state of the random-field model with  $q$  states. In Chap. 5, the efficiency and quality of accuracy of the graph cut method are compared with parallel tempering.

The last research question tackled in this thesis is related to the two-dimensional spin-glass. Initially, the spin-glass model was aimed to understand some strange behaviour observed in the experiments of certain magnetic alloys. However, the theory and applicability of spin-glasses have spread to a wide range of systems with a rugged energy landscape. A two-dimensional spin-glass is one of the models used to test the efficiency of quantum annealing machines (sometimes known as quantum computers).

It is widely accepted that the two-dimensional spin-glass systems with Gaussian or Bimodal interaction have a phase transition at zero temperature. However, there are claims from re-normalisation group (RG) theory studies that if one decreases the frustration of such systems while keeping the number of anti-ferromagnetic bonds constant, a phase transition at finite temperature is observed. There are no studies to support this argument via simulations. Hence, the question arises, if such a phase transition can also be seen from Monte-Carlo simulations of under-frustrated spin-glasses. Therefore, in Chap. 6 two-dimensional under-frustrated spin-glass systems with Gaussian and bimodal interactions are examined for the phase transitions. Moreover, one can raise the question of universality. Do under-frustrated and over-frustrated spin-glass systems belong to the same universality class?

The outcomes of the research are summarised and discussed in Chap. 7.

# Chapter 2

## Theoretical background

In the introduction, it is mentioned that the core models investigated in this dissertation are spin models with disorder; particularly the random-field Potts model and the two-dimensional spin glass. The critical behaviour of these models is still not well understood. Therefore, in this dissertation, the central research topics are related to the phase transitions and critical behaviour in these systems. Before I start to discuss some specific models, I need to introduce some concepts of statistical mechanics and in particular the theory of critical phenomena.

This chapter is organised as follows. In Sec. 2.1, first a short introduction to statistical mechanics relating to the ferromagnetic Ising model is given. I briefly discuss essential observables, e.g., specific heat, susceptibility, magnetisation, correlation functions etc. I also discuss the idea of critical scaling for this particular example. In Sec. 2.2, models with the quenched disorder are introduced. The theory of random-field Ising model (RFIM), random-field Potts model (RFPM) and spin glasses (SG) in the Sec. 2.2.1, Sec. 2.2.2, Sec. 2.2.3 respectively.

### 2.1 The Ising model

Wilhelm Lenz initiated the idea of the Ising model in Ref. [1], but the model is developed and studied in detail by Ernst Ising in 1925 [2]. Since the development of the model, it is used in many fields of science. This model is exactly solvable in two-dimensions, but still captures many aspects of the statistical physics in details. This model is compelling to test algorithms and study ferromagnetic systems because of its simplicity. In the simplest case spins ( $s_i = \pm 1$ ) are situated on the sites of a  $d$ -dimensional lattice with nearest neighbour interactions. The Hamiltonian of the Ising model is given by

$$\mathcal{H} = - \sum_{\langle i,j \rangle} J_{ij} s_i s_j - \sum_i h_i s_i . \quad (2.1)$$

In Eq. (2.1)  $J_{ij} = J$  is the exchange coupling. The system is anti-ferromagnetic if the value of  $J$  is negative and ferromagnetic if  $J$  is positive. Angle brackets  $\langle i, j \rangle$  indicates that the lattice sum only runs over all the nearest-neighbour pairs implying nearest-neighbour interactions. In the second term of Eq. (2.1)  $h_i$  represents an external magnetic field.

In the absence of the external magnetic field, this model is exactly solvable in one and two dimensions. Moreover, in the one-dimensional case, it can be solved even in the presence of the magnetic field. Therefore it is also known as the "fruit fly" of statistical physics. In dimensions  $d > 1$ , one observes a phase transition from ordered to disordered state at a finite critical temperature  $T_c$ .

A quantity called the order parameter is used as a measure of the degree of order across the boundaries in a phase transition system. It is usually zero in the disordered phase and one in the ordered phase. This ordering implies that the spins are either aligned in the same direction or they randomly point in any of the possible directions. For the Ising model, the temperature-dependent phase transition can be studied by measuring the magnetisation in the ferromagnetic case. The magnetization is given by

$$m = \frac{1}{N} \sum_i s_i \quad (2.2)$$

Above the critical temperature  $T_c$ , one is in the disordered phase and spins fluctuate randomly. Hence, the average magnetisation is zero. Therefore, it serves as an order parameter which is zero in the disordered state and one in the ordered state. Before we discuss the model further, some basic concepts from statistical physics are introduced in the next section.

### 2.1.1 Partition function

To discuss the criticality and scaling theory, we need to recall some of the basic concepts of statistical physics and phase transitions [3, 4, 5, 6]. In this dissertation, we will focus only on the classical canonical ensemble i.e no quantum effects will be discussed. The partition function for this ensemble is given as

$$\mathcal{Z} = \sum_{\mathbf{s}} e^{-\beta \mathcal{H}} = e^{-\beta F}, \quad (2.3)$$

where  $\beta = 1/(k_b T)$  with  $k_b$  being Boltzmann constant and  $T$  the temperature respectively. If not mentioned otherwise, the values of  $\beta$  and  $k_b$  are set to be unity throughout this dissertation. The summation is running over all possible states of the system. The state space may be continuous or discrete.  $F$  is the free energy of the system given by

$$F = -\beta^{-1} \ln \mathcal{Z}, \quad (2.4)$$

The Hamiltonian holds the information about the short range, medium range or long range interactions. The canonical partition function is used for studying a system in thermal equilibrium, which is connected to a heat bath at some temperature  $T$ . It plays the role of a normalising constant which is independent of states, ensuring that the probabilities sum up to one.

### 2.1.2 Order of phase transition

Order parameters can be found for most systems exhibiting a phase transition. The phase transitions are normally either of 1st order or the second order. The term order originates from the number of derivatives of the free energy  $F$  before the discontinuous behaviour is observed. The free energy is a zeroth order quantity as it is always continuous. The order parameter shows a discontinuous jump at the critical point if the system exhibits a first order phase transition e.g. the latent heat. Systems which show a divergence in the second derivatives of the free energy, e.g. susceptibility, specific heat etc. are the examples of second order phase transition. In this dissertation, we only concentrate on the second order phase transition. Therefore if not mentioned a phase transition after this point means a second order phase transition and the whole theory introduced is based on second-order phase transition.

### 2.1.3 Observables

The partition function  $\mathcal{Z}$  is used to calculate the expectation values of physical quantities such as the energy, magnetic susceptibility, magnetization and specific heat. These quantities are called the observables and can be calculated as follows

$$\langle \mathcal{O} \rangle = \frac{1}{\mathcal{Z}} \sum_s \mathcal{O}(s) e^{-\beta \mathcal{H}}. \quad (2.5)$$

The sum runs over all states  $s$  in the system,  $\mathcal{Z}$  is the partition function. The partition function ( $\mathcal{Z}$ ) is used to normalize the equilibrium Boltzmann distribution

$$\mathcal{P}_{\text{eq}}(s) = \frac{1}{\mathcal{Z}} e^{-\mathcal{H}\beta}. \quad (2.6)$$

The  $\langle \dots \rangle$  in Eq. (2.5) represent a thermal average of the quantities. Now we look at the definitions of some observables of interest for the Ising model. The internal energy per site is given by  $e = E/V$  with

$$E = \langle \mathcal{H} \rangle = -\frac{1}{\mathcal{Z}} \frac{\partial \mathcal{Z}}{\partial \beta} = -\frac{\partial \ln \mathcal{Z}}{\partial \beta}, \quad (2.7)$$

and  $V$  is the volume of the lattice. The specific heat can be derived as

$$\langle \mathcal{H}^2 \rangle - \langle \mathcal{H} \rangle^2 = -\frac{\partial}{\partial \beta} \langle \mathcal{H} \rangle, \quad (2.8)$$

$$C_v = -\frac{\partial}{\partial \beta} \langle \mathcal{H} \rangle = T^2 \left( \frac{\partial E}{\partial T} \right), \quad (2.9)$$

The magnetisation  $m = M/V$  and the susceptibility  $\chi$  are defined as

$$M = \frac{1}{\beta} \frac{\partial \ln \mathcal{Z}}{\partial h} = V \langle m \rangle, \quad m = \frac{1}{V} \sum_i s_i, \quad (2.10)$$

where  $h$  is the magnetic field and

$$\chi = \beta V (\langle m^2 \rangle - \langle m \rangle^2). \quad (2.11)$$

The 4th order moment of the magnetisation is another important quantity used to study the phase transitions. This quantity is termed as the Binder cumulant.

$$g = \frac{1}{2} \left[ 3 - \frac{\langle m^4 \rangle}{\langle m^2 \rangle^2} \right], \quad (2.12)$$

The Binder cumulant  $g$  scales as  $\tilde{G}[L^{1/\nu}(T - T_c)]$  for a lattice of length  $L$ . It is clear from the definition that it is a dimensionless quantity. The different factors ensure that  $g \rightarrow 1$  for  $T \rightarrow 0$  and  $g \rightarrow 0$  for  $T \rightarrow \infty$ . The asymptotic (for large  $L$ ) scaling behaviour of the Binder ratio follows directly from the fact that the pre-factors of the moments of the magnetization ( $m^k \sim L^{k\beta/\nu}$ ) cancel out in [Eq. \(2.12\)](#).

Another significant quantity which we are interested in is the correlation between spins  $s_i$  and  $s_j$  at the lattice sites  $i$  and  $j$ . The correlation can be measured by considering correlation functions like the two-point spin-spin correlation  $G(i, j)$  given by

$$G(\mathbf{r}) = G(i, j) = \langle s_i s_j \rangle - \langle s_i \rangle \langle s_j \rangle, \quad (2.13)$$

where  $\mathbf{r} = r_i - r_j$ . At the large distances and away from criticality  $G(\mathbf{r})$  decays exponentially

$$G(\mathbf{r}) \propto e^{-|\mathbf{r}|/\tilde{\xi}}. \quad (2.14)$$

The correlation length is defined using the decay rate of  $G(\mathbf{r})$

$$\tilde{\xi} = -\lim_{|\mathbf{r}| \rightarrow \infty} \frac{|\mathbf{r}|}{G(\mathbf{r})} \quad (2.15)$$

which is directional and depends on the orientation of vector  $\mathbf{r}$ .

### 2.1.4 Phase transitions, criticality & scaling relations

The Ising model is the benchmarking model for the systems exhibiting the continuous (second order) phase transitions from ordered phase at low temperature to the disordered phase at the high temperatures. The temperature at which the phase transition occurs is called the critical temperature,  $T_c$ . At a continuous phase transition, the free energy has a singularity that usually manifests itself via a power-law behaviour of the derived observables at criticality. In case of vanishing external magnetic field, the two dimensional Ising model has been solved exactly by Onsager in Ref. [7]. For the same case, there are also methods to calculate the partition function of the Ising model exactly discussed in Ref. [8, 9]. In Ref. [10, 11], the exact magnetization is calculated in the absence of the magnetic field. The magnetic susceptibility is known to very high precision, but there exists no exact solution yet [12, 13]. The correlation length is known in arbitrary lattice directions [14, 15]. Three dimensional Ising model is not solved exactly yet, however, numerical and analytical studies of various methods provide a consistent and very precise picture.

The correlation length  $\xi$  of Eq. (2.14) gives a measure of correlations and order in a system diverges at the transition. The leading divergence of the correlation length can be parametrized as:

$$\xi = \xi'_0 |1 - T/T_c|^{-\nu} + \dots \quad (2.16)$$

with  $\nu$  a critical exponent related to this divergence.  $\xi'_0$  is the critical amplitude and it has different values above and below the critical temperature. In Eq. (2.16), the ... indicates sub-leading term and corrections.

The qualitative properties of second-order phase transition do not depend on the short range distance features of the Hamiltonian. This fact is used as the basis of the universality hypothesis in [16]. This implies that all systems with the same symmetries and same dimensionality should have the same set of critical exponents. In re-normalisation group theory certain amplitude ratios also show universal behaviour, but it is not true in general. Close enough to the phase transition (i.e.,  $|T - T_c|/T_c \ll 1$ ) because of the singularities power laws can well describe the behaviour of observables. There could also be other types of singularities, e.g. exponential divergence which could not be characterised by the power laws. The critical exponents are used to describe the behaviour around the critical point in second order phase transitions. The most important critical exponents are  $\alpha$ ,  $\beta$  and  $\gamma$ , respectively. Each exponent is associated with a physical quantity.

$$C_v = C_b + C_0 |1 - T/T_c|^{-\alpha} + \dots, \quad (2.17)$$

$$m = m_0 (1 - T/T_c)^\beta + \dots, \quad (2.18)$$

$$\chi = \chi_0 |1 - T/T_c|^{-\gamma} + \dots, \quad (2.19)$$

It is shown in [17, 18, 19, 20, 21] that the critical exponents relate to each other via some scaling identities. If the scaling relations hold, only two exponents are independent and fully describe the critical behaviour of the Ising model. The scaling relations are as follows

$$\begin{aligned}
dv &= 2 - \alpha \quad (\text{Josephson's law}), \\
2\beta + \gamma &= 2 - \alpha \quad (\text{Rushbrooke's law}), \\
\beta(\delta - 1) &= \gamma \quad (\text{Griffiths's law}), \\
\nu(2 - \eta) &= \gamma \quad (\text{Fisher's law}).
\end{aligned} \tag{2.20}$$

In Eq. (2.20),  $d$  is the dimensionality of the system and  $\delta$  and  $\eta$  are two further exponents defined exactly at the critical temperature  $T_c$  as follows

$$\begin{aligned}
m &\propto h^{1/\delta} \\
G(r) &\propto r^{-d+2-\eta}
\end{aligned} \tag{2.21}$$

### 2.1.5 Finite-size scaling

Finite-size scaling is a method of extracting values for critical exponents by observing how measured quantities vary as the size  $L$  of the system changes. This variation is caused by the finiteness of the a system studied on a lattice. On a finite lattice, we have finite number of degrees of freedom. Finite size effects cause many problems in studying physical quantities. For example, choosing a good order parameter  $m$  and  $|m|$  are both zero in infinite volume limit, but  $|m| > 0$  on a finite lattice. In Eq. (2.16), it is shown that the correlation length  $\xi$  diverges near the critical temperature. However, because of the finite size  $L$  in the simulation, the system is effectively ordered when  $\xi \rightarrow L$ . Hence, one observes so-called pseudo-critical point

$$\left( \beta_c(\infty) - \beta_C(L^d) \right)^{-\nu} \propto L \rightarrow \beta_C(L^d) = \beta_c(\infty) - c_1 L^{-\frac{1}{\nu}} \tag{2.22}$$

Usually, the value of  $\beta_C(\infty)$  is not known to us and  $c_1$  is a constant. One of the tasks now is to locate the pseudo-critical point. I will demonstrate with the example of magnetic susceptibility  $\chi$  how to locate the pseudo-critical point. The observations from the simulation show that at the pseudo-critical point  $\chi$  has a maximum.  $\chi$  diverges in infinite volume as given in Eq. (2.20). Therefore, at the pseudo-critical point, the maximum value of  $\chi$  is

$$\chi_{\max} \propto \left( \beta_C(L^d) - \beta_c(\infty) \right)^{-\gamma} \propto L^{\frac{\gamma}{\nu}} \tag{2.23}$$

Now for each system with lattice size  $L$ , the maximum can be determined and from the maximum one can use the power law ansatz (there could be other possibilities some of which are discussed in the next chapters).

$$\beta_{\max} = \beta_c - cL^x \tag{2.24}$$

There are three fit parameters in Eq. (2.24),  $\beta_c$  is the critical inverse temperature and  $x$  is equal to  $-\frac{1}{\nu}$ . One could now determine the value of  $\gamma/\nu$  from  $\chi_{\max}$ . Hence using the finite size scaling, one can determine the critical temperature and universality class with very high accuracy. Note that other dimensionless quantities, such as the two-point finite-size correlation length [22, 23] can also be used with similar results.

## 2.2 Systems with quenched disorder

Almost all materials in nature are inhomogeneous and many different kinds of impurities could be distributed randomly throughout these materials. These impurities introduce disorder in the system and if the disorder of these impurities is not weak, then the system becomes frustrated. In theory, the disorder can be either geometric, annealed or quenched. If a system has a disorder where impurities are in thermal equilibrium with the host and the partition function is calculated by summing the configuration of original components and impurities, then it is called annealed disorder. System where the impurities remain blocked in random fixed positions and do not contribute to the thermal equilibrium have the quenched disorder. Geometrical frustration is a phenomenon where atoms tend to stick to non-trivial positions and form complex structures. In this Section, we first discuss some prominent examples of systems with quenched disorder. I also discuss some of the theoretical methods used to study the statistical properties of models with quenched-disorder.

### 2.2.1 Random-field Ising model (RFIM)

In Eq. (2.1), I introduced the Hamiltonian of the Ising model. In RFIM, the couplings are set to a constant  $J_{ij} = J$  as for the Ising ferromagnet. For Ising ferromagnet the external field associated with each spin is zero. For the RFIM, the disorder is introduced through  $h_i$ . In the physical world  $h_i$  can be interpreted as a site dependent external magnetic-field acting on an Ising ferromagnet. Eq. (2.1) stays valid for random-field Ising model:

$$\mathcal{H} = -J \sum_{\langle i,j \rangle} s_i s_j - \sum_i h_i s_i. \quad (2.25)$$

RFIM is one of the simplest and an archetypal disordered system. Therefore, there has been a great theoretical interest in it and different aspects are discussed in Refs. [24, 25, 26, 27, 28, 29, 30]. There are also many studies connecting the theory to the experiments in condensed matter physics [31, 32, 33, 34, 35, 36]. Some important systems which can be studied using RFIM are: colloid-polymer mixtures [36, 37], colossal magnetoresistance oxides [38, 39], phase-coexistence in the

presence of quenched disorder [40, 41, 42], diluted antiferromagnets in a field [34], non-equilibrium phenomena e.g. Barkhausen noise in magnetic hysteresis [43, 44] and the design of switchable magnetic domains [45], etc.

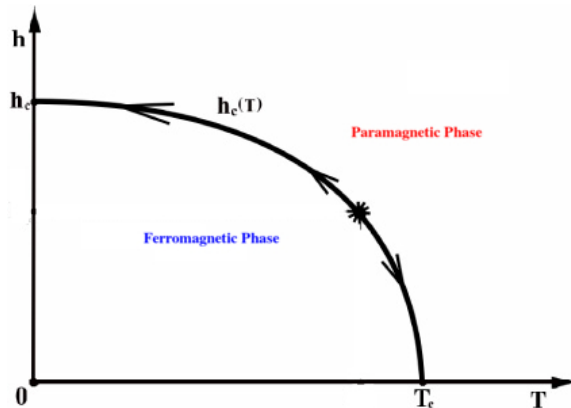


Figure 2.1: A sketch of a phase diagram for RFIM.

### 2.2.1.1 Phase transition and critical behaviour

It is discussed by Imry and Ma in Ref. [24], that there exists an ordered ferromagnetic phase for the random-field Ising model at low temperatures and weak disorder for space dimensions larger than two ( $d > 2$ ) [46, 47, 48, 49, 50]. This conclusion is used to sketch the phase diagram of the RFIM in many studies [51, 52, 53, 54, 55, 56]. There are also quantitative expressions from mean field theory to support this argument [56]. However such quantitative arguments to sketch a phase diagram from the mean-field theory are very poor approximations in general. In Fig. 2.1, a phase boundary separates the ordered ferromagnetic phase from the paramagnetic phase. This phase diagram is from re-normalisation group (RG) picture and the stable fixed point is at zero temperature. Also, the randomness axis has a critical value  $h_c$  for the random-field strength. The ordered phase starts to appear at the critical point and the system stays in the ordered phase below it, above it the paramagnetic phase is observed.

In Sec. 2.1.4, the theoretical scaling arguments are discussed for the Ising ferromagnet. In the same way the scaling ansatz is formed for RFIM. However, in the presence of the random-field disorder, the hyper-scaling relation is broken. The hyper-scaling relation refers to the class of critical-point exponent relations and is discussed in Ref. [46, 47, 48]. The paramagnetic-ferromagnetic phase transition is ruled by a fixed point at temperature  $T = 0$  [33]. The spatial dimension  $d$  in Eq. (2.20) is replaced by  $d - \theta$ , in hyper-scaling relations ( $\theta \sim d/2$ ). There are three independent exponents in  $d \leq 3$  and two independent exponents for  $d \geq 5$ . It is shown in Ref. [57] that for  $3 < d < 5$ ,  $\eta = \beta$ . Unfortunately, establishing the scaling

picture in full detail is non-trivial. In 3-dimensions, perturbation theory predicts that the ferromagnetic phase disappears for any non-zero random-field [26]. Even if the statement holds at all orders in perturbation theory [28], the ferromagnetic phase is stable in  $D = 3$  [50]. Therefore, it can be concluded that non-perturbative phenomena are at play [58, 59]. There are suggestions that spontaneous supersymmetry breaking distorts the scaling picture. It is discussed in Ref. [60] that the phase transition is described by more than two critical exponents.

Experimentally, the diluted anti-ferromagnet in an applied magnetic-field is a well-studied example [34] for RFIM. In neutron scattering, different parametrizations of the scattering line-shape yield contradictory estimates of the thermal critical exponent, namely  $\nu = 0.87(7)$  [61] and  $\nu = 1.20(5)$  [62]. Moreover, the anomalous dimension  $\eta = 0.16(6)$  [61] violates hyper-scaling bounds, if the experimental claims of a divergent specific heat [35, 63] are to be believed. It is clearly evident that a reliable parametrization of the line-shape is needed. Unfortunately, RFIM universality class is not well understood yet.

RFIM is extensively studied using numerical simulations [64, 65, 53]. However, typical Monte Carlo schemes get trapped into local minima. Therefore some sophisticated simulation methods are used in Ref. [66, 67, 68, 69, 70]. However, the curse of finite size effects is associated with these simulations. Larger system sizes can be simulated via mapping of the ground state to the maximum-flow optimization problem [71, 72, 73, 74, 75, 76, 77, 78]. However, strong violations of universality are observed in finite-size scaling analysis of the numerical data produced by these methods [79, 80, 81, 73].

The methods for determining the order of the low temperature phase transition and its dependence on the form of the field distribution have been discussed throughout the years [56, 82, 83, 84, 85, 86]. The choice of random-field distribution might effect the final results. There are many different possibilities to choose the random-field distribution. The well known examples are Gaussian distribution and bimodal distribution. It was shown in Ref. [56, 87] that the tri-critical point at the strong disorder regime is present only in the bimodal distribution. However, it was shown later in Ref. [88] that this observation was a finite-size artefact and there is no tri-critical point and no first-order transition. Even after so much effort, there is no clear picture of the critical behaviour of RFIM. Although, the view that the phase transition of the RFIM is of second-order is well accepted [76, 68, 66, 67] the notably small value of the scaling exponent  $\beta$  continues to cast some doubts. Therefore, there exists a strong debate about the role of disorder on criticality. The data available from different simulations is not able to answer the question of whether the critical exponents depend on the particular choice of the distribution for the random-fields, analogously to the mean-field theory predictions [56]. Hence, the critical behaviour of RFIM is still under intense investigation [60, 66, 67, 69, 70, 89].

RFIM is a well-studied model, but there are systems where more than two states can exist. These systems are not well studied. One such generalised model is called

the random-field Potts model. In the next section, the difficulties related to studying this model are discussed.

### 2.2.2 Random-field Potts model (RFPM)

As mentioned in the last section, the RFPM describes the systems with more than two states. Therefore, the Hamiltonian in Eq. (2.25) has to be modified appropriately. Before RFPM is discussed, I will briefly present an overview of the Potts model without disorder. The  $q$ -state Potts model can be seen as generalisation of Ising model to  $q$ -states. If one sets  $q = 2$ , the whole picture of Ising model can be captured. The Potts model has many physical realizations [90, 91]. Some applications of Potts model include soap froths, cellular tissues, grain growth, nucleation, static and dynamic recrystallization, etc. However, the real physical picture requires disorder to be incorporated in such systems for their accurate description. Therefore, a more appropriate model in this context is the generalization of the  $q$ -state Potts model with disorder or the  $q$ -state random-field Potts model (RFPM). Experimentally, the RFPM can describe magnetic grains, anisotropic orientational glasses, randomly diluted molecular crystals [92, 93], structural transitions in SrTiO<sub>3</sub> crystals [94], and the phase transitions in type I antiferromagnets (such as Ndsb, NdAs, CeAs) in a uniform field [95]. Similarly to the RFIM, the presence of random-fields in RFPM (or disorder  $\Delta$ ) poses difficulties, both analytically and computationally, due to the complex free energy landscape arising from the  $q$ -spin states and their coupling with quenched randomness. The Hamiltonian of RFPM can be written as:

$$\mathcal{H} = -J \sum_{\langle ij \rangle} \delta_{s_i, s_j} - \sum_i \sum_{\alpha=0}^{q-1} h_i^\alpha \delta_{s_i, \alpha}, \quad (2.26)$$

where  $\delta_{x,y}$  is the Kronecker delta function and  $q$  is the total number of labels or the Potts state. Each spin  $s_i$  can take any of the possible  $q$ -values in the set  $s_i = \{0, 1, \dots, q-1\}$ .  $h_i^\alpha$  are the quenched random-field variables at site  $i$  acting on the state  $\alpha$ . We define  $h_i^\alpha = \Delta \epsilon_i^\alpha$ , where the parameter  $\Delta$  is a measure of the disorder strength. The variables  $\epsilon_i^\alpha$  are drawn from a chosen distribution e.g. bimodal or Gaussian. The parameter  $\Delta$  is a measure of disorder strength in the system. There is also an alternative to the Hamiltonian in Eq. (2.26):

$$\mathcal{H} = -J \sum_{\langle ij \rangle} \delta_{s_i, s_j} - \Delta \sum_i \delta_{s_i, h_i}. \quad (2.27)$$

The main difference in Eq. (2.26) and Eq. (2.27) is the interaction of the external magnetic-field with the spin. The detailed description of the interactions will be given in chapter 5. The Hamiltonian in Eq. (2.26) has a unique ground state, whereas the ground state of the alternative Hamiltonian in Eq. (2.27) has degeneracy.

### 2.2.2.1 Phase-transition and critical behaviour

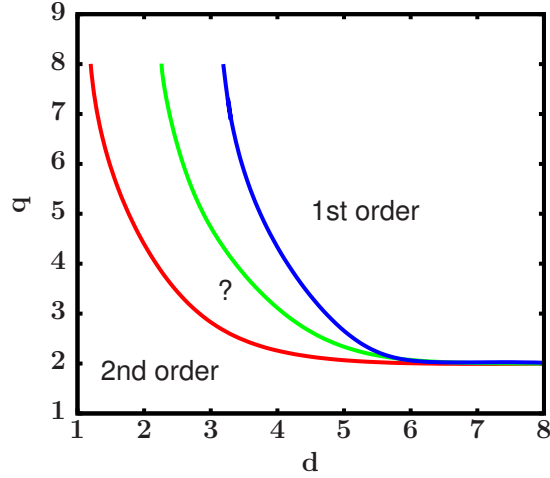


Figure 2.2: A sketch of a phase diagram for RFPM.  $q$  represents the states of RFPM and  $d$  denotes the physical dimensions. The red and blue line show two different possibilities of phase transition predicted by different studies. The green line is a hypothetical correct (yet unknown) transition line.

The nature of phases and phase transitions from the ferromagnetic to the disordered phase for RFPM are not well understood. There are two different planes of phase diagrams which one could try to understand. One is the  $q$ - $\Delta$  plane, where one attempts to understand how the number of states and the disorder strength affects the phase. The other plane is the  $(T, \Delta)$ -plane, where the effect of temperature and disorder strength can be studied.

The  $q$ -state RFPM is not extensively studied in the literature. However, there are some preliminary studies in Ref. [96, 97, 98, 99, 100]. These have primarily investigated the phase diagram in  $(T, \Delta)$ -space for different  $q$  and  $d$  values. The analytical approaches have generally used mean-field techniques, while the computational approaches are based on Monte-Carlo methods. The Potts model without disorder can be used for comparative studies, therefore first I first discuss the Potts model. In  $d = 2$ , the  $q$ -state PM has a second-order phase transition for  $q \leq 4$ , and a first-order transition for  $q > 4$  [101]. In  $d = 3$ , on the other hand, there is a first-order transition for  $q \geq 3$ . A detailed study of the  $q$ -state RFPM in  $d = 3$  is performed by Eichhorn and Binder using MC simulations [98, 99]. They found that the random-fields turn the first-order transition of the  $q$ -state Potts model into a second-order transition if the disorder is large. They proposed a qualitative scenario in the  $(q, d)$ -plane which exhibited a shift of the tri-critical curves  $q_c(d)$  to higher values, consistent with the mean-field predictions of Blankschtein et al. [96].

In the study by Eichhorn and Binder, the values of  $q < q_c(d)$  yielded a second-order transition, while  $q > q_c(d)$  led to a first-order transition. From their study, the

3-state RFPM (and probably the 4-state RFPM) exhibited a second-order transition with increasing disorder strength. These observations, however, disagreed with the corresponding results obtained by Goldschmidt and Xu [102], who performed a  $1/q$ -expansion of the 3-state RFPM and found that there is a first-order transition, irrespective of the disorder strength. Another major interest in systems with quenched disorder is the determination of the ground state (GS). The importance and techniques related to GS problem are discussed in Chap. 5.

### 2.2.3 Spin-glass model

It was in the middle of the 20<sup>th</sup> century that many researchers started paying much attention to different alloys. Particular attention was given to the mixture of Mn in Cu. This mixture exhibited unusual properties that raised many questions among condensed matter physicists [103, 104, 105]. It appeared that the susceptibility shows a phase transition at a temperature  $T_c$  which is roughly proportional to the concentration of Mn. However, the transition is not between paramagnetic and an ordered phase. There is a new phase which had many different features compared to a paramagnetic phase. There is no spontaneous magnetisation. It is also observed that the susceptibility  $\chi$  is not inversely proportional to the temperature. Indeed, it stayed constant and did not follow the Curie law ( $\chi \propto 1/T$ ).

The  $s - d$  interaction which couples conduction electrons to the electrons of unfilled inner shells is responsible for the unusual low-temperature behaviour [106]. This interaction is discussed in Ref. [107, 108, 109] without involving the possibility of anti-ferromagnetism. It is shown in Ref. [110] that the  $s - d$  interaction can imply anti-ferromagnetism and spin waves. However, in Ref. [111], it is shown that the  $s - d$  interaction can be described by the Ruderman and Kittel model introduced in Ref. [112]. The resulting coupling between two Mn ions separated by a distance  $r$  denoted by  $J_{xy}^{(\text{RKKY})}$  is called RKKY interaction. Mathematically, the RKKY interaction between two spins  $\vec{s}_x$  and  $\vec{s}_y$  at distance  $r$  from each other can be written as

$$J_{xy}^{(\text{RKKY})} \sim \cos\left(\frac{\mathbf{k} \cdot \mathbf{r}}{|\mathbf{r}|^3}\right), \quad (2.28)$$

the wave vector  $k$  is of the same order as the Fermi vector. The Eq. (2.28) implies that the coupling either can be ferromagnetic or anti-ferromagnetic depending on the distance between the ions.

Many studies [106, 113, 114, 115] contributed to the theory until in 1970 Anderson first used the term spin glass. Analogous to the structural glasses, presence of a low-temperature phase with an unidentified order is observed. Anderson introduces a Hamiltonian exhibiting an explicit dependence on the disorder in Ref. [116]. His main argument is that the exchange interaction of Mn ions play a dominant role

compared to the electron interactions. The Mn ion interaction is given by RKKY interaction given in Eq. (2.28), whose sign depends on the distance  $r_{xy}$  between two spins  $\vec{s}_x$  and  $\vec{s}_y$  on site  $x$ . The strength of this interaction weakens with increasing the distance  $r_{xy}$ . The distance  $r_{xy}$  is random and changes with each alloy and its disorder. Hence, Anderson proposed the first SG Hamiltonian as a Heisenberg model

$$\mathcal{H} = \frac{1}{2} \sum_{x \neq y} J_{xy} \vec{s}_x \cdot \vec{s}_y, \quad (2.29)$$

where the  $J_{xy}$  are random values generated from a distribution that should reproduce roughly the RKKY interaction. This implies that the random variables  $J_{xy}$  are used to simulate the experimental couplings  $J_{xy}^{(\text{RKKY})}$ .

Although the model in Eq. (2.29) looks very simple, it is very difficult to treat it theoretically. Various different theoretical and numerical techniques has been employed to study this mode in finite dimensions. Numerical computations can test any proposed working hypothesis with some limitations. These working hypotheses are often named as pictures. Prominent examples of such pictures are the replica-symmetry-breaking (RSB) and the droplet picture. One of the core issues of research in spin glass theory is the incompatibility in these two approaches. However, it is rather difficult to perform a conclusive numerical test in the three-dimensional case. We will discuss these pictures in the next sections.

### 2.2.3.1 Edwards–Anderson (EA) model

One of the most studied models in spin glass is the Edwards–Anderson (EA) model by Edwards and Anderson in Refs.[117, 118]. It is able to catch many experimental aspects of physics. This model is a simplistic form of the Heisenberg model described by Eq. (2.29). The simpler form is exactly the form represented in Eq. (2.1), which in the absence of the external magnetic-field can be written as:

$$\mathcal{H} = - \sum_{\langle i,j \rangle} J_{ij} s_i s_j. \quad (2.30)$$

The couplings  $J_{ij}$  are usually chosen from a Gaussian or from a bimodal distribution. Each different realisation of the couplings will lead to a different behaviour. However, in thermodynamic limit the behaviour should be similar. Hence, larger lattices should give on average better results. In order to get results for a set of different disorders, one should average the physical quantities. The average result of a set of couplings should always stay similar. This assumption is called self-averaging. This assumption is used to define the free energy of the spin glasses. If  $\mathcal{F}_J$  and  $\mathcal{Z}_J$  are the free energy and partition function of a given realisation respectively and the subscript  $J$  describes here one specific bond configuration. The

average free energy over all disorders can be written as:

$$\mathcal{F} \int \mathcal{F}_J P(J) dJ = -k_B T \int P(J) \ln \mathcal{Z}_J dJ = -k_B T \overline{\ln \mathcal{Z}_J}. \quad (2.31)$$

The bar in the above equation represents the average over all disorders. Eq. (2.31) displays the major analytical difficulty of SG model. The main difficulty is to take the quenched average  $\overline{\ln(\mathcal{Z}_J)}$ . It is easier to take the annealed average  $\ln(\overline{\mathcal{Z}_J})$ , however the annealed free energy  $\mathcal{F}_{\text{Anl}} = \ln \overline{\mathcal{Z}_J}$ , gives wrong results at low temperatures [119]. Edwards and Anderson proposed that the replica trick can be used to overcome this problem. The trick is to use the identity  $\ln(x) = \lim_{n \rightarrow 0} \frac{x^n - 1}{n}$  to transform the annoying logarithm in a power law.

$$\mathcal{F} = -k_B T \overline{\ln \mathcal{Z}_J} = -k_B T \lim_{n \rightarrow 0} \frac{\overline{\mathcal{Z}_J^n} - 1}{n}. \quad (2.32)$$

Assuming that  $n$  is an integer, one can define  $\overline{\mathcal{Z}_J^n}$  as the partition function of  $n$  independent replicas of the same realisation. These realisations belong to the same disorder distribution but differ from one another. Now one can define a new order parameter with the help of replicas [120].

$$q^{\text{ab}} = \left\langle s_i^{(a)} s_i^{(b)} \right\rangle \quad (2.33)$$

where (a) and (b) indicate different replicas. The replica trick helps simplifying the calculation, however, it comes with some restrictions such as taking the limit  $n \rightarrow 0$  with  $n \in \mathbb{N}$ . The EA model is not fully understood analytically. The replica trick became a very useful tool to study disordered systems. The EA model can be extended to a model with quantum spins [121, 122], but this is out of the scope of this thesis.

### 2.2.3.2 Mean-field picture

**The Sherrington-Kirkpatrick (SK) model** The EA model is based on nearest neighbour interactions, therefore, it can not be treated mathematically via mean field theory. In 1975, Sherrington and Kirkpatrick slightly modified the Hamiltonian Eq. (2.30) by imposing infinite (of the order of the size of the lattice) range interactions with Ising spins in Ref. [123].

$$\mathcal{H} = \frac{1}{2} \sum_{i < j} J_{ij} s_i s_j. \quad (2.34)$$

In comparison to the EA model, the sum runs over all pairs of spins in the system and not only over nearest neighbour pairs. As the mean field theory applies to

this model, a mean field solution is proposed. However, the SK solution had non-physical properties such as negative entropy at the low temperatures. Sherrington and Kirkpatrick argue the limit of number of spins  $N \rightarrow 0$  and the thermodynamic limit  $N \rightarrow \infty$  are commutative and could cause the negative entropy. However, later it is shown in Ref. [124, 125] that their assumption of replica symmetry breaking is the cause this problem. They assumed that the overlap given by Eq. (2.33) is same independent of  $n$  replicas chosen for the replica trick,

$$q^{ab} = q(1 - \delta^{ab}). \quad (2.35)$$

In Ref. [124] it is shown that the replica symmetry solution proposed for SK model in Ref. [123] is stable only at high temperatures. In a study performed in Ref. [126], it is shown that the replica symmetry trick holds in the paramagnetic phase only. Under a certain temperature, massless modes in the overlap correlation functions become unstable. Hence, replica symmetry is unstable in the SG phase. Therefore the results obtained using this method are not correct at low temperatures. This statement is also true in the presence of an external magnetic-field at low temperatures and fields with small amplitude. However, for large amplitude of magnetic-field, there exists a SG phase. The critical line where the RS phase

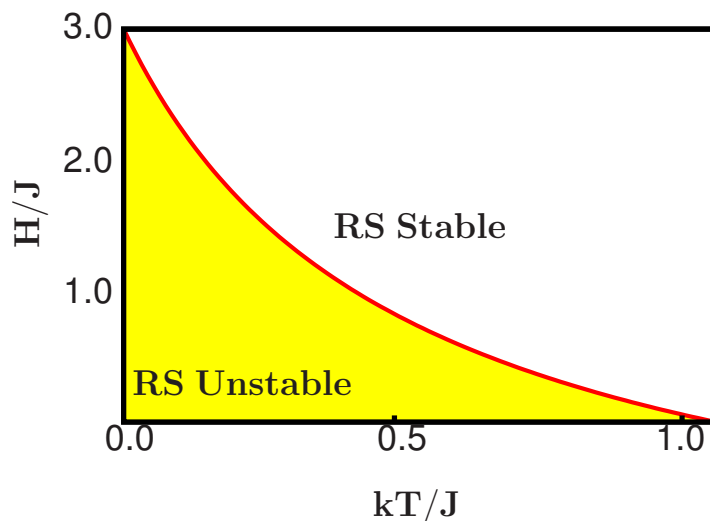


Figure 2.3: Schematic representation of the de Almeida-Thouless (dAT) line (red curve). In the yellow region under the red line RS solution fails and above the red line this solution is valid.

becomes unstable is shown as a red curve in Fig. 2.3 and is called the de Almeida-Thouless (dAT). Even though the reason for this instability is suspected to be replica symmetry [125, 124], it is not clear how to break the symmetry between replicas to obtain a physically reasonable solution.



- Divide a matrix of size  $n \times n$  into  $n/m_1$  blocks.
- The off-diagonal terms of the diagonal blocks are assigned a new value  $q_1$ .
- The first step of RSB (1RSB) is complete.
- Iterate the above process in each block.
- Each block is divided in  $m_1/m_2$  sub-blocks of size  $m_2 \times m_2$ .

The process can be iterated until the full RSB solution is found. In this way an overlap matrix is constructed which has any two rows (or columns) identical up to permutations. This property is called replica equivalence. Replica equivalence holds for both RS and RSB matrices.

In the RS phase  $q^{ab} = 0 \forall a, b$ , so the probability distribution of the order parameter,  $P(q)$  is a  $\delta(0)$ . The full RSB ansatz implies that in the SG phase the probability distribution function of the order parameter is non-trivial. By simply counting the  $n(n-1)$  non-diagonal values  $q^{ab}$ , one has

$$\begin{aligned}
P(q) &= \frac{1}{n(n-1)} \sum_{a \neq b} \delta(q - q^{ab}) = \\
&= \frac{n}{n(n-1)} [(n - m_1)\delta(q - q_0) + (m_1 - m_2)\delta(q - q_1) + \\
&\quad + (m_2 - m_3)\delta(q - q_2) + \dots] .
\end{aligned} \tag{2.38}$$

Once the  $n \rightarrow 0$  limit is taken,

$$P(q) = m_1\delta(q - q_0) + (m_2 - m_1)\delta(q - q_1) + (m_3 - m_2)\delta(q - q_2) + \dots , \tag{2.39}$$

the  $P(q)$  is positive definite only if  $0 < m_1 < m_2 < \dots < 1$ . From theory and simulations one can hypothesize that the  $q_i$  is an infinite sequence, hence a function  $q(x)$  can be defined such that

$$q(x) = q_i \text{ if } m_i < x < m_{i+1}. \tag{2.40}$$

In Ref. [133] it is shown that after a  $k$ -step RSB,  $q(x)$  is a piecewise function that can take at most  $k + 1$  different values. In the limit  $k \rightarrow \infty$ ,  $q(x)$  becomes a continuous function in the interval  $[0,1]$ . Hence, using this representation the free energy becomes a function of  $q(x)$ . It is also shown by Parisi that

$$q(x) = q_m \text{ for } x \leq x_m, \tag{2.41}$$

$$q(x) = q_M \text{ for } x \geq x_M. \tag{2.42}$$

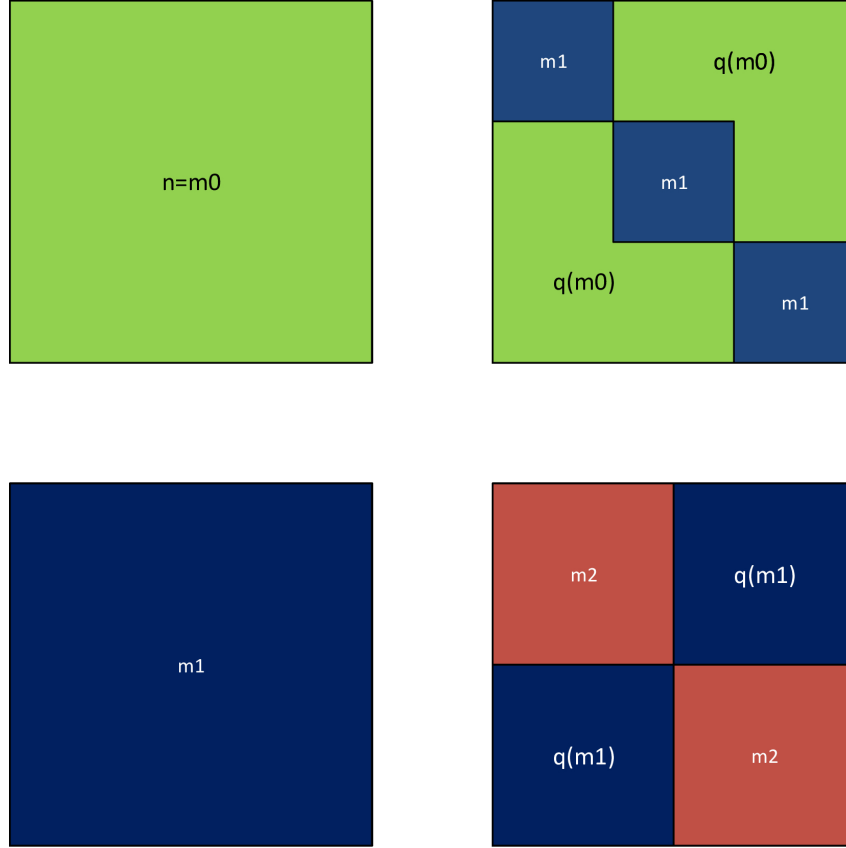


Figure 2.5: Schematic representation of RSB

This implies that the probability distribution function can be written as the sum of two delta functions connected by a smooth function  $\tilde{P}(q)$  which is non-zero only in the interval  $x_m < x < x_M$

$$P(q) = x_m \delta(q - q_m) + \tilde{P}(q) + x_M \delta(q - q_M). \quad (2.43)$$

The Parisi ansatz shows that there is an underlying hierarchical structure in the organization of the states in the SG phase, which results in an ultrametric overlap space where  $q^{ac} \geq \min(q^{ab}, q^{bc})$  [136, 137, 138]. RS can be described as the root of the tree because at this level all states have the same overlap  $q_0$ . In the first step of replica symmetry breaking the replicas part in two groups. Replicas within the same group share overlap  $q_1$ , otherwise, it is  $q_0 < q_1$ , and so on for further steps of RSB. If two belong to the same group the overlap between two replicas  $\alpha$  and  $\beta$  can be identified by returning back to the root of the tree.

There are infinitely many metastable states that do not relate through evident symmetries. The space of configurations consists of many local minima separated

by large barriers (free energy barriers) whose height goes to infinity in the infinite-volume limit [120]. The number of valleys is exponential in the number of spins  $N$  [139, 140, 141]. Therefore, time spent in each minima valley also grows exponentially in the number of spins. Consequently, in the SG phase the dynamics of SG is extremely slow, and in the thermodynamic limit the ergodicity is broken [142]. This is shown in the study of the first infinite-range model (SK) [131]. This model is an extension to SK model that has interactions between  $p$  spins (also called the  $p$ -spin model). The limit  $p \rightarrow \infty$  of the  $p$ -spin model produces an exactly solvable model called the random energy model (REM) [143]. In this model, the probability of a state depends solely on its energy and not on the system configuration.

Because of a lack in rigorousness in the Parisi solution, further numerical studies were performed, however a rigorous mathematical proof came 20 years later and is described in Ref. [144, 145, 146].

### 2.2.3.3 The droplet picture

The motivation behind the droplet picture were numerical domain-wall re-normalization group studies of low-dimensional SG [147, 148]. In addition to that a schematic scaling theory of SG proposed by McMillan [149] which also favoured such picture. Motivated by these studies, the droplet picture of the ordered phase in SG is proposed in Ref. [150, 151, 152, 153, 154] by Fisher and Huse. This theory is based on the Migdal-Kadanoff approximation [155, 156]. Within a pure state, phase coexistence occurs in form of low lying excitations (droplets) of spins in the sub-dominant state. The boundaries of these domains for a particular disorder are not fixed. These boundaries fluctuate or move around with the change in disorder. The unsatisfied links are exploited and the strongly satisfied links are avoided. The effect is that the droplets are non-convex, and their boundary scales as  $L^{d_s}$ , with  $d - 1 \leq d_s < d$ , so they are not space-filling. The fundamental ansatz of droplet theory is inspired by an earlier argument from Anderson and Pond in the aforementioned Migdal-Kadanoff approach in Ref. [157]. This ansatz states that the free-energy cost of the lowest-energy excitations of linear size  $\ell$  are

$$F_\ell \sim \gamma(T)\ell^\theta, \quad (2.44)$$

where  $\theta(0 < \theta < (d - 1)/2)$  and  $\gamma$  are the stiffness exponent and the stiffness modulus, respectively. That implies that that infinite energy is required to excite a finite fraction ( $\ell \sim L$ ) of the total number of spins, so only small excitations ( $\ell \ll L$ ) are supported.

In the droplet picture the stiffness exponent controls the decay of the correlations as

$$C(|i - j|) = \overline{\langle s_i s_j \rangle^2} - \overline{\langle s_i \rangle^2} \overline{\langle s_j \rangle^2} \sim \frac{1}{|i - j|^\theta}, \quad (2.45)$$

that entails  $\overline{q^2} - \bar{q}^2 \rightarrow 0$ , and therefore the overlap distribution is a delta function,  $P(q) = \delta(q - q_{\text{EA}})$ . Another important feature of the droplet theory is that the energy barrier for flipping a droplet in a field  $h$  scales as  $L^\theta - hL^{d/2}$ . The value of  $\theta$  is bounded  $\theta < (d - 1)/2$ , therefore in the presence of any magnetic-field SG phase is unstable. This prediction is in contrast with the RSB theory, which predicts a dAT line for  $h > 0$ . Both the droplet and the RSB scenario describe the spin glass phase well [158, 159, 160, 161, 162, 163]. There is a quite good agreement in the spin glass community that the RSB scenario is valid for dimensions greater than the upper critical dimension  $d_u = 6$ , and that the droplet picture is exact in  $d = 1$ . However, there are no conclusive studies which could describe which of the two theories is correct or incorrect.

## 2.3 Summary

In this chapter, I introduced the concepts related to the random-field Potts model and spin glasses. It is clear from the literature review that the disordered systems are hard to study theoretically. Therefore, the numerical approaches are used to support or negate the mathematical arguments. In this thesis, we use computational techniques to study some aspects of these models.

# Chapter 3

## Computational methods

In the last chapter, it is mentioned that spin glass (SG) and random-field Potts model (RFPM) both have a rugged and complex energy landscape. We discussed the analytical difficulties in studying such systems and mentioned that numerical simulations play a crucial role to study equilibrium or non-equilibrium properties of spin glasses and random-field Potts model. However, these systems are not easy to simulate either. We do need sophisticated and advanced methods to study disordered systems.

This chapter is divided into three sections. In section 3.1, an introduction to Monte-Carlo methods including Metropolis algorithm, statistical errors etc. is given. In section 3.2 the replica-exchange Monte-Carlo method called parallel tempering (PT) is discussed. In the last section 3.3, we go through computational methods specifically designed to study the spin glasses.

### 3.1 Monte-Carlo methods

To study physical quantities in physics, one has to solve high dimensional integrals with a large number of degrees of freedom or for the case of discrete degrees of freedom summation over many different states has to be performed. Even if the dependence of the observable of the micro-state is known, the number of states increases exponentially with the size of the system. For the Ising model, the number of possible configurations is equal to  $2^{L^d}$  with  $d$  being the dimension of the system. Hence, this approach is infeasible. However, trustworthy approximate results can be derived from alternative approaches.

A set of such alternative approaches is called Monte Carlo methods. In this approach, the configuration space is sampled randomly trying to get information about the system. A simple random sample is a measure of a statistical population where each member has an equal probability of being chosen. If simple random

sampling is used, the sample size has to be very large to get good approximations for the system. However, the size of configuration space is so large that it is very unlikely that a representative or even relevant part of it is visited. Therefore, one uses importance sampling techniques, where instead of choosing configurations randomly, the states are selected employing a weight function that selects states according to desired distributions. Consequently, the computational effort to solve the same problem reduces.

The expectation value of an observable  $\langle \mathcal{O} \rangle$  is given by:

$$\langle \mathcal{O} \rangle = \frac{\sum_s \mathcal{O}(s) e^{-\beta \mathcal{H}}}{\sum_s e^{-\beta \mathcal{H}}} . \quad (3.1)$$

A distribution for the states can be accommodated in Eq. (3.1) in the following way

$$\langle \mathcal{O} \rangle = \frac{\sum_s [\mathcal{O}(s) e^{-\beta \mathcal{H}} / \mathcal{P}(s)] \mathcal{P}(s)}{\sum_s [e^{-\beta \mathcal{H}} / \mathcal{P}(s)] \mathcal{P}(s)} . \quad (3.2)$$

By replacing  $\mathcal{P}(s)$  with the Boltzmann distribution in Eq. (2.6), we obtain

$$\langle \mathcal{O} \rangle = \frac{1}{M} \sum_i \mathcal{O}(s_i) . \quad (3.3)$$

In Eq. (3.3), the states  $s_i$  are selected from a Boltzmann distribution. In the next section, I discuss the algorithms that allow for a sampling of states according to the Boltzmann distribution.

### 3.1.1 Metropolis algorithm

The Metropolis algorithm is named after Nicholas Metropolis who co-authored the Ref. [164] in 1953. This algorithm makes use of a Markov chain of successive states  $s_1 \rightarrow s_2 \rightarrow \dots$  to evaluate Eq. (3.1)). A carefully-designed transition probability  $\mathcal{P}(s \rightarrow s')$  is used to generate the new state. In the Markov process, the state  $s$  occurs with probability  $\mathcal{P}_m(s)$  at the  $m$ th time step, described by the following equation

$$\mathcal{P}_{m+1}(s) \propto \mathcal{P}_m(s) + \sum_{s'} [\mathcal{T}(s' \rightarrow s) \mathcal{P}_m(s') - \mathcal{T}(s \rightarrow s') \mathcal{P}_m(s)] . \quad (3.4)$$

The sum runs over all states  $s'$ . The first term in the sum of Eq. (3.4) describe the processes entering state  $s$ , and the second term describe the processes leaving this state. The probabilities  $\mathcal{P}_m(s)$  should reach a stationary distribution described by the Boltzmann distribution in the limit  $k \rightarrow \infty$ . The transition probabilities  $\mathcal{T}$  are designed in such a way that for all states  $s$  and  $s'$  the detailed balance condition given by

$$\mathcal{T}(s' \rightarrow s) \mathcal{P}_{\text{eq}}(s') = \mathcal{T}(s \rightarrow s') \mathcal{P}_{\text{eq}}(s) \quad (3.5)$$

is satisfied. The condition in Eq. (3.5) means that the process has to be reversible. Furthermore, the ratio of the transition probabilities only depends on the change in energy  $\Delta\mathcal{H}(s, s') = \mathcal{H}(s') - \mathcal{H}(s)$ , i.e.,

$$\frac{\mathcal{T}(s \rightarrow s')}{\mathcal{T}(s' \rightarrow s)} = \exp[-\beta(\mathcal{H}(s') - \mathcal{H}(s))] = \exp[-\beta\Delta\mathcal{H}(s, s')]. \quad (3.6)$$

There are different choices for the transition probabilities  $\mathcal{T}$  that satisfy Eq. (3.6). In this thesis the simulations are restricted to the following choice:

### Metropolis or Metropolis-Hastings algorithm

In this case  $\mathcal{T}(x) = \min(1, x)$  and so

$$\mathcal{T}(s \rightarrow s') = \begin{cases} 1, & \text{if } \Delta\mathcal{H} \leq 0; \\ e^{-\beta\Delta\mathcal{H}(s, s')}, & \text{if } \Delta\mathcal{H} \geq 0. \end{cases} \quad (3.7)$$

#### 3.1.1.1 Equilibration

In order to obtain a correct measure of an observable  $\mathcal{O}$ , it is crucial to guarantee that one is actually sampling an equilibrium state. In general, the initial configuration of the simulation can be chosen arbitrarily. The most popular choices are the polarised configuration or randomly generated configuration. The system requires many Monte-Carlo steps before an equilibrium state at a given temperature is obtained. The time needed to reach thermal equilibrium is called equilibration time and is denoted by  $\tau_{\text{eq}}$ . This time is usually measured in the units of Monte Carlo steps.

One has to ensure that all measured observables are measured in thermal equilibrium. Some observables for spin glasses, such as the energy, equilibrate faster than others, e.g., magnetisation and thus the equilibration times of all observables measured need to be examined. While studying the physical quantities in the next chapters, some methods to check the equilibration are discussed.

#### 3.1.2 Auto-correlation times and error analysis

The Metropolis algorithm is based on a Markov process; the new states are generated by modifying the previous ones. Hence the newly generated states can be highly correlated. To ensure that the measurement of an observable  $\mathcal{O}$  is not affected by correlated configurations, it is essential to measure the auto-correlation time  $\tau_{\text{auto}}$  that describes the time it takes for two measurements to be decorrelated. This means that in a Monte Carlo simulation after the system has been thermally equilibrated, measurements can only be taken every  $\tau_{\text{auto}}$  MCS in order to have

smaller statistical errors. The auto-correlation time can be computed via measuring the time-dependent auto-correlation function for a given observable  $\mathcal{O}$ :

$$C_{\mathcal{O}}(t) = \frac{\langle \mathcal{O}(t_0)\mathcal{O}(t_0+t) \rangle - \langle \mathcal{O}(t_0) \rangle \langle \mathcal{O}(t_0+t) \rangle}{\langle \mathcal{O}^2(t_0) \rangle - \langle \mathcal{O}(t_0) \rangle^2}. \quad (3.8)$$

In general,  $C_{\mathcal{O}}(t) \sim \exp(-t/\tau_{\text{auto}})$  and so  $\tau_{\text{auto}}$  is given by the value where  $C_{\mathcal{O}}$  drops to  $1/e$ . An alternative is the integrated auto-correlation time  $\tau_{\text{auto}}^{\text{int}}$ , which is easier to compute:

$$\tau_{\text{auto}}^{\text{int}} = \frac{\sum_{t=1}^{\infty} (\langle \mathcal{O}(t_0)\mathcal{O}(t_0+t) \rangle - \langle \mathcal{O} \rangle^2)}{\langle \mathcal{O}^2 \rangle - \langle \mathcal{O} \rangle^2} \quad (3.9)$$

Auto-correlation effects influence the determination of the error of statistical estimates. It can be shown [74] that the error  $\Delta\mathcal{O}$  is given by

$$\Delta\mathcal{O} = \sqrt{\frac{\langle \mathcal{O}^2 \rangle - \langle \mathcal{O} \rangle^2}{(M-1)} (1 + 2\tau_{\text{auto}})}. \quad (3.10)$$

Here  $M$  is the number of measurements. The auto-correlation time directly influences the calculation of the error bars and must be computed and included in all calculations. So far, we have not discussed how the auto-correlation times depend on the system size and the temperature. Like the equilibration times, the auto-correlation times increase with increasing system size. In the next section, we discuss parallel tempering which belongs to the Monte Carlo methods, however we introduce it in a separate section where we also discuss a new method to tune the required parameters.

## 3.2 Parallel Tempering

In the introduction of this chapter, we mentioned that parallel tempering is used to study complex systems with rugged energy landscapes. Before we discuss the parallel tempering method, we will discuss the need to use PT. In general, for infinitely long simulations, it is enough to use Metropolis algorithm introduced in [164]. However, as mentioned earlier, spin glasses and random-field Potts model have a rugged energy landscape with multiple minima and maxima which become more pronounced with increasing system size. Thus, any reasonable MC sampling has to overcome energy barriers and cross from one basin to another in the configuration space to obtain a representative set of configurations. Metropolis or other local moves do not allow the system to explore all of the rugged configuration space efficiently. The efficiency of the algorithm can be increased by supplementing local configurational Metropolis moves with global swap moves (parallel tempering or exchange Monte-Carlo move) that update an entire set of configurations.

In the literature, glassy systems such as spin glass with complex free energy landscape are studied via parallel tempering (PT) [165, 166, 167, 168, 169]. It is well known that parallel tempering is relatively efficient at finding the ground states of disordered systems [170, 171, 172, 173, 174, 175, 176], because parallel tempering is more efficient than using only the Metropolis algorithm at overcoming free-energy barriers. RFPM is a comparable system to spin-glass with quenched disorder and frustration, motivating us to use this algorithm for studying the ground states.

Assume there is a system of  $N_T$  non interacting replicas i.e. identical copies of the system to be simulated. The  $m$ -th replica is associated with the temperature  $T_m$  ( or inverse temperature  $\beta_m$ ). An ensemble of states of at each replica can be written as:  $\{R\} = \{R_1, R_2, \dots, R_{N_T}\}$ , and the partition function can be written as

$$\mathcal{Z} = \text{Tr}_{\{R\}} \exp\left(-\sum_{m=1}^{N_T} \beta_m \mathcal{H}(R_m)\right) = \prod_{m=1}^{N_T} Z(\beta_m), \quad (3.11)$$

where  $Z(\beta_m)$  is one of the systems. For a given set of inverse temperatures,  $\{\beta\} = \{\beta_1, \beta_2, \dots, \beta_M\}$ , the probability distribution of finding  $\{R\}$  becomes

$$P(\{R, \beta\}) = \prod_m^M P_{\text{eq}}(R_m, \beta_m), \quad (3.12)$$

where

$$P_{\text{eq}}(R, \beta) = Z^{-1}(\beta) \exp(-\beta \mathcal{H}(R)) \quad (3.13)$$

In constructing a Markov process for parallel tempering, a transition matrix  $\mathcal{T}(R, \beta_m | R', \beta_n)$  is introduced. This transition matrix gives the probability of exchanging the configurations of the  $n$ -th and  $m$ -th replicas. To keep the system at equilibrium, detailed balance is imposed on the transition matrix:

$$\begin{aligned} & P(\dots; X, \beta_m; \dots; R', \beta_n; \dots) \mathcal{T}(R, \beta_m | X', \beta_n) \\ &= P(\dots; R', \beta_m; \dots; R, \beta_n; \dots) \mathcal{T}(R', \beta_m | X, \beta_n). \end{aligned} \quad (3.14)$$

Eq. (3.13) implies

$$\frac{\mathcal{T}(R, \beta_m | R', \beta_n)}{\mathcal{T}(R', \beta_m | R, \beta_n)} = \exp(-P_{\text{ex}}), \quad (3.15)$$

where

$$P_{\text{ex}} = (\beta_n - \beta_m)(\mathcal{H}(R) - \mathcal{H}(R')). \quad (3.16)$$

Therefore the replica-exchange part of the transition probability can be expressed as

$$\mathcal{T}(R, \beta_m | R', \beta_n) = \begin{cases} 1, & \text{for } P_{\text{ex}} < 0 \\ \exp(-P_{\text{ex}}), & \text{for } P_{\text{ex}} > 0 \end{cases} \quad (3.17)$$

if one adopts the Metropolis method.

In our program we use the following two moves at every Monte Carlo step:

1. Each replica is simulated independently using the Metropolis update.
2. Exchange of two configurations  $R_m$  and  $R_{m+1}$ , is tried and accepted with the probability  $P_{\text{ex}}$ .

The acceptance ratio of the exchange trial decreases exponentially with the difference  $\beta_m - \beta_n$ , therefore it is more efficient to restrict the exchange to the neighbouring replicas  $R_m$  and  $R_{m+1}$ . Before we can do the simulation, the set of temperatures has to be chosen.

The most natural way to choose a temperature set would be to start with a random set of temperatures. If two systems are simulated at temperatures  $T_1$  and  $T_2$  with a temperature difference  $\delta T = T_2 - T_1$ , then the energy histograms are obtained by collecting the energies over a set of Monte Carlo steps  $N_{\text{mcs}}$ . These histogram might overlap depending on the difference in the two temperatures. If  $\delta T$  is too small, the overlap will be very large. This means that the states sampled at temperature  $T_1$  are most likely to appear at temperature  $T_2$  again. If the overlap is large, the exchange rate will be higher as there are many similar states.

In Fig. 3.1 we show a schematic plot of histograms for four different temperatures. We observe that for temperatures  $T_0$  and  $T_1$  the overlap is too large, this implies that we would be wasting a lot of simulation time without getting much out of it. In the same way, we observe that for the temperatures  $T_2$  and  $T_3$ , there is no overlap. In the latter case, we will never have an exchange between replicas. Hence, it is very crucial to have a good set of temperatures to achieve a high efficiency. However, for  $T_1$  and  $T_2$  we have an acceptable overlap in the histograms. Hence, the crucial, but non-trivial part of this algorithm is to find the optimal set of temperatures.

### 3.2.1 Selection of the optimum set of temperatures

Many studies [177, 178, 179, 180, 181, 182, 183, 184, 185] proposed different ideas of optimising the chosen temperature set for parallel tempering simulations. Katzgraber *et. al.* [177] argue that the optimal temperature set corresponds to a maximum rate of round trips (tunnelling events) between lowest and highest temperature in the temperature range. They show that the maximum rate can be obtained using a recursive readjustment of temperatures. This feedback-optimised update scheme is a sophisticated and appealing method, but because of its complexity, other methods have been more often implemented in comparative studies and applications of PT.

A newer update scheme to improve the efficiency of parallel tempering systematically was introduced by Bittner *et. al.* [178]. With numerical simulations, it was shown that the average round-trip events of a replica can be significantly increased

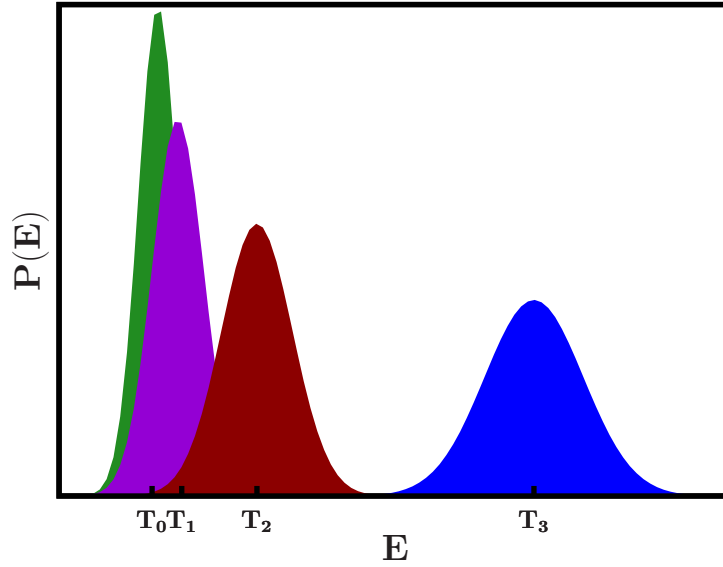


Figure 3.1: Schematic diagram of energy histogram overlap

by adapting the number of Monte Carlo sweeps between replica exchanges to the canonical auto-correlation time. The temperatures are adjusted to yield a 50% exchange rate between adjacent replicas.

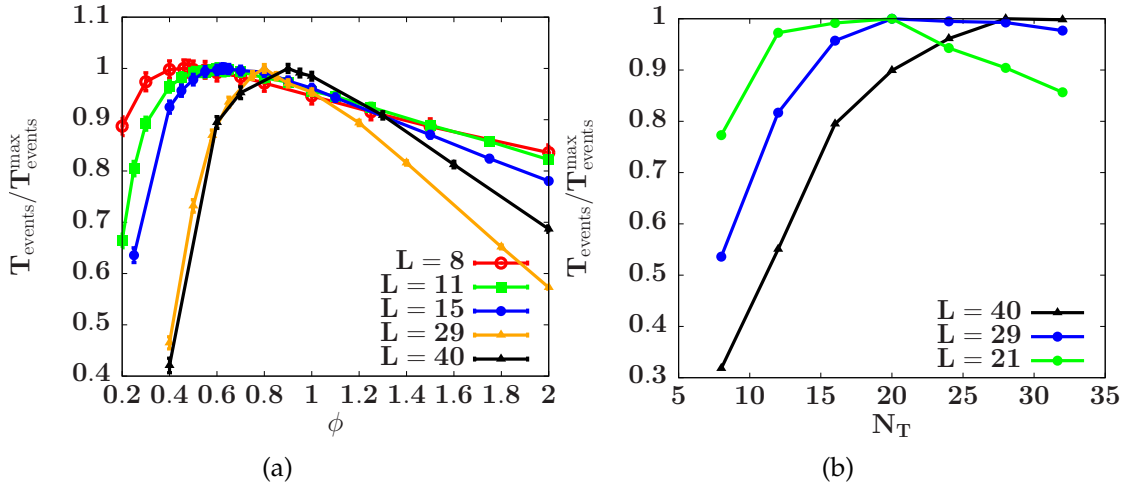


Figure 3.2: Tunnelling as a function of (a)  $\phi$  for  $N_T = 32$  (b)  $N_T$  at  $\phi_{\max}$ . These plots are normalised to the maximum value of the tunnelling events in each system size.

These methods have frequently been used in the literature. The first method is adaptive, and one needs to do simulations and again insert a new temperature between two temperatures if tunnelling time is not optimal. In the second method, Monte Carlo sweeps are tuned with auto-correlation time to get the lowest tunnelling time. This approach, however, is not very efficient if one wanted to do

simulations on GPU (see next section). Therefore, we propose a simpler technique to minimise the tunnelling time in a given temperature range. It is obvious from these studies that acceptance rates and tunnelling time do play the most important role to get an optimised set of temperatures. In our work, we have used a greedy optimisation method to chose an optimal temperature set. This greedy algorithm is straightforward to implement and will work on GPU as well. The temperature  $T_m$  of the  $m_{\text{th}}$  replica is chosen by following equations:

$$\begin{aligned} T_m &= m^\phi T_{\text{norm}} + T_{\text{min}}, \\ T_{\text{norm}} &= \frac{T_{\text{max}} - T_{\text{min}}}{(N_T - 1)^\phi}, \end{aligned} \quad (3.18)$$

where  $T_{\text{max}}$  and  $T_{\text{min}}$  are the maximum and minimum temperatures, respectively. In the following, we choose  $T_{\text{max}} = 1.5$  and  $T_{\text{min}} = 0.2$  for the spin glass simulations. These temperature values are chosen based on the temperature ranges usually studied in the literature. A set of temperatures and run the simulation by choosing some initial value of  $\phi$ . We measure the acceptance rates and the tunnelling time. Once

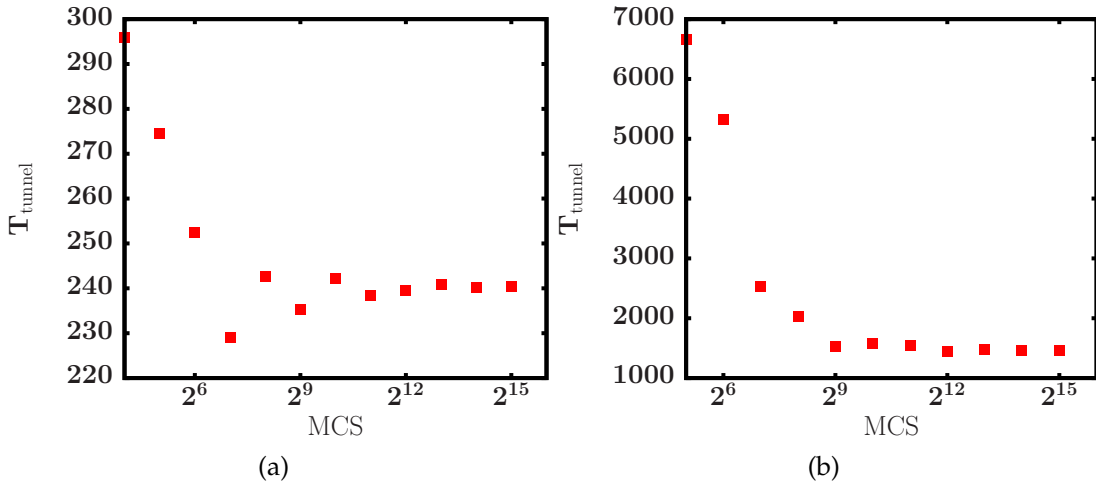


Figure 3.3: Tunnelling time equilibration with respect to Monte Carlo steps (a) for  $L = 15$  and (b) for  $L = 40$ .

the measurement is done, we re-run the simulation with a modified value of  $\phi$ . The value of  $\phi$ , which gives the minimum tunnelling time is used for all the simulations. The number of temperatures in a given range is fixed and the different values of  $\phi$  are used to run the simulations. In Fig. 3.2, the tunnelling events (inverse tunnelling time) is shown as a function of  $\phi$ . It is evident from Fig. 3.2 that for increasing system size  $L$ , the peak shifts to higher values of  $\phi$ .

By fixing the temperature range, it is possible to get a suitable set of temperatures by finding the optimal value of  $\phi$ . Finite size scaling can be used to estimate

the values for larger system sizes. Why is this method simpler than other methods? The answer is straightforward. One does not need to think of setting up different Monte-Carlo steps at the different temperature. Neither does one need to adapt the temperature set by hand. The only requirement is to run the simulations for different  $\phi$  values for various system sizes.

During the simulation it is important to note that like all the physical quantities, the observed tunnelling times also change during equilibration. It is seen in Fig. 3.3 that the tunnelling events equilibrate quickly. There is no need for long simulations in order to find the optimal value of  $\phi$ . The rapid equilibration of the tunnelling times makes this method very useful for choosing the temperature set. Another important aspect of this method is that we can do finite size scaling for different system sizes to find the optimal value of  $\phi$  in a given range. In Fig. 3.4(a) a functional fit for the optimal value  $\phi = \phi_{\max}$  with respect to system size  $L$  is shown. A similar fit is done for the optimal value  $N_T = N_{T_{\max}}$  in Fig. 3.4(b). The parameters of the fit function of the form  $a + bL$  are listed in the table 3.1. The linear ansatz is used because the  $p$ -values are very high for the fit. Using any other ansatz gave extremely small  $p$ -values.

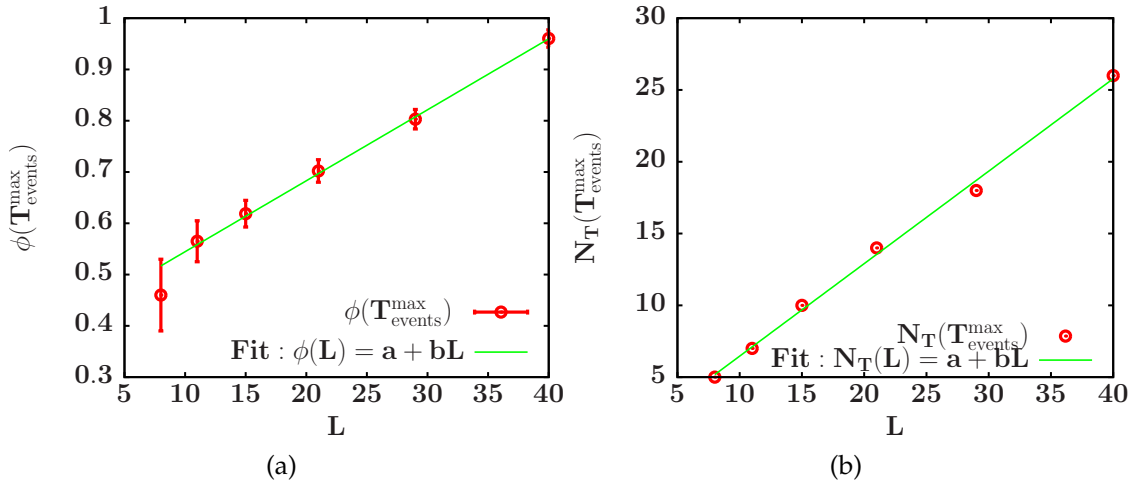


Figure 3.4: Here we show maximum tunnelling events as a function of (a)  $\phi$  for  $N_T = 16$  (b)  $N_T$  at  $\phi_{\max}$ .

One can use the fitted function to predict the optimal value of  $\phi$  or number of optimal temperatures  $N_T$  for any system size. We are usually bound to use the smaller system sizes because of extremely long simulation time. In that short range, we can predict the optimal parameter with a very high accuracy. We also observe that peaks are not very sharp, there is a wide range close to optimal values. By using the fit parameters listed in Table 3.1, we can predict that for a system with  $L = 76$  the optimal value of  $N_T$  should be 48. Either we could use this value, or we could double the run-time of simulation and choose a lower value of  $N_T$ . This

method is advantageous if one wants to pick a temperature set for larger system sizes. Moreover, this approach is beneficial for choosing a temperature set to do parallel tempering on GPU. We will discuss this in the next section. It should be noted that one parameter is fixed and the observed linear behaviour is only for that fixed parameter. We would always choose a finite value and the linear growth does not mean that in the thermodynamic limit the optimal values are infinite. The behaviour might be different if one tries to build a function of multiple parameters. However, for the ranges where we would be interested (or generally one can simulate using current available resources), this method works very well.

parameter	$a$	$b$
$N_T(\phi_{\max})$	0.406	0.0138
$\phi(N_T = 16)$	0.0247	0.6440

Table 3.1: Simulation parameters

### 3.3 Houdayer cluster algorithm

In the previous section, we discussed the applicability and use of parallel tempering for disordered systems. This approach is very efficient for improving equilibration time for a system. However, for spin glasses most numerical studies are still troubled by corrections to finite-size scaling due to the small system sizes currently available. In need of simulating larger system sizes, one requires algorithms which help to equilibrate the system even faster. One such algorithm was proposed by J. Houdayer in Ref. [186]. The Houdayer cluster algorithm (HCA) [186] is an efficient algorithm to study *two-dimensional* Ising spin glasses at low temperatures where equilibration is slow. It is similar to replica Monte Carlo [165], but with the difference that both replicas are at the *same* temperature. By allowing large cluster rearrangements of configurations, the HCA improves equilibration by efficiently tunnelling through configuration space. In this algorithm, two independent spin configurations (replicas) are simulated at the same temperature. The site overlap between replicas at temperatures  $T_1, T_2$ ,  $q_i = s_i^1 s_i^2$  is calculated at every site. It has two domains with either  $q = 1$  or  $q = -1$ . The connected components of these domains are clusters.

One chooses a random site on the overlap lattice and if  $q_i = -1$ , the next neighbour is checked if it belongs to the same domain. When there is no more connected site which belongs to the same domain, the spins belonging to the cluster in both replicas are flipped, irrespective of their orientation. Cluster updates are rejection free. Hence this implementation is very efficient. To ensure ergodicity, the cluster move is combined with standard single-spin Monte Carlo updates. Summarising,

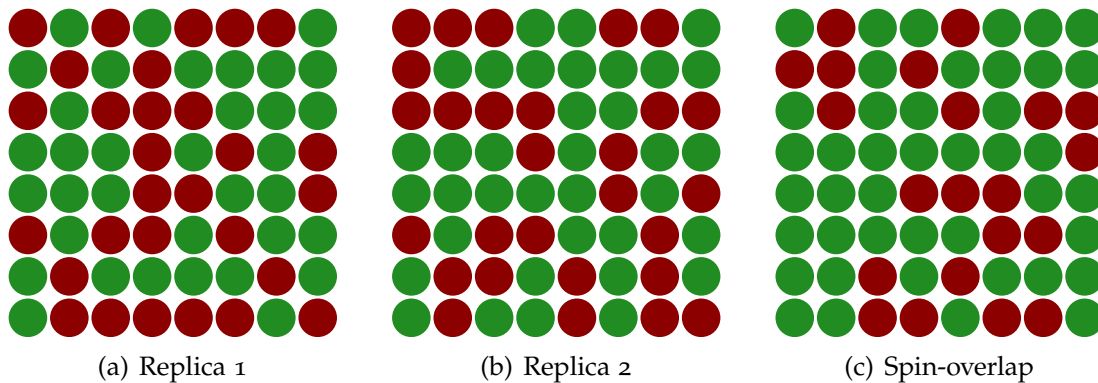


Figure 3.5: Here each colour represent an orientation of spin. One can see that there are more than one clusters available to pick from the site overlap randomly.

one simulation step using the Houdayer cluster algorithm with Metropolis and parallel tempering moves consists of the following steps:

1. Perform one Monte Carlo sweep ( $N$  Metropolis updates) in each replica.
2. Perform one Houdayer cluster move.
3. Perform one parallel tempering update for a pair of neighbouring temperatures.

The efficiency of the Houdayer cluster algorithm depends strongly on the percolation threshold of the desired topology to be simulated. Because spins are added to the cluster with probability 1, if the percolation threshold of the studied lattice is below 50%, then the cluster might span the entire system and an update will yield a configuration which is highly correlated with the last configuration. Hence, in the original paper, Houdayer argues that this method is only applicable in two dimensions. However, Zhu et. al in [187] proposed an improvement to this algorithm. They used the spin reversal symmetry for a modification of algorithm. If the cluster size is larger than half the number of spins, they propose to flip the whole configuration in one of the replicas out of the same temperature replicas. This Isoenergetic cluster algorithm is summarised as follows:

1. Perform one Monte Carlo sweep ( $N$  Metropolis updates) in each replica.
- 2a. If the number of cluster sites with  $q_i = -1$  is greater than  $N/2$ , then all the spins in one of the configurations can be flipped (because of spin-reversal symmetry), thus reducing the cluster size while leaving the energy unchanged.
- 2b. Perform one Houdayer cluster move for all temperatures  $T \lesssim J$ .
3. Perform one parallel tempering update for a pair of neighbouring temperatures.

## 3.4 Summary

In this chapter, we presented the different computational techniques which are used to study disordered systems in this thesis. A new method to set the number and positions of the temperature for the parallel tempering method was proposed. A combination of these methods is used to simulate random-field Potts model and spin glasses. Houdayer cluster algorithm is used in its original form as described in Ref. [186].

## Chapter 4

# Performing spin glass simulations on GPUs

In the previous chapter, we discussed problems related to the equilibration of a spin glass (SG) system. Due to the complex energy landscape, disordered systems are much more difficult to simulate even with the advanced computing methods discussed in Chap. 3. Houdayer's cluster algorithm is overcoming the issue to some extent. One also requires an average over a large number of disorders to ensure a high degree of accuracy in the results. However, the resources available to simulate the larger system sizes are not sufficient. Even the available resources are not very efficient. The growth of computer efficiency has been halted and reached a plateau 15 years ago. According to Moore's law the number of transistors in a dense integrated circuit doubles about every two years. But, Fig. 4.1 the data shows that the frequency of the central processing units is saturating. Nonetheless, Moore's law, predicting exponential growth in the number of transistors in typical integrated circuits, continues to hold [188]. This growth in transistor units has given an opportunity to use additional transistors to form multi-core computational units, instead of speeding up single threads. Consequently, the number of cores available on cluster machines or supercomputers is proliferating (shown via black data points in Fig. 4.1), calling for the parallelisation of established computational approaches and algorithms. Once such parallel algorithm exist, it would be most efficient to have computers with a large number of cores.

In the last few years GPU-accelerated computing has gained much attention. The graphics processing units (GPUs) were originally designed to render triangles in three dimensional graphics and for improving the quality of video games. These devices are massively parallel. A GPU architecture consists of thousands of more efficient, smaller arithmetic logic units (ALUs) designed for handling multiple tasks simultaneously, whereas a CPU consists of a few ALUs optimised for sequential serial processing. This fact is beneficial for simulating disordered systems which can be trivially parallelised. The reason behind this parallelisation is that each

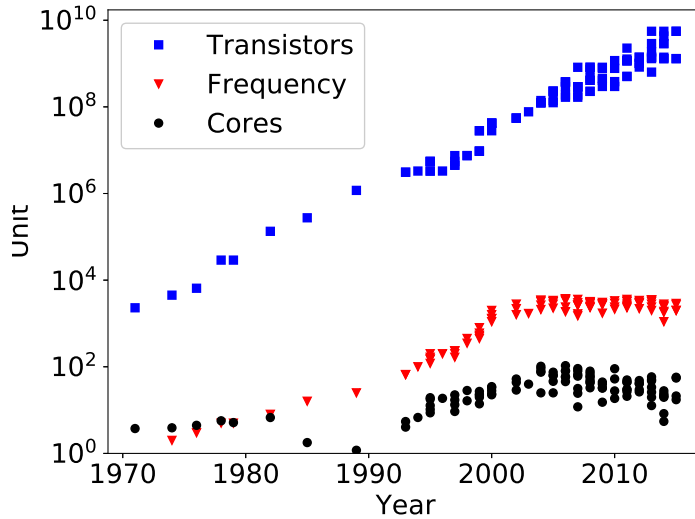


Figure 4.1: Moore’s law is demonstrated here for the GPU transistors (blue data), CPU frequency (red data) and number of cores (black data). The data is downloaded from <https://github.com/karlrupp/microprocessor-trend-data>.

disorder requires its own Monte Carlo simulation. These independent simulations can be distributed on on GPU cores for parallel processing.

This chapter is organised as follows. In Sec. 4.1, the algorithm used to simulate disordered system is presented and the hardware structure of GPUs is discussed. The results for the two dimensional and three dimensional spin glass are benchmarked in Sec. 4.2. In Sec. 4.3, the performance of the implementation is discussed before the chapter is summarized in 4.4.

## 4.1 Hardware, optimization and implementation

In this work, different kinds of GPUs were used for the simulations. The simulations are done using Nvidia Tesla K20/K40, Nvidia GTX Titan black, NVIDIA GTX 1050/1060/1080. These different GPUs belong to distinct generations of the Nvidia architecture. Telsla K20/K40 belongs to Kepler, GTX Titan Black belongs to Maxwell and the GTX 10 series belongs to the Pascal architecture. The crucial components of a GPU are the multiprocessors sustaining multiple threads and the memory of GPU, which play a key role in the efficiency of a GPU program. GPU memory is organised as follows:

- Registers: each multiprocessor is equipped with several thousand registers, access to which is local to each processing unit and extremely fast.

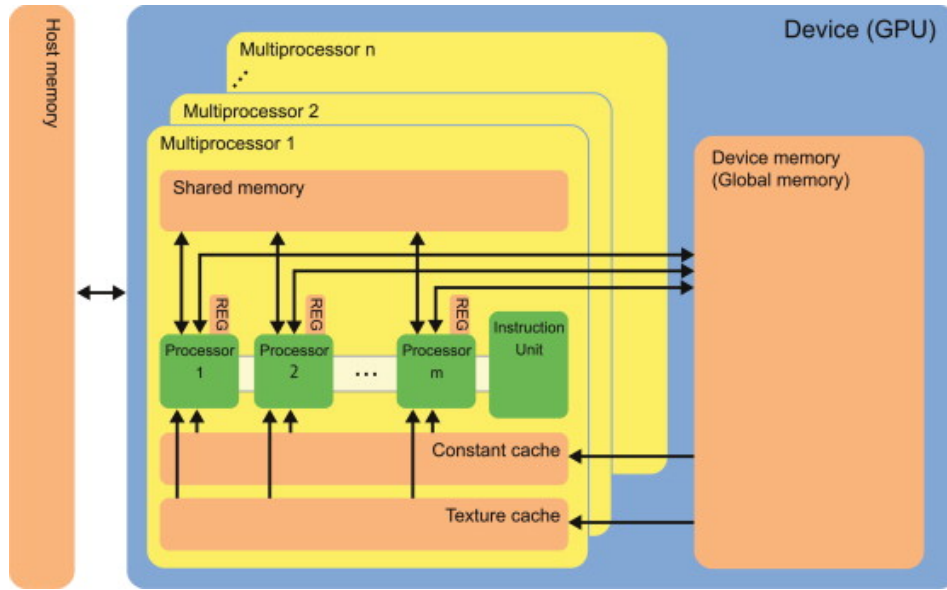


Figure 4.2: Schematic diagram of NIVIDIA GPUs from Ref. [189].

- **Shared memory:** A single multiprocessor consists of many processors. These have access to a small amount (Kepler 16K/32K/48K, Maxwell 64K, Pascal 96K) of shared memory, which serves as a means of synchronisation and communication between the threads (processors) in a block (a set of threads executed on a multiprocessor). This memory resides on-chip and can be accessed essentially without significant memory latency.
- **Global memory:** this large amount of memory is on separate DRAM chips and can be accessed by each thread on each multiprocessor. Access suffers from a latency of several hundred clock cycles.
- **Constant and texture memory:** these memory areas are of the same speed as global memory, but they are cached such that read access can be very fast. From the device perspective, they are essentially read-only.
- **Host memory:** the memory of the host CPU unit cannot be accessed from inside GPU calculations. Memory transfers between global and device memory are important for communication with the outside world.

The CUDA programming language [190] is used for simulations employing the Metropolis and Houdayer cluster algorithm on GPUs. There are a number of studies using GPUs for spin glass systems [189, 191, 192, 193, 194]. Most of these studies are based on domain decomposition, where a lattice is decomposed to smaller units to parallelise the processes. This method is very efficient, however not necessarily easy to implement. Therefore, we use a slightly different approach. We make use of trivial parallelisation of disordered systems. Structure of GPU plays an important

role in efficiency of a CUDA program. A GPU (NVIDIA) has  $C$  cores distributed on  $M_P$  multi-processors. There are multiple thread blocks which are resident on a multiprocessor. Each block can be three dimensional with maximum dimensions  $(1024, 1024, 64)$  on each axis. However, the maximum number of threads in each block can be 2048 (e.g. Pascal architecture) or 1024 (e.g. Maxwell or Kepler architectures). In our system, the parameters to parallelise are the number of temperatures ( $N_T$ ) and the number disordered realisations ( $N_R$ ). We also need to simulate the same disorder twice at the same temperature to study overlap and other functions of overlap. Therefore we have a third parameter, the number of copies at the same temperature ( $N_C$ ), which can be used in the parallelisation. This parallelisation takes place on every block out of total  $N_B$  blocks. To access spin in a given disorder, we have to know exactly on which thread a spin is assigned i.e. how does a thread reads the value of a spin from the memory. To do so, it is needed that one knows exactly the mathematical index of each thread in each block. Therefore for any  $b$ th block, site index of a thread can be calculated as follows:

$$B_{\text{id}} = i + jN_T + kN_TN_R, \quad (4.1)$$

where indices run as  $0 \leq i < N_T$ ,  $0 \leq j < N_R$  and  $0 \leq k < N_C$ . Each disorder is assigned to the running index. The values are set in such a way that the product  $N_TN_CN_R$  equals 2048 for maximum efficiency and usage of the GPU. Depending on the number of multiprocessors we can repeat this unit with different disorder realisations on each block. Every  $b$ th block consists of  $N_R$  disorder realizations. Hence the total number of disorders simulated in parallel is the product of the total number of blocks  $N_B$  and disorder realizations per block  $N_R$ . Now a running index  $L_{\text{id}}$  for a given lattice using  $B_{\text{id}}$  can be written as:

$$L_{\text{id}} = bV_B + B_{\text{id}}, \quad (4.2)$$

where  $V_B = N_TN_RN_C$  is the volume of the block and  $0 \leq b < N_B$  is the block index. Every lattice at a given temperature for a given disorder with a different seed can be initialized on any site given by  $L_{\text{id}}$ . In simpler words to establish analogy, each index  $L_{\text{id}}$  can be considered as a single CPU core to run the simulation. At this point, we are prepared to program the Metropolis algorithm on GPUs for disordered systems. However, while doing the spin updates, the neighbouring spins have to be accessed from the memory. Therefore, the spins have to be organised in the memory in such away that the threads should not access the spins from the same location of memory. This is achieved via  $L_{\text{id}}$ . The total number of spins distributed over the whole GPU memory are  $L^2V_BN_B$ . Any spin at the  $m$ th index of a two dimensional lattice can be written as:

$$M(L_{\text{id}}, B_b) = mV_BN_B + L_{\text{id}}. \quad (4.3)$$

Accessing the coupling requires a little more maths. However, we use the index  $L_{\text{id}}$  for that, as the index of the  $m$ th coupling between  $m$  and  $m + 1$  in any given lattice can be written as:

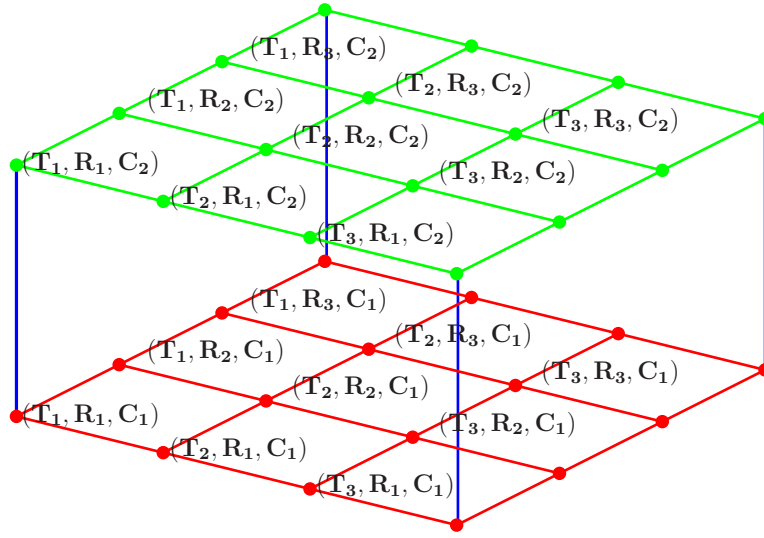


Figure 4.3: Schematic diagram of a thread block of GPU. Each coordinate is a thread and can simulate a two dimensional spin system with a given disorder and temperature.

$$M(L_{\text{id}}) = \begin{cases} \frac{(2mV_B N_B + L_{\text{id}})}{N_T N_C}, & \text{for neighbor in x-direction } x \geq 1 \\ \frac{((2m+1)V_B N_B + L_{\text{id}})}{N_T N_C}, & \text{for neighbor in y-direction .} \end{cases} \quad (4.4)$$

The number of couplings is less than the number of spins as the whole set of temperature shares a disorder twice for two copies with different initialisation. Each site  $m$  has two coupling associated with it, i.e. one to the right neighbouring spin and one to the neighbouring spin below on a two dimensional lattice.

Fig. 4.3 illustrates how thread blocks are utilised on GPU to maximise efficiency. This figure shows one block, and we can put at least one such block on each multiprocessor. Therefore, we have a highly parallelised system over different disorder realisations. We now can start  $V_B$  independent Metropolis updates on each thread of the GPU. Without thinking about the cluster algorithm and parallel tempering, we can now summarise how to simulate disordered systems on GPUs. The steps are as follows:

1. Initialise spins as integer variables using Eq. (4.3) on host (CPU) and device (GPU).
2. Initialise couplings using Eq. (4.4) on host and device. These can be sent as textures. Texture objects can be passed as arguments just as if they were pointers.
3. Once everything is prepared, call the Metropolis kernel.

4. Each thread now has its own  $L^2$  spins on it and simulate a single two dimensional system at a given temperature.
5.  $L_{id}$  enables each thread to know which spins belongs to which system.
6. Once the simulation is completed, kernel gives back the data to CPU.

We already discussed the need for the PT and cluster algorithm to accelerate equilibration. Parallel tempering has  $N_T$  trials to swap the temperatures which are far less than the  $L^2$  trials required for spin flips. Therefore, in our case the parallel tempering is done on the CPU. At first it might seem inefficient, however because of the requirements of the cluster algorithm, the data has to be synchronised in every Monte-Carlo step. We can summarise the PT+Metropolis algorithm as follows:

1. Initialise in the same way as described in the Metropolis update.
2. Call Metropolis kernel in every Monte-Carlo step, calculate change in energy for all  $N_B N_R$  simulated systems.
3. Return the energies and temperature index corresponding to that to host (CPU).
4. Do parallel tempering move on the CPU.
5. Send new index of temperatures to each thread.

The parallel tempering implementation for disordered systems on GPUs is straight forward. However, the Houdayer cluster algorithm is not as easy to implement efficiently. The main problem associated with it is that two copies of a given disorder

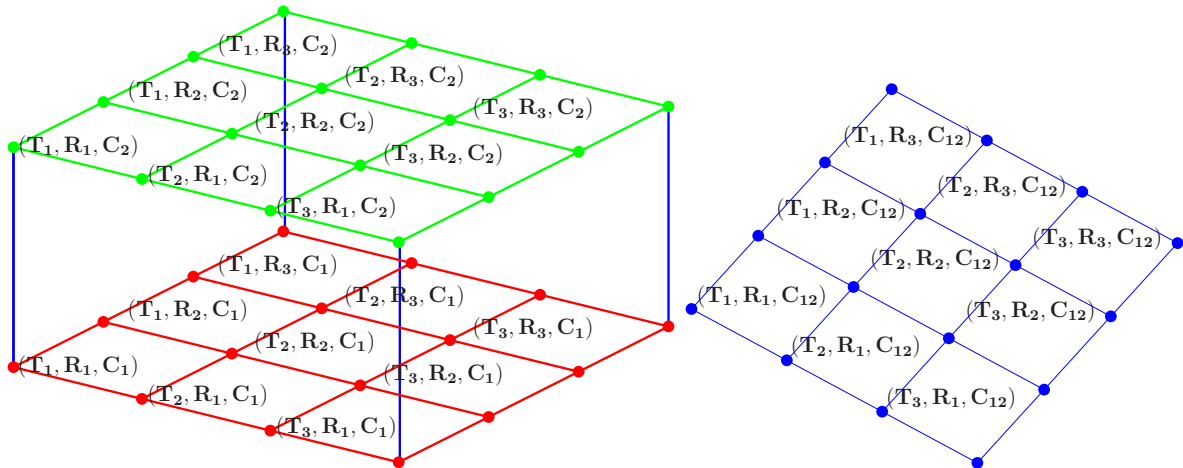


Figure 4.4: Mapping of two replicas ( $C_1, C_2$ ) onto one replica ( $C_{12}$ ) in overlap space.

at given temperatures are required for forming the cluster. We want to keep the count of spins and variables, therefore using the same indices, we would have half of the threads on a block that were free. This is demonstrated in Fig. 4.4, where we map spin space (green and red surfaces) on to overlap configurations (blue surface). We can now only make use of half of the threads on a block that would keep half of the threads on GPU free. One method to overcome this problem is to fill each multiprocessor with two blocks to make most use of the hardware.

Filling the multiprocessors with two blocks might solve the hardware problem, however, cluster sizes are temperature dependent and vary significantly making cluster algorithm still inefficient. There will be many threads waiting until the largest cluster has been formed. To fully comprehend this, imagine that in a system with size  $L = 16$  having 256 spins, on one thread the cluster has 20 spins, but on another thread a cluster has 120 spins. On the first thread with a smaller lattice size, the search for spins will end much earlier than for the larger cluster size. Therefore, before we can send all the information back to CPU, we have to wait for the thread which forms the largest cluster and thereby take the longest time to finish. One could consider other methods to work around this, however we have used the algorithm as it is and the time spent by the cluster kernel is the time spent in forming the largest cluster.

Nonetheless, the equilibration speed up we gain from the Houdayer cluster algorithm is greater in magnitudes compared to the efficiency loss on a GPU. This fact motivates us to use the cluster algorithm on GPUs. Here we would like to mention that the speed up in spin-flip times is still 100 times larger compared to a single CPU. We will discuss performance in a later part of this section. In Fig. 4.4, we show a full schematic diagram of the implementation of Metropolis and HCA on GPU. Parallel tempering is done on a CPU, hence it is not shown in this figure.

Now we summarise the full algorithm including Metropolis, parallel tempering and Houdayer cluster algorithm in the following steps:

1. Initialise all variables in the same way as described for the Metropolis update.
2. Start the Monte Carlo loop for Monte Carlo steps.
3. Call the Metropolis kernel to update the spins parallelly on each thread given by a coordinate as seen in Fig. 4.3
4. Copy the required arrays like energies etc. to the host for measurements.
5. Call the cluster algorithm kernel for forming the cluster and updating the spins according to the Houdayer cluster algorithm.
  - The overlap configurations are formed by  $q_{ii}(i, j, k) = s_{ii}(i, j, k)s_{ii}(i, j, k)$ , where  $ii$  is the spin index running from 0 to  $L^2 - 1$ .

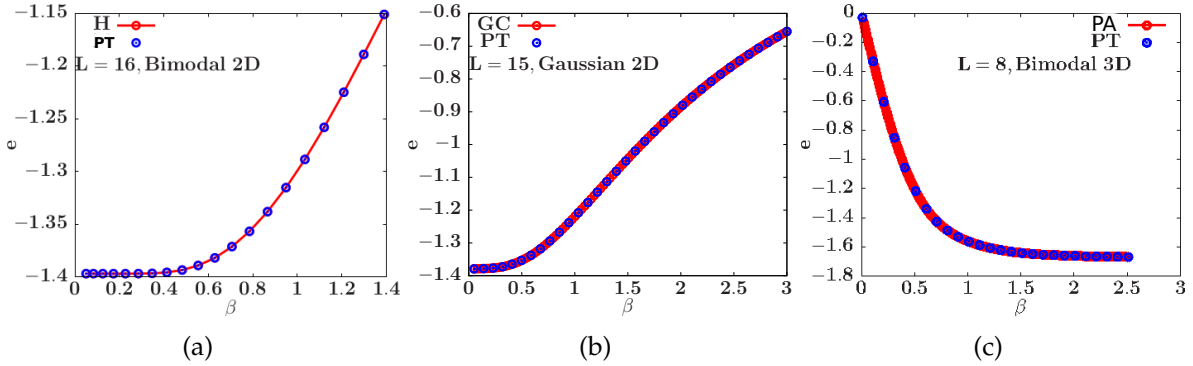


Figure 4.5: Benchmarking energies for: (a) two dimensional spin glass with bimodal couplings; (b) two dimensional spin glass with Gaussian couplings; (c) three dimensional spin glass with bimodal coupling. The blue data is from different sources which are discussed in the text.

- After the spins are flipped according to the Houdayer cluster algorithm, recalculate the energies.
6. Run a loop for  $N_T$  temperatures to perform one parallel tempering update for a pair of neighbouring temperatures on the host.

## 4.2 Verification of the physical results

The implementation described in Sec. 4.1 needs to be tested for producing the physical results. Therefore, we use average energies as the benchmarking variable to test program. In Fig. 4.5, the blue data is from our simulations and the red data is either from the literature or produced by other methods. For example in Fig. 4.5(a) we compare our results to those found in Ref. [195] for a bimodal two-dimensional spin glass of system size  $(16 \times 16)$ . The data is similar within errorbars, however, the errorbars are too small to be observed on the plot. In Fig. 4.5(b), we show energies as a function of temperature for the spin glass with Gaussian couplings. The red data line is produced by an exact method and the blue data points are the results from our simulations on GPUs. For this case too we find an excellent agreement between these results. In Fig. 4.5(c) of the panel, we show results for a three-dimensional system with bimodal couplings. Here we show a comparison between the results from population annealing algorithm [196]. Results for all these cases show excellent agreement. Hence, we conclude that for the energy calculations or for finding the ground states, the program can be used in its current state.

## 4.3 Performance

To test the performance of our implementation, we measure the average spin-flip time given by:

$$t_{\text{psFlip}} = \frac{t_{\text{av}}}{N_T N_R N_C N_{\text{MCS}} N} , \quad (4.5)$$

where  $t_{\text{av}}$  is the wall clock time spent on the kernel during the simulation,  $N = L^d$  is the number of spins with  $d$  being the dimension of the system and  $N_{\text{MCS}}$  is the number of Monte Carlo steps in the simulation. We measure the time of different kernels in the code to analyse the performance for each kernel. The measurements are done on NVIDIA GTX 1080 GPU. In Ref. [194], it was shown that multi-spin coding gives a vast improvement in performance. However, for the use of the Houdayer cluster algorithm (HCA) one has to unpack the spins again. It has to be tested how much damage such unpacking would do to the multi-spin code.

The GPU algorithm is tested for the spin glass with bimodal coupling in 2D and 3D. The 2D model is also tested for the system with Gaussian couplings.

### 4.3.1 Two-dimensional system with bimodal couplings

In this case the bonds can take  $\pm J$  values which are randomly picked from a bimodal distribution. In Fig. 4.6, the performance of the algorithm is illustrated in multiple sub-figures. In the upper row, we analyse the performance of the Metropolis algorithm. Fig. 4.6(a) demonstrates the dependence of the spin-flip time on the system size. The horizontal axis shows the number of Monte Carlo steps. It is evident from the figure that after approximately  $2^6$  MCS the system equilibrates in the spin-flip times. In Fig. 4.6(c), spin-flip times are plotted as a function of the system size. We observe that for smaller system sizes spin-flip times are large. After a certain system size ( $L \approx 30$ ), the spin-flip times settle to a constant value. This is due to the fact that the larger system sizes have more work to do in the spin flipping and spend more time on the GPUs. Therefore the data is not synchronised very often with the host device (CPU). The smaller systems sizes have less spins to flip and need to synchronise more often with the host device. Fig. 4.6(b) in the top row shows the performance as a function of filled blocks on the GPU. The  $\eta$  is the efficiency given by:

$$\eta = \frac{t_{\text{psFlip}}^{\text{max}}}{t_{\text{psFlip}}} . \quad (4.6)$$

$t_{\text{psFlip}}^{\text{max}}$  is the maximum spin-flip time. When  $\eta$  is unity, the program is most efficient. Note that the spin-flip times varies with the number of blocks filled on the GPU. Using the value of  $\eta$ , we can identify the number of blocks for which the program is most efficient. Therefore, as a consequence of the GPU design, the number of

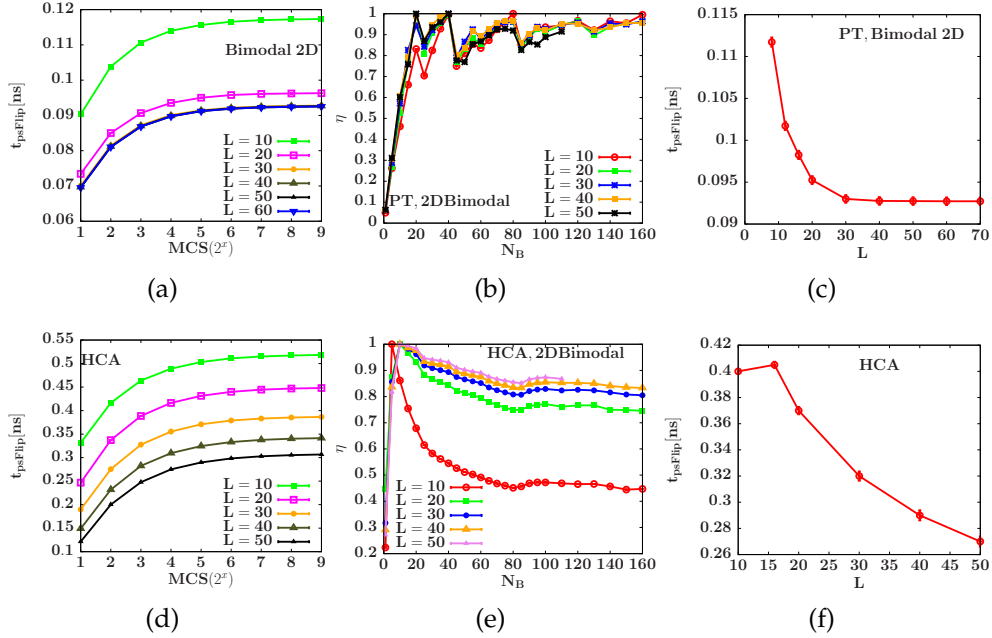


Figure 4.6: In first column, the spin flip time is shown as as function of Monte-Carlo steps. In the middle column, the inverse of spin flip time for the peak performance for three different system sizes is demonstrated for a system with bimodal couplings in 2D.

thread blocks is chosen in a way that all multiprocessors are fully filled, the performance is maximised. Therefore, we expect the same behaviour from our program. In Fig. 4.6(b), we observe that the performance is best when the number of filled blocks is a multiple of the GPU multiprocessors. This is the ideal behaviour as described by the CUDA developers. In the bottom row of 4.6, we look at the performance of the Houdayer cluster algorithm (HCA). Fig. 4.7(d) has the same axis as Fig. 4.6(a). We see a more systematic increase in spin-flip times with growth in the system size. We can understand this as we expect the cluster sizes to get larger for larger system sizes and the variance in the clusters sizes will be greater. Hence, the performance will be weaker. In Fig. 4.7(f), we observe the  $L$  dependence of the spin flip times. We see larger error bars, hinting at the vast fluctuations. In Fig. 4.7(e), the dependence of the performance on the number of filled blocks on GPU is shown. It is evident that the best performance is unique. There is a single peak and when all the multiprocessors are filled once. If one compares Figs. 4.6(b) and 4.7(e), it can be concluded that the best performance is when each multiprocessor is filled once. For the Metropolis there are multiple peaks with maximum efficiency. However, there is a unique peak for HCA. This peak as evident in Fig. 4.7(e) is for all system sizes larger than  $L = 10$  at a single point.

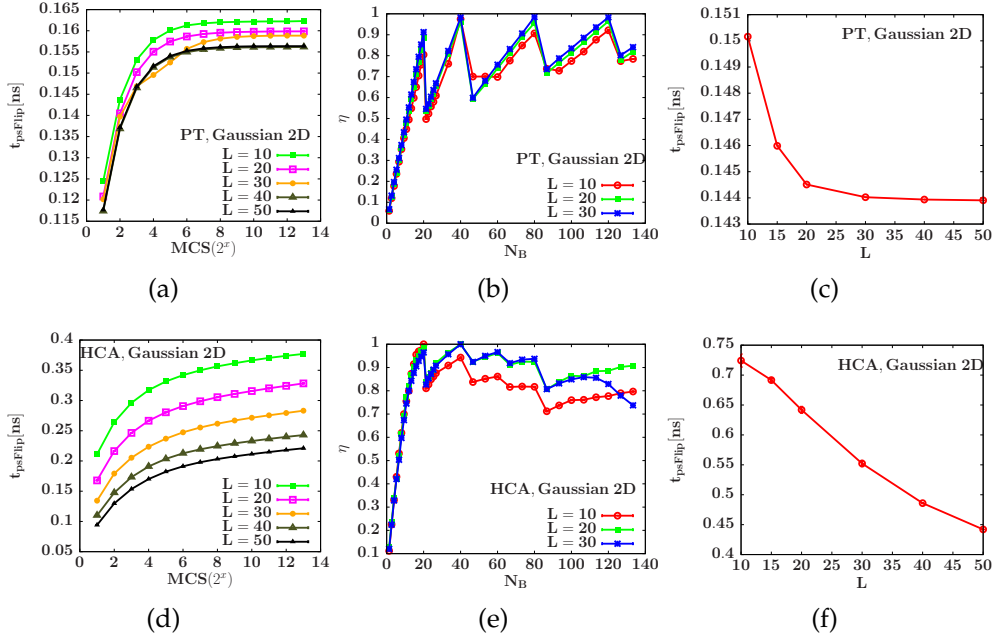


Figure 4.7: Same as in Fig. 4.6, but for a system with Gaussian couplings in 2D.

### 4.3.2 Two-dimensional system with Gaussian couplings

In this part, the performance results for the Gaussian couplings are discussed. In figure 4.7, the performance of the algorithm is illustrated in multiple sub-figures. In this case, the couplings are generated from a Gaussian distribution with zero mean and unit variation. As explained above, in the top row, we analyse the performance of the Metropolis algorithm. There are no anomalies in the left figure. In the top right figure, spin-flip times are plotted as a function of the system size. We observe a flattening of the spin flip times with respect to the system size within the error bars. The middle figure of the top row shows the performance of GPU as a function of filled blocks on the GPU. The efficiency  $\eta$  behaves as expected from the CUDA. For HCA in the lower panel, we observe a systematic growth in the spin-flip times. For the Gaussian case, error bars are smaller in the bottom right figure. This could be because, for the bimodal case, we have a very high degeneracy, hence many possibilities of forming different clusters. In the middle of the bottom panel, the dependence of the performance on the number of blocks is shown. There is a single peak and when all the multiprocessors are filled once. One also sees that if we fill  $2N_B$  multiprocessors, the efficiency is still good but not for all system sizes.

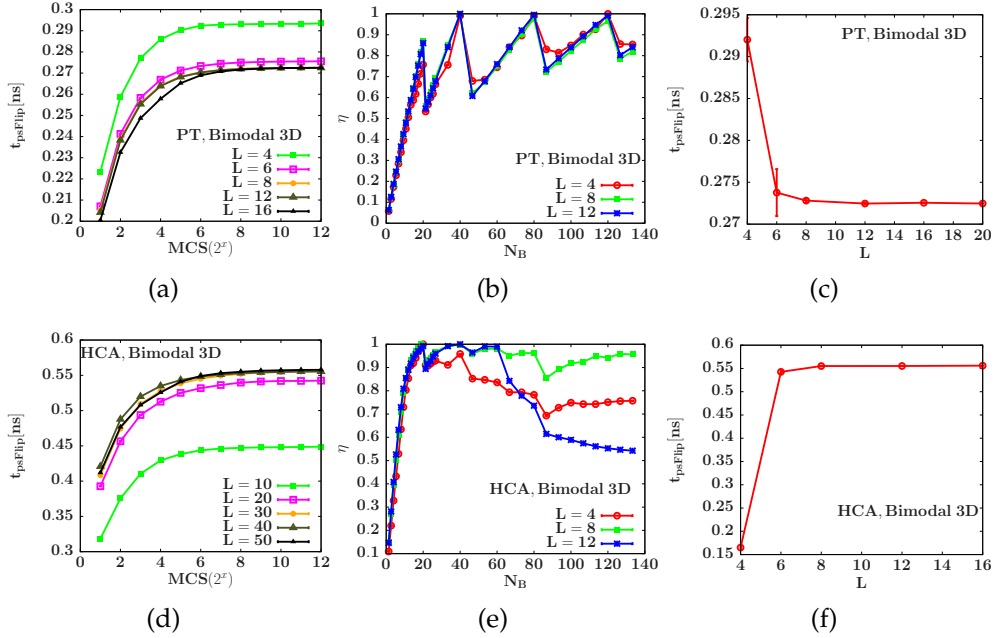


Figure 4.8: The performance plots for 3D spin glass with bimodal couplings.

### 4.3.3 Three-dimensional system with bimodal couplings

We also tested the code for a three-dimensional spin glass system with bimodal couplings. We demonstrate the performance analysis in Fig. 4.8. All the subfigures represent the same analysis as in Figs. 4.6 and 4.7. The spin-flip times are larger compared to the two-dimensional case. There are no anomalies in this case. The spin-flip times become consistent for the larger system ( $L > 8$ ) sizes. In Fig. 4.8(a), the behaviour is similar to the two-dimensional system. As a consequence the value of spin-flip time settles down to a constant around the same number of spins ( $8^3 20^2$ ) for the both three dimensional and two dimensional cases in Fig. 4.8(c). The efficiency  $\eta$  also follows the CUDA benchmarked behaviour in Fig. 4.8(b).

The behaviour of  $\eta$  for the cluster algorithm in three dimensions is also similar to the two dimensional in 4.8(e), however the spin-flip times are saturating to a constant value in Fig. 4.8(f). The reason behind this different behaviour could be that the Houdayer cluster algorithm in three-dimensions has some drawbacks and does not work similarly as in two dimensions. The three-dimensional system is listed here for completeness, it is evident that the method represented in this chapter can be used to simulate a three dimensional system, however for the cluster algorithm further investigations are required. In this thesis, the central point of the research is the two dimensional spin glass. Therefore, no further investigation about the cluster algorithm is discussed here. It should be noted that the peak performance for the cluster algorithm is always taken from the second peak where the number of blocks is twice the number of multiprocessors.

### 4.3.4 Parallel tempering on CPU

It is mentioned above that the Metropolis and cluster algorithms are simulated on GPUs, however the parallel tempering part of the code is done on CPU. Irrespective of the dimension, for the same number of temperatures the cost in terms of time on a CPU is the same. Therefore, instead of repeating the same plot three times here, we discuss only the two dimensional spin glass with bimodal couplings in Fig. 4.9. Parallel tempering swaps happen only  $N_T - 1$  times, whereas the spin flip sweeps happen  $L^2$  times. Swap to sweep ratio for larger system sizes is tiny. Therefore, the total time is not as much affected by the parallel tempering. We plot the time spent in parallel tempering in each swap normalized by  $L^2$  in Fig. 4.9. It is visible that for the larger system sizes the time spent in parallel tempering differs by an order of magnitude from spin flip time. The total time spent in one spin-flip in the program can be written as:

$$t_{\text{psFlip}}^{\text{total}} = t_{\text{psFlip}}^{\text{Metropolis}} + t_{\text{psFlip}}^{\text{HCA}} + t_{\text{pt}}. \quad (4.7)$$

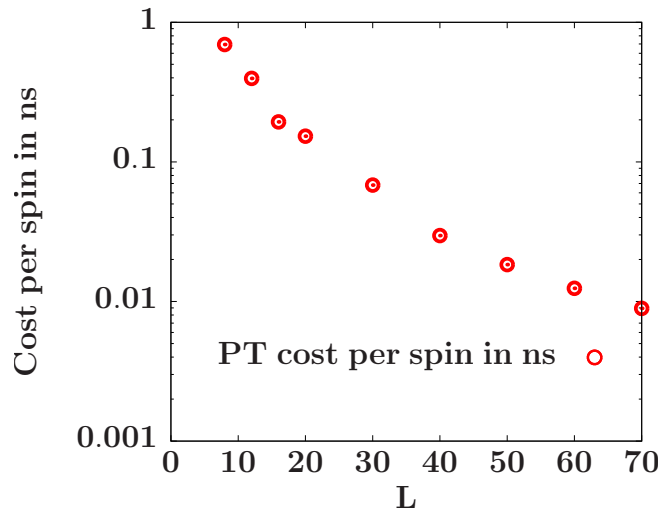


Figure 4.9: The cost of parallel tempering calculated per spin.

## 4.4 Summary

We demonstrated that parallel tempering and the Houdayer cluster algorithm can be used to simulate disordered systems on massively parallel architectures. Due to the favourable relation of performance to price and power consumption in GPUs, they become the natural testing platform for our problem. To be representative of typical installations accessible to users, we used Nvidia GPUs from the consumer

series (GTX 1080). The code was also tested on a professional computing card (Tesla K20m), however the spin flip times were half as fast as on the GTX 1080 which have almost double the multiprocessors as compared to the Tesla K20m. In comparison to a single CPU core a speed up of 220 times was gained for the Metropolis kernel of the algorithm. Systems like spin glass are parallel in nature due to the large number of disorders required to get an averaged physical result.

We observe that a two-dimensional spin glass with Gaussian couplings has larger spin flip times compared to the case with bimodal couplings. This is because the bonds are floats and all the physical variables turns out to be floats. For the cluster-algorithm speed up is between 50-80 times. This is not as good as the Metropolis, however this is still an excellent improvement. We also tested the time spent in swapping of temperature indices and energies in the parallel tempering. The time spent per spin in the parallel tempering is at least an order of magnitude smaller. Therefore, doing the parallel tempering on CPU does not make the implementation inefficient.

For three dimensional systems the speed up is about 140 times compared to the serial CPU code. The cluster algorithm in this case is just for the purpose of demonstration of the implementation. There are some problems associated with the efficiency of this algorithm for three dimensional spin glass systems [186, 187]. Further studies and tests are required to use this algorithm for three dimensions. In this thesis three dimensional spin glasses are not investigated, therefore this implementation can be used as is. We use this method to study the random-field Potts model and two dimensional spin glasses in the next chapters.

# Chapter 5

## Approximate ground states in the random-field Potts model

The random-field Potts model (RFPM) was introduced in Sec. 2.2.2. In this chapter, we investigate the ground state (GS) of the RFPM using the graph cut (GC) method. The results of the energy minima produced by this heuristic algorithm are compared to those found by an appropriately tuned parallel tempering (PT) method that is configured to find ground states for the considered system sizes with high probability. Interestingly, it is observed that as a trend, the GC method found the same states in a fraction of the time. In fact in some cases, the PT method manages to find better estimates of the energy minima as compared to the GC, but the caveat is that the running time grows at least exponentially with system size and is applicable for restricted system sizes. The GC method on the other hand efficiently computes good quality local energy minima, close to the exact GS. The run-time typically scales linearly with the system size, which, therefore, allows to simulate large systems. Consequentially, for a first exploratory study of the RFPM, the GC method is used in  $d = 2, 3$ .

The work presented in this chapter has been published in Ref [197]. This chapter is an overview of the same work and is organised as follows. In Sec. 5.1, the model and our methodology for studying the GS problem is described. Specifically, we describe the parallel PT method. In Secs. 5.2 and 5.3, the detailed numerical results for the GS study of RFPM are presented, using GC method and are compared to the GS results of the GC method to the corresponding results from the PT method. Finally we conclude the chapter in Sec. 5.4

### 5.1 Model and methodology

In Chap. 2.2.2, two different Hamiltonians for RFPM were introduced. For completeness, we describe here the variant of the Hamiltonian used in this study. Two

numerical approaches, the graph-cut approach and parallel tempering are used for determining ground states of samples.

### 5.1.1 Random-field Potts model

The Hamiltonian [90] describes the ferromagnetic  $q$ -states Potts model

$$\mathcal{H} = -J \sum_{\langle ij \rangle} \delta_{s_i, s_j},$$

where the  $s_i \in \{0, 1, \dots, q-1\}$  are the Potts spins, and  $\langle ij \rangle$  denotes summation over nearest neighbours only. The present study is done on square and simple cubic lattices with periodic boundary conditions. As described in Sec. 2.2.2, the coupling of the spins to random-fields can take a variety of different forms [96, 98, 102]. A symmetric coupling of continuous fields can be expressed as [96]:

$$\mathcal{H} = -J \sum_{\langle ij \rangle} \delta_{s_i, s_j} - \sum_i \sum_{\alpha=0}^{q-1} h_i^\alpha \delta_{s_i, \alpha}, \quad (5.1)$$

where  $\{h_i^\alpha\}$  denotes the quenched random-field at site  $i$  and on state  $\alpha$ . Hence, in this model, the random-field at each site has  $q$  components, and we take each of these to follow a normal distribution. To separate the disorder strength from the random instance we define  $h_i^\alpha = \Delta \epsilon_i^\alpha$  and  $\epsilon_i^\alpha$  are then drawn from a standard normal distribution, i.e.,

$$P(\epsilon_i^\alpha) = \frac{1}{\sqrt{2\pi}} \exp\left(-\epsilon_i^{\alpha 2}/2\right). \quad (5.2)$$

For the case  $q = 2$ , the Hamiltonian in Eq. (5.1) has two different random-fields  $h_i^0 \equiv h_i^+$  and  $h_i^1 \equiv h_i^-$  for the two spin orientations. On other side the usual definition of the RFIM has only one random-field acting on a particular spin [198]. For this case the Hamiltonian given by Eq. (5.1) can be written as

$$\mathcal{H} = -\frac{J}{2} \sum_{\langle ij \rangle} [\sigma_i \sigma_j + 1] - \frac{1}{2} \sum_i [(h_i^+ + h_i^-) \sigma_i + (h_i^+ - h_i^-)],$$

where  $\sigma_i = \pm 1$  are Ising spins. Hence, it can be concluded that up to a constant shift, the two states RFPM of Eq. (5.1) and with the distribution given by Eq. (5.2) at coupling  $J$  and random-field  $\Delta$  is equivalent to the random-field Ising model (RFIM) at coupling  $J/2$  and field strength  $\Delta/\sqrt{2}$ .

In Chap. 2, an alternative model with a discrete distribution of disorder is also introduced. However, for this study, the model was restricted to Eq. (5.1). It should be noted that for the continuous form (5.1) a unique ground state is expected, while the alternative form in Eq. (2.27) might admit (extensive) degeneracies depending

on the choice of  $\Delta$ . While the discreteness of the form Eq. (2.27) might have some advantages for the efficiency of simulation codes, any possible subtleties associated with degeneracies should be avoided for development of a new algorithm. Therefore, the Hamiltonian given by Eq. (5.1) is used in this work.

### 5.1.2 Graph-cut method

In Chap. 1 we discussed the NP hardness of finding the GS for RFPM. It is also mentioned that PT is not enough to deal with the problem in the thermodynamic limit. Therefore, an efficient approximation algorithm used in computer science [199] is adopted to the systems with Potts model like Hamiltonians. The method is composed for a general energy function of the form

$$E(\{s_i\}) = \sum_{i,j} V_{ij}(s_i, s_j) + \sum_i D_i(s_i), \quad (5.3)$$

where in the original application  $s_i$  refers to the colour label of the pixels of a (planar) image, but the interaction matrix  $V_{ij}$  can be constructed in a way that also more general graphs and three-dimensional systems can be modelled. The RFPM Hamiltonian in Eq. (5.1) is clearly a special case of this general form. Each site  $i$  is assigned a label  $s_i \in \{0, 1, \dots, q-1\}$ . The function  $V_{ij}(s_i, s_j)$  gives the cost of assigning labels  $s_i$  and  $s_j$  to the sites  $i$  and  $j$ , while the function  $D_i$  measures the penalty (or cost) of assigning the label  $s_i$  to the site  $i$ . The approach taken in Ref. [199] is to put a constraint on the optimisation problems derived from Eq. (5.3) by reducing the  $q$  colours problem to an effective two-colour problem. This is equivalent to the RFIM, the ground state for this constraint problem can be determined exactly and in polynomial time using the established min-cut/max-flow algorithms. The idea in the current study is in the same spirit as the embedding of Ising variables used in combination with minimum-weight perfect matching in dealing with continuous-spin glasses on planar lattices [200, 201].

In Ref. [199] two such approaches proposed are the  $\alpha$ - $\beta$ -swap and the  $\alpha$ -expansion moves. For the  $\alpha$ - $\beta$ -swap one picks two labels  $\alpha \neq \beta \in \{0, 1, \dots, q-1\}$  and freezes all labels apart from  $\alpha$  and  $\beta$ . Hence, this constraint makes the problem (5.3) equivalent to a two-label problem on the sites with labels  $\alpha$  or  $\beta$  that can be solved by min-cut/max-flow. This step is repeated for all pairs of labels, resulting in a *cycle* of  $q(q-1) \approx q^2$  steps. For the  $\alpha$ -expansion move one picks a label  $\alpha$  which is then frozen. All other pixels are given the alternative of either keeping their current label or being flipped into the  $\alpha$  state, which is again a binary choice, and min-cut/max-flow can solve the resulting constraint problem. A cycle of the  $\alpha$ -expansion takes  $q$  steps. In both algorithms, cycles are repeated until the methods have converged to a local minimum and the configurations do not change any further.

$L$	8	12	16	20	24	32	40
$N_T$	16	16	16	16	16	32	32
$\phi$	1.13	1.13	1.13	1.13	1.13	1.14	1.14

Table 5.1: Optimised values of  $\phi$  according to Eq. (3.18) and the number of temperature replicas  $N_T$  for different lattices with  $L^2$  spins used in the parallel tempering.

While the such algorithms do not guarantee to find ground states, they have been reported to yield excellent approximations to the ground states and are extensively used in computer vision. An upper bound on the energy of the local minima can be found for the  $\alpha$ -expansion [199], which is given by

$$E(\hat{f}) \leq 2cE(f^*), \quad \text{where} \quad c = \frac{\max_{s_i \neq s_j} V(s_i, s_j)}{\min_{s_i \neq s_j} V(s_i, s_j)}. \quad (5.4)$$

For the Potts model,  $V_{ij}(s_i, s_j) \equiv -J\delta_{s_i, s_j}$ , yielding  $c = 1$ . So the expansion move provides a local minimum within a factor of two of the global minimum. To check the effectiveness of their algorithms, the authors of Ref. [199] experimented on a variety of computer vision problems such as image restoration with multiple labels, stereo and motion. These problems are solved by computing a minimum cost *multiway cut* on the graph. A comparison of their results with known ground states revealed 98% accuracy [199]. This method has not been applied to RFPM previously. In next sections of this chapter, we benchmark the ground states of a set of chosen disorders via parallel tempering simulations. We compare these ground states to the lowest states given by graph cut method.

### 5.1.3 Parallel-tempering

The RFPM has a rugged free energy landscape with many minima and maxima. The evolving systems get trapped in these meta-stable states, and the system does not relax to the ground state. Any reasonable Monte Carlo sampling, therefore, has to overcome energy barriers and cross from one basin to another to reach the global minimum. Established approaches to achieve this are simulated annealing [202] and parallel tempering [203, 204]. It has been shown that among the Monte Carlo methods parallel tempering consistently outperforms simulated annealing as a tool for ground-state searches in disordered systems [205]. But note that population annealing [206] might be another interesting contender in this respect [205, 207]. We will hence focus on parallel tempering.

In Chap. 4 PT is introduced. The method for tuning the temperature is also discussed in the same chapter. The values of  $\gamma$  exponents used here are listed in table 5.1. As a realisation of Markov chain Monte Carlo that satisfies ergodicity

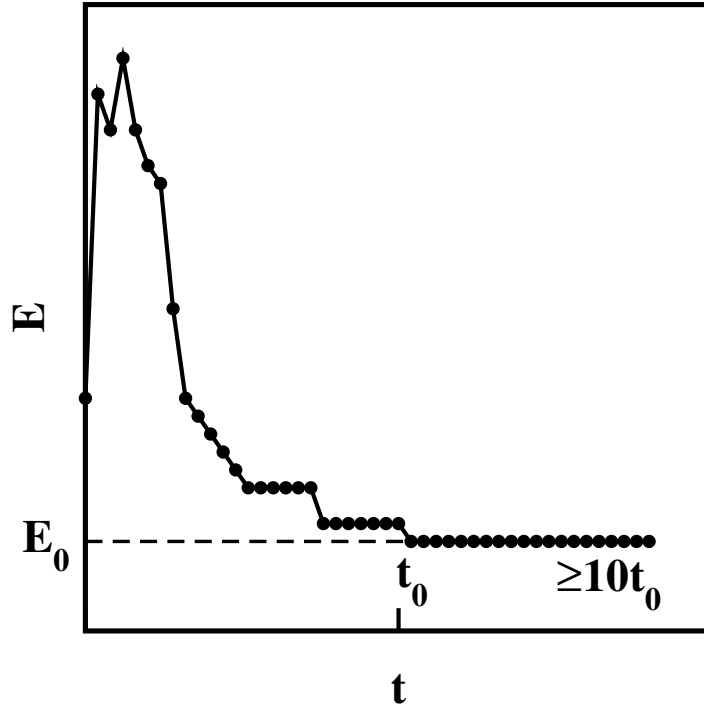


Figure 5.1: Schematic diagram showing the variation of  $E$  with time  $t$  in the PT runs (in MC steps). The first occurrence of the minimum energy  $E_0$  is at onset time  $t = t_0$ . The corresponding state is accepted as a ground state if no lower energy is found up to  $t \geq 10t_0$ .

and detailed balance, PT is guaranteed to converge to the equilibrium distribution. PT performs much better than the local updates alone, however, for systems with complex and rugged energy landscape such as the RFPM the equilibration times can be very long. Moreover, they increase steeply with system size and with lowering  $T_{\min}$ . Therefore, for bench marking the results, the study is constrained to not too large systems. For the considered system sizes, PT can find ground states for the overwhelming majority of the samples. To ensure this, we rely on the following bootstrapping procedure:

1. We run all samples for a given system with side length  $L$  and number of states  $q$  for some initial time chosen to ensure equilibration of an average sample (determined, for example, by measuring the average tunnelling time).
2. For each sample, we determine the onset time  $t_0 = t_0(\{h_i^\alpha\})$ , i.e., the time when the program determines the lowest energy in the run for the first time.
3. We re-run each sample with a run-time of  $t(\{h_i^\alpha\}) = 10 \times t_0(\{h_i^\alpha\})$ .
4. For samples where a new, lower state is found in the extended runs, we repeat this procedure until the condition  $t = 10 \times t_0$  is met for all samples.

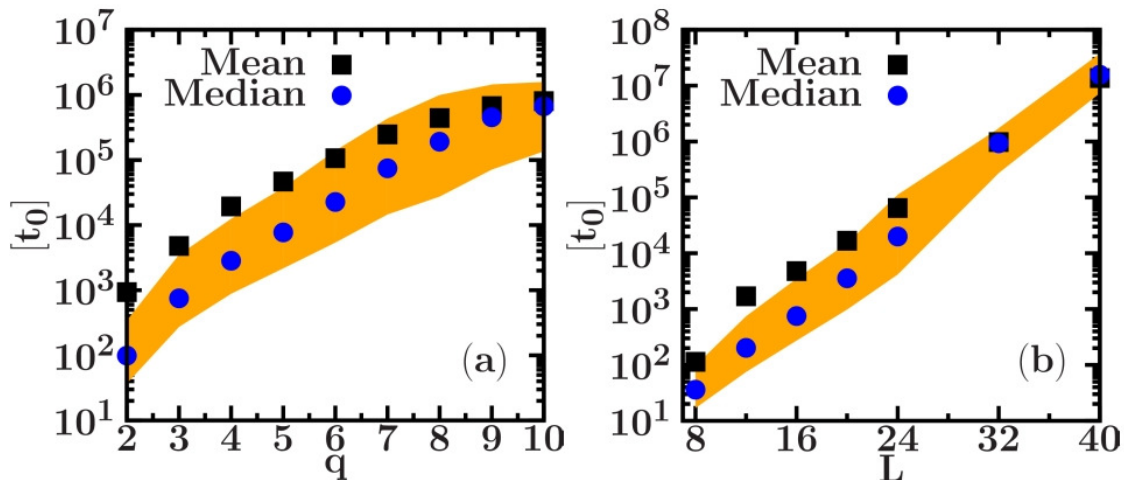


Figure 5.2: Disorder-averaged onset times  $t_0$  for finding the ground states of the  $d = 2$  RFPM using parallel tempering. The data is plotted on a log-linear scale as a function of (a) the number of Potts states  $q$  for  $L = 16$ , and (b) the system size  $L$  for  $q = 3$ . The data are averaged over 1536 realisations of quenched random-fields according to Eq. (5.2) with  $\Delta = 1$ . The shaded area shows the range that contains the onset times for  $2/3$  of the samples.

This procedure is illustrated in Fig. 5.1. This method finds ground states with very high reliability. For the system sizes considered, the failure probability was estimated to be of the order of 1 in 1000. For none of the samples considered here is a state lower than the reference state determined from the procedure above found in any of the other runs (PT or GC).

The simulations are performed for system sizes  $8 \leq L \leq 40$  and number of states  $2 \leq q \leq 10$  for 1536 random-field configurations. The resulting average and median onset times of the ground states are shown in Fig. 5.2. The shaded area indicates the level of disorder fluctuations. These plots are shown on a linear-log scale. In Fig. 5.2(a), we observe that  $t_0$  increases slightly slower than exponentially with the number of Potts states  $q$ . In Fig. 5.2(b), we observe an exponential increase of  $t_0$  for system sizes  $L \geq 16$ . This is expected behaviour for any process tailored to ensure the exact ground states for NP-hard problems. As the mean values are larger than the medians, the distribution is asymmetrical and tail-heavy for all values of  $q$  and  $L$ .

## 5.2 Benchmarks

We first consider the behaviour of the GC method in its own right before turning to a detailed comparison of this technique to the PT method. The bulk of our

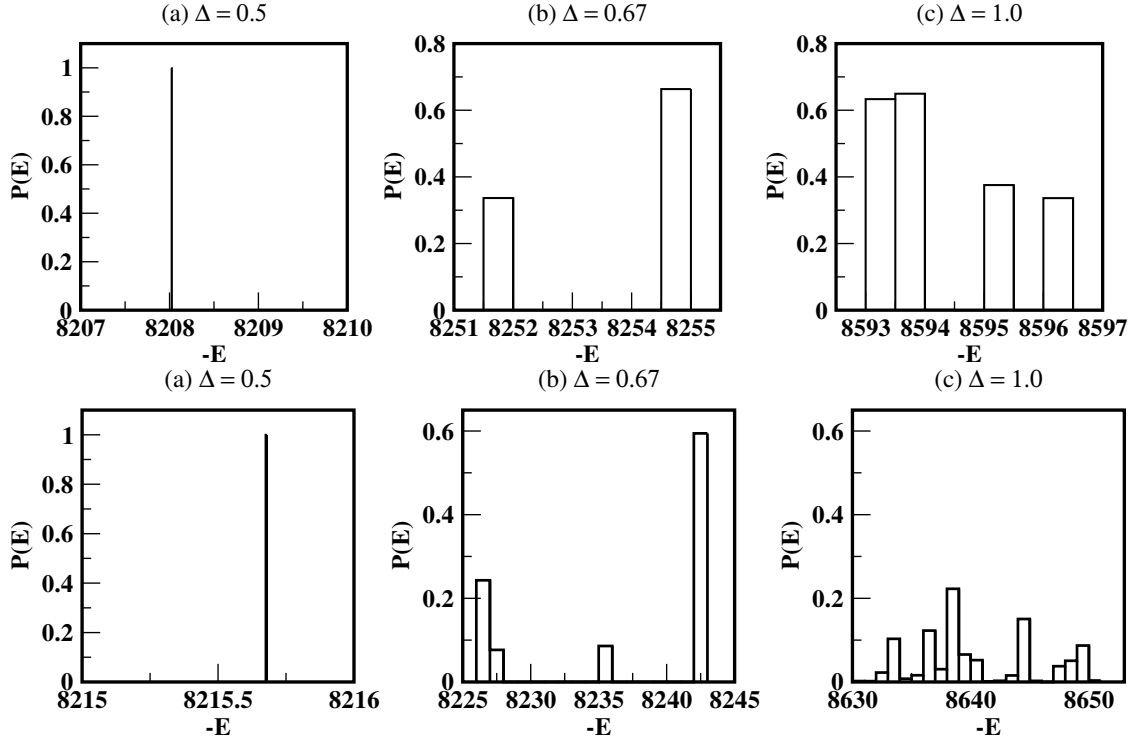


Figure 5.3: Energy histograms of final states obtained from GC for the  $q = 3$  RFPM (top row) and the  $q = 4$  RFPM (bottom row) on a  $64^2$  lattice. The histograms are obtained from 10 000 initial configurations  $\{s_i\}$  for a fixed disorder configuration  $\{\epsilon_i^\alpha\}$ .

runs were performed in two dimensions, but some of the timing runs discussed in Sec. 5.2.3 were repeated for cubic lattices.

### 5.2.1 Approximate ground states from GC

First, the GC method is tested to find the approximate ground states in RFPM. The minimum energy states are recorded for several runs with different initial labelling  $\{s_i\}$  of a fixed disorder configuration  $\{\epsilon_i^\alpha\}$ . Each run might give a different minimum state close to the ground state which is referred to a meta-stable state.

In Fig. 5.3 histograms of the energies to meta-stable states as found from GC method are shown. Histograms for  $q = 3$  and  $q = 4$  with varying  $\Delta$  are shown in the top and bottom row respectively. The minimisation runs are performed on a  $64^2$  lattice for 10000 runs of different initial conditions.  $E = \mathcal{H}(\{s_i\})$  is the total energy of the RFPM from the Hamiltonian in Eq. (5.1) (Note that  $E$  is negative and we have plotted  $-E$ ). For  $\Delta = 0.5$ , the same energy state for several runs of different initial conditions is observed, hence the histogram shows a sharp peak corresponding to that energy state. With the increase in the disorder strength  $\Delta$ , the number of energy

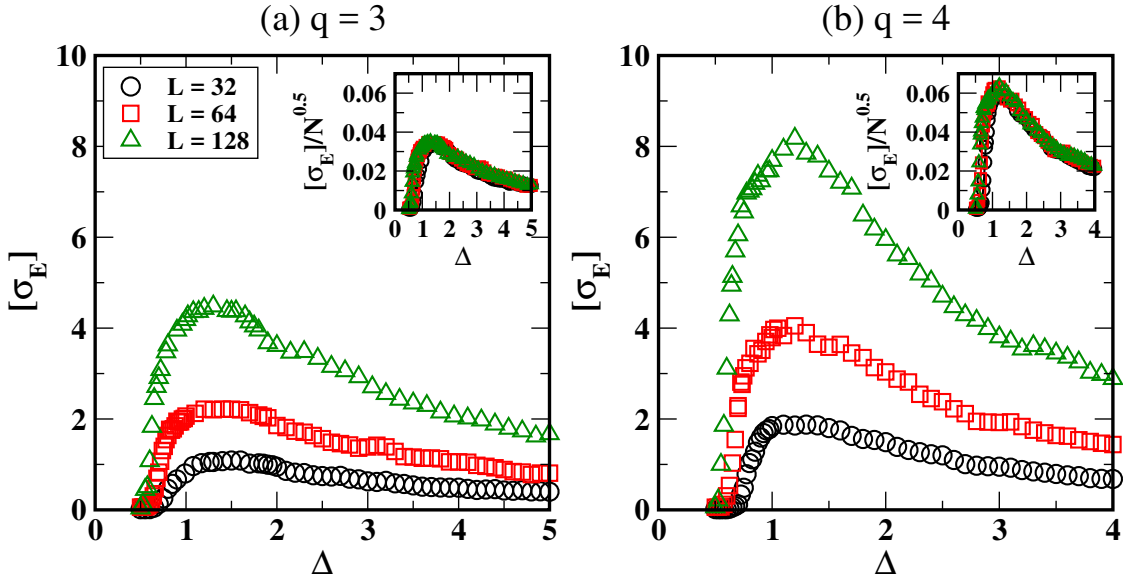


Figure 5.4: Variation of the standard deviation of energy  $[\sigma_E]$  from runs of the GC method as a function of disorder amplitude  $\Delta$  for the  $d = 2$  RFPM with (a)  $q = 3$ , and (b)  $q = 4$ . All data are averaged over 100 disorder realisations  $\{\epsilon_i^\alpha\}$ , and 1000 initial states  $\{s_i\}$  for each disorder realisation. Clearly,  $[\sigma_E]$  grows with lattice size  $L$ , and also with number of states  $q$ . The scaled data in the insets demonstrates that  $[\sigma_E] \sim \sqrt{N} = L$ , i.e., there are no critical fluctuations in this range of  $\Delta$ -values.

states is increased. Therefore, a distribution with width is observed as we move from left to right in the top or bottom row. The GC method, therefore, does not produce the exact ground states of the RFPM. The same behaviour can be observed in the bottom row of Fig. 5.3 for the  $q = 4$  RFPM. However, it can be clearly seen that the histograms are wider as compared to  $q = 3$  and more meta-stable states are observed.

We use the standard deviation in energy,  $\sigma_E = \sqrt{(E - \bar{E})^2}$  to quantify the energy spread in the histogram. The mean of energies obtained for different runs of GC for a given disorder realisation are denoted as  $\bar{E}$ . In Fig. 5.4, the disorder averaged standard deviation  $[\sigma_E]$  in energy is plotted with respect to disorder strength  $\Delta$  for  $q = 3$  and  $q = 4$  RFPM is shown. The system studied is a square lattice ( $L^2$ ) of linear sizes  $L = 32, 64$  and  $128$ . The energy spread is determined from 1000 independent runs for a fixed disorder realisation and then averaged over 100 disorder realisations. It can be observed from the figure that the energy spread grows with increasing  $L$ . In order to check the  $L$ -dependence of  $[\sigma_E]$ , we plot  $\sigma_E/\sqrt{N}$  in inset of Fig. 5.4, which shows a nice data collapse. Therefore,  $\sigma_E \sim \sqrt{N}$ , as  $\bar{E} \propto N$ , it yields the relation:

$$\left[ \frac{\sigma_E}{\bar{E}} \right] \sim \frac{1}{\sqrt{N}}, \quad (5.5)$$

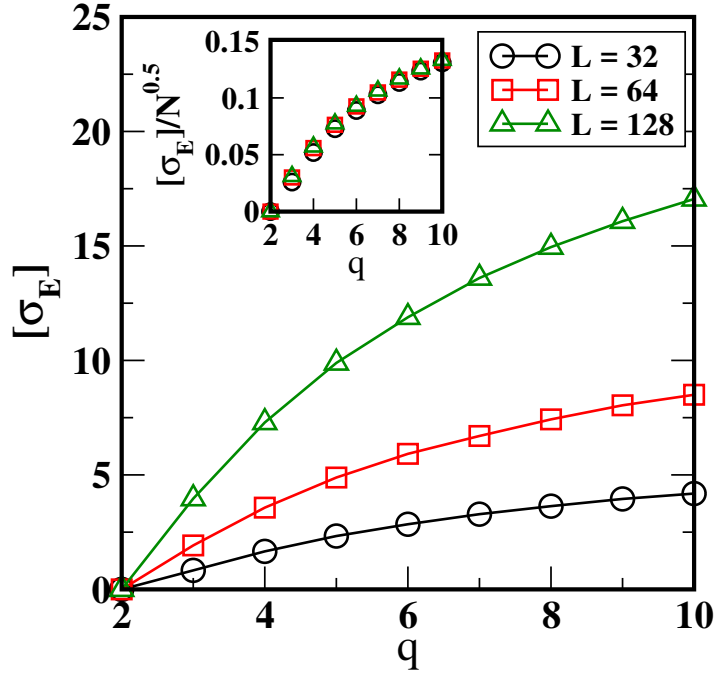


Figure 5.5: Plot of  $[\sigma_E]$  vs.  $q$  for the  $d = 2$  RFPM with  $\Delta = 1.0$ , and indicated lattice sizes. The statistics is the same as in Fig. 5.4. The spread in energy of the GC method states increases with  $q$ . The inset shows that  $[\sigma_E] \sim \sqrt{N} = L$ .

which means that the energy fluctuations about the mean energy will vanish in the thermodynamic limit,  $N \rightarrow \infty$ . The same behaviour is observed for  $q = 3$  (left) and  $q = 4$  (right). However, it is evident that for  $q = 4$ , the energy spread is larger. Therefore, one interesting aspect is to study the energy spread behaviour with respect to the number of Potts states  $q$ . This is shown in Fig. 5.5, where  $[\sigma_E]$  vs.  $q$  is plotted. The data sets correspond to  $\Delta = 1.0$ . The energy spread shows an increase with increasing number of Potts states  $q$ , that implies that the number of meta-stable states increases with increasing  $q$ . As a consequence GC method on average find states of higher energy. The inset of this figure again confirms  $\sigma_E \sim \sqrt{N}$ .

## 5.2.2 Comparisons with PT

In Sec. 5.1.3 of this chapter, a procedure to find the ground states with a very high probability is described. This method is used to create a database of samples for which the ground states are known with very high probability. It is possible to benchmark the GC method against quasi-exact results and PT runs.

In this section, the robustness of the GC method and PT algorithm are tested against each other. To make a direct comparison to the PT simulations the length

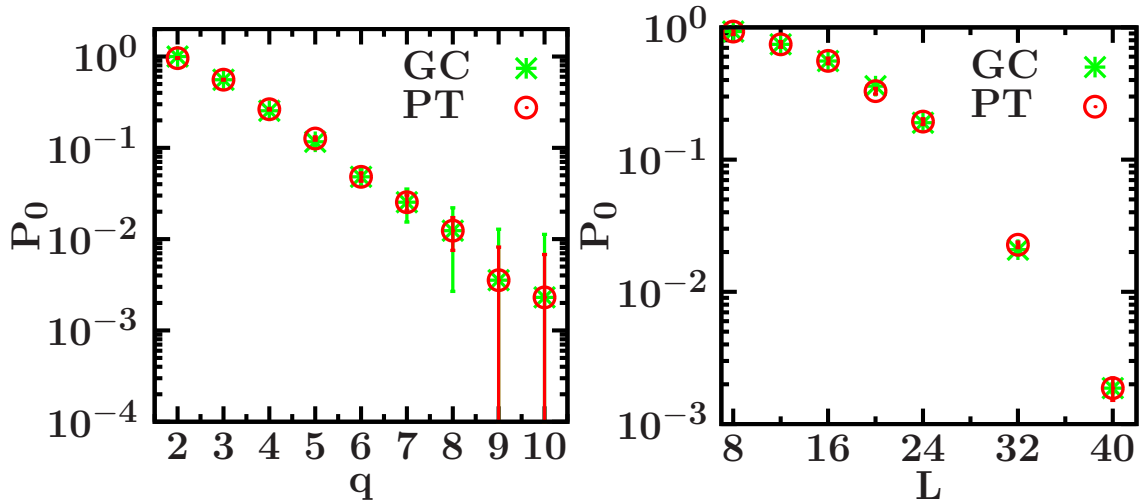


Figure 5.6: Disorder-averaged success probability of finding the ground state from GC and PT runs for 2d RFPM as a function of  $q$  ( $L = 16$ , left panel) and  $L$  ( $q = 3$ , right panel). The GC data correspond to one initial state per disorder sample, while the run-time in PT is adapted to yield exactly the same success probability as the corresponding GC run (see main text). All data are averaged over 1536 configurations of the random-fields.

of simulation is tuned to find the ground state with the same average success probability as the GC method. For a good comparison of the performance of GC and PT, the latter can be tuned via the number of Monte-Carlo steps to give the same average success probability for a given disorder sample as GC. This does not require further computational effort and can be determined from the onset times in Sec. 5.1.3: one can choose the number of steps  $t^*$  for all runs in such a way that the fraction  $n(t_0)/N_s$  of samples with  $t_0 < t^*$  exactly equals the success probability  $P_0$  observed for GC.  $N_s = 1536$  is the total number samples studied. This is illustrated by the data points for PT, also shown in Fig. 5.6, that fall on top of the results for GC.

In Fig. 5.6, we demonstrate the probability of finding the actual ground state with respect to  $q$  (left panel) and  $L$  (right panel). It is observed that the probabilities decay strongly with increasing  $q$  and  $L$ . Both plots show an exponential decay behaviour which is expected from applying a polynomial-time algorithm to an NP-hard problem. It should be noted that the values of  $P(E_0)$  are calculated for GC runs with a single initial condition. It takes only fractions of a second which is much less than the time taken by PT (see the discussion of run-times below in Sec. 5.2.3). In real applications of GC, one would normally perform runs for many initial conditions and pick the state of lowest energy. This approach is a generic method of improving global optimisation algorithms [201, 208]. The success probability of a sequence of

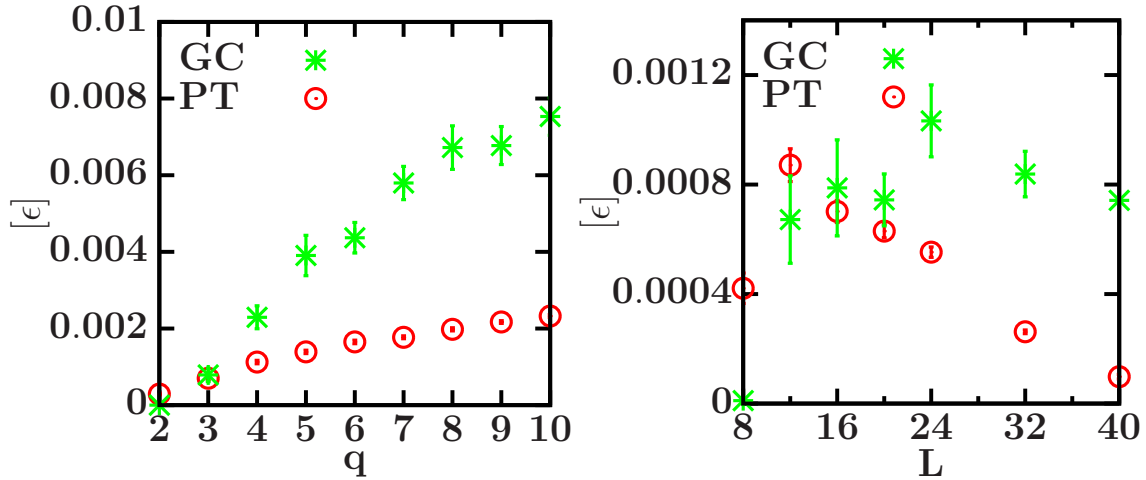


Figure 5.7: Accuracy  $[\varepsilon]$  defined in Eq. (5.7) of GC and PT runs for the  $d = 2$  RFPM with  $L = 16$  as a function of  $q$  (left panel,  $L = 16$ ) and  $L$  (right panel,  $q = 3$ ), respectively. Both methods are tuned to have the same success probabilities, as shown in Fig. 5.6. The data are averaged over 1536 disorder realisations with  $\Delta = 1.0$ .

$m$  runs with different initial conditions follows an exponential,

$$P_s(\{h_i^\alpha\}) = 1 - [1 - P_0(\{h_i^\alpha\})]^m. \quad (5.6)$$

Hence for a certain target success probability  $P_s$ , the required number of runs follows from

$$m(\{J_{ij}\}) = \log[1 - P_s] / \log[1 - P_n(\{J_{ij}\})].$$

For the  $P_0 = 0.00187$  for  $q = 3$  and  $L = 40$  shown in the right panel of Fig. 5.6, for example, using  $m = 2460$  runs ensures  $P_s = 0.99$

While the success probabilities of one GC run and the PT simulation with  $t^*$  steps are identical, this does not imply that the both methods find the same states where they do not find the ground states. Therefore, it is important to quantify the quality of approximation in these cases. In this work, the relative excess energy of the minimum energies returned by both algorithms above the ground state is used as the quality of approximation,

$$\varepsilon = \frac{E_{\min} - E_0}{E_0}. \quad (5.7)$$

This quantity is called *accuracy*. In Fig. 5.7 we show this quantity as a function of  $q$  for a fixed  $L = 16$  in the left panel and as a function of  $L$  for fixed  $q = 3$  in the right panel. The accuracy at the same success probability is approximately comparable as a function of  $L$  and for  $q = 3$  in the considered regime. The accuracy from PT seems to be better compared to the accuracy from GC. Note that  $[\varepsilon] = 0$  for GC at  $q = 2$  as this method finds exact ground states for the RFIM.

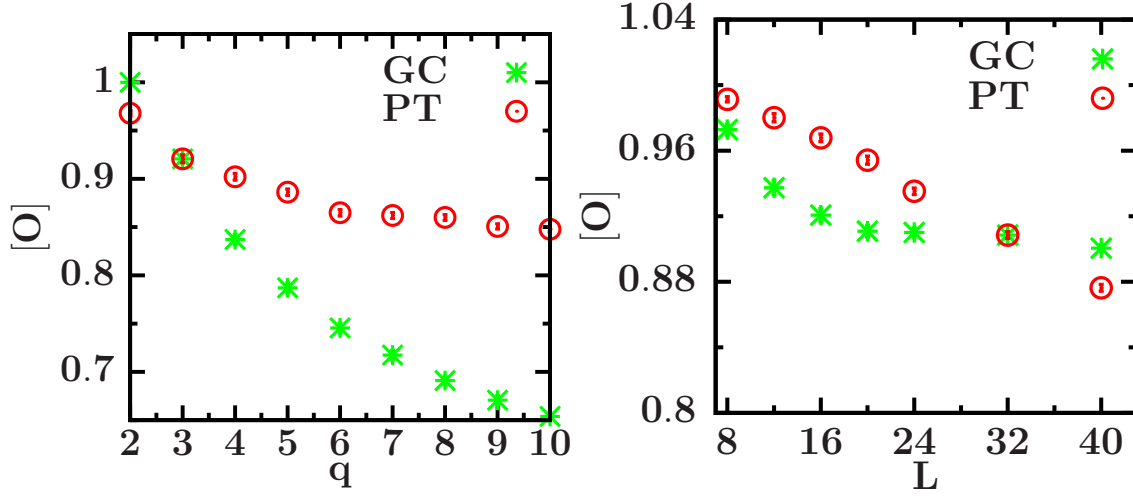


Figure 5.8: Average overlap  $[O]$  (see Eq. (5.8)) of the states returned by GC and PT, respectively, with the true ground states for the  $d = 2$  RFPM as a function of (a)  $q$  for  $L = 16$ , and (b)  $L$  for  $q = 3$ . The averaging is done over 1536 disorder realisations with  $\Delta = 1.0$ .

### 5.2.3 Run times and computational complexity

The accuracy of both the models is of the same order for both methods. Therefore, a crucial question is to know the overlap between the ground states. Are the states found by GC method or PT close to the ground state or far in the configurational space? The overlap is defined as:

$$O = \frac{1}{N} \sum_i \delta_{s_i, s'_i} \quad (5.8)$$

where  $s_i$  and  $s'_i$  are the spins at site  $i$  in the ground state spin configuration and GC method or PT lowest state spin configuration. In Fig. 5.8, average overlap between the ground state and the GC method lowest states is shown as a function of  $q$  and  $L$ . In Fig. 5.8 (right), We observe that for a fixed system size, the overlap between the lowest states from GC method or PT and the ground states decreases with the system size  $L$ . For a relatively small system size ( $L = 16$ ), the overlap of lowest energy state of PT and the ground state is always larger than 85% even for the larger  $q$  values. But, for GC method it drops rapidly to 65% for  $q = 10$ . For a fixed value of  $q = 3$  in Fig. 5.8 (left), we see that the overlap is larger than 90% for PT and GC method, but the fall is steeper for PT. For  $L < 32$ , we notice that the overlap with respect to PT is larger than the GC method for the same  $L$  values. The overlap value saturates for  $L \geq 20$ . Appropriately at  $L = 32$ , we observe a crossover between GC method and PT. Here, we can conclude that the fall in the overlap of GC method is slower compared to PT. Hence for the larger system sizes GC method is a better method compared to PT. Now we discuss the time taken

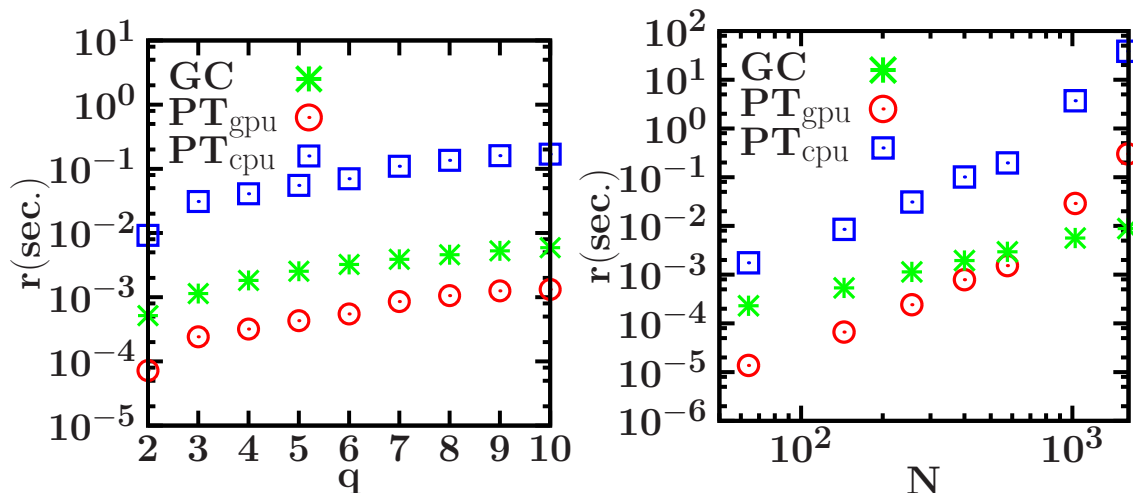


Figure 5.9: Disorder-averaged run-time  $[r]$  of the GC method for the 2d RFPM as compared to CPU and GPU implementations of the PT method tuned to achieve the same success probability.

by the GC method to find an approximate ground state of the RFPM. We measure the CPU time  $r$  (in seconds) that the  $\alpha$ -expansion variant of GC used here takes to reach its final state. We ran our codes on an IBM cluster with 2.67 GHz Intel Xeon processors. The simulations are performed for  $\Delta = 1.0$ , and  $r$  is averaged over 1000 disorder samples. Fig. 5.10 (top row) shows the run-time  $[r]$  for the  $q$ -state RFPM in  $d = 2$ . We plot  $[r]$  as a function of (a) the total number of spins  $N = L^2$  for  $q = 10, 50, 100$ ; and (b)  $q$  for  $L = 128, 256$ . The solid lines are power-law fits with the specified exponent. Clearly,  $[r]$  is linear in  $N$  and  $q$  for the  $q$ -state RFPM. This is in line with the general discussion of the time complexity of the method given in Sec. 5.1.2. A similar analysis for the RFPM in three dimensions is summarised in the bottom row of Fig. 5.10 which shows that also in this case the run-time is approximately linear with respect to  $N$  and  $q$ .

We finally consider the scaling of run times of the GC and PT techniques with the latter scaled to achieve the same success probability in finding ground states as the former. We compare the timings of the GC method to two different implementations of PT, one regular CPU code and a highly optimised implementation on graphics processing units (GPUs) as discussed in 4. The GPU code is slightly faster than GC for small systems, but for larger system sizes the GC approach becomes more favourable as PT shows a clearly super-linear increase of run-times there. For the system sizes probably used in practical studies that are significantly larger than the sizes than the  $L \leq 40$  considered with quasi-exact ground states here, we expect a substantial advantage for GC over PT. The GPU code is about 128 times faster than the CPU implementation. The corresponding run times for the two-dimensional RFPM are shown in Fig. 5.9, using an Nvidia GTX1060 GPU. The times for the GC approach depend linearly on  $q$  and  $N = L^2$  to a very good approximation as

already seen above. The CPU variant of PT is always significantly slower than GC at the same success probability.

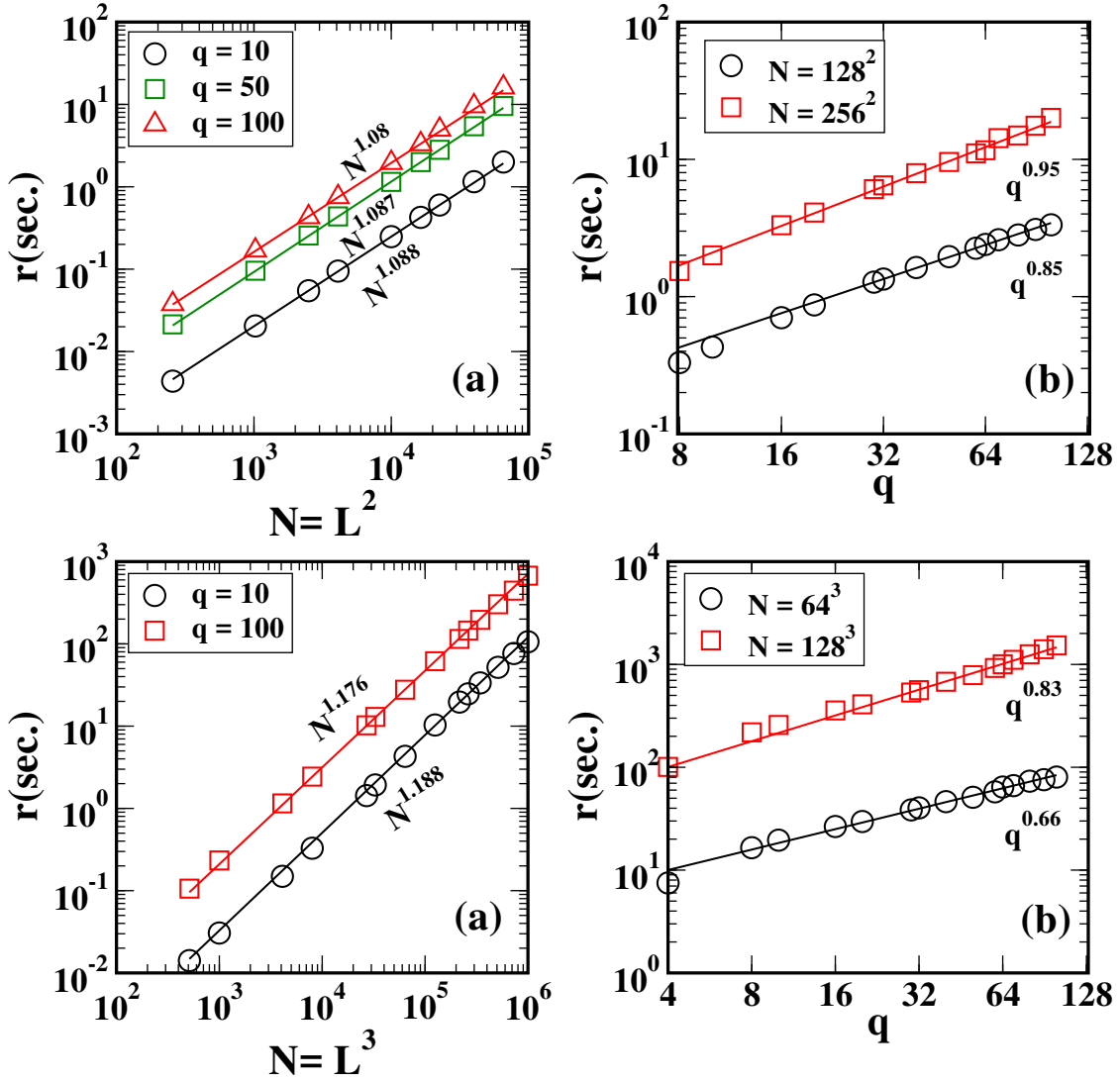


Figure 5.10: Disorder-averaged run-time  $[r]$  (in CPU sec.) for determining the final state by the application of the  $\alpha$ -expansion GC method to the RFPM in two dimensions (top row) and three dimensions (bottom row) as a function of the number of spins  $N = L^d$  and the number of states  $q$ , respectively. The data are averaged over 1000 disorder realisations with  $\Delta = 1.0$ . The solid lines are power-law fits with the specified exponents, and demonstrate that the run-time is linear in  $N$  and approximately linear in  $q$ .

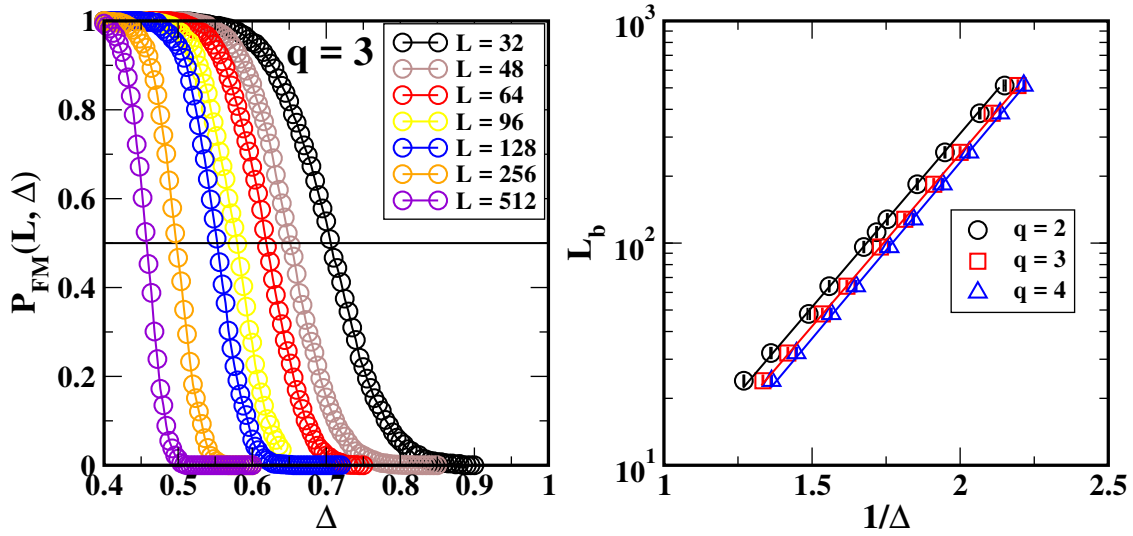


Figure 5.11: (a) Disorder-averaged probability  $P_{\text{FM}}(L, \Delta)$  of samples of the 2D RFPM to have purely ferromagnetic ground states. The data are averaged over 100 configurations of the random-fields. (b) The breakup length scale  $L_b$ , defined as the system size  $L$  where  $P_{\text{FM}}(L, \Delta) = 0.5$ , versus the inverse random-field strength  $1/\Delta$  for  $q = 2, 3$ , and 4. The solid lines show fits of the functional form  $L_b \sim e^{A/\Delta}$  to the data, where  $A = 3.6 \pm 0.03$ .

### 5.3 Scaling of the breakup length

We finally consider an application of the methods outlined above to exploring the physical properties of the RFPM in two dimensions. Given the absence of finite-temperature ordering in the 2d RFIM [209], it seems fairly clear that the RFPM also does not admit order at  $T > 0$  [96]. Instead, one expects the presence of ferromagnetic domains that break up at a length scale  $L_b(\Delta)$  similar to what is observed for the RFIM [209, 210]. At very small disorder, the ground state is purely ferromagnetic where all spins have the same label, while at large disorder the ground state breaks into domains of  $q$  labels. To determine  $L_b$ , we follow Ref. [210] and count the fraction of samples with a purely ferromagnetic ground state, defining the probability  $P_{\text{FM}}(L, \Delta)$ . This quantity is shown in Fig. 5.11(a) as determined from GC for  $q = 3$  and a number of different lattice sizes  $L$ . The breakup length  $L_b$  can then be defined from the condition  $P_{\text{FM}}(L, \Delta) = 0.5$  [210]. A plot of  $L_b$  vs.  $1/\Delta$  is shown for the cases  $q = 2, 3$ , and 4 in Fig. 5.11(b) using a semi-logarithmic scale. We find that fits of the simple exponential form

$$L_b \sim \exp(A/\Delta) \quad (5.9)$$

to the data work well, and we arrive at  $A = 3.6 \pm 0.03$  as a  $q$ -independent constant that depends only on the disorder distribution. We note that this scaling is not consistent with that proposed in Ref. [209, 210] for the RFIM, but it is in line with

what is found in numerical simulations of the RFIM in Ref. [211]. The reason for this discrepancy might be the presence of only a rather weak curvature in a plot of the types of Fig. 5.11(b), and one might need to go to rather small  $\Delta$  to see the asymptotic behaviour.

## 5.4 Summary

In this chapter, a carefully tuned set of parallel tempering simulations is used for creating a benchmark set of disorders for which the ground states are known with a very high probability. This allowed measuring the success probabilities of finding ground states for short parallel tempering simulations and for the graph-cut method. It is observed that as a function of system size  $L$  the quality of the states returned by graph-cut and parallel tempering techniques is quite similar for small  $q$  and different system sizes. But the quality of graph-cut results worsens rather quickly as  $q$  increases. The PT simulations are computationally much more expensive than the corresponding GC runs for small  $L$  and different values of  $q$ . The code used for PT simulations is a highly efficient GPU implementation but still fails to top the GC performance. For larger system sizes there is a crossover and the graph-cut approach starts to outperform even the GPU implementation of PT and is likely asymptotically the most efficient approach. The success probability for the very fast graph-cut method can be additionally increased by using repeated runs and selecting the minimum-energy state found between them.

The main outcomes of this  $d = 2$  study are as follows:

- The parallel tempering method guarantees ground states in the infinite run-time limit, but the graph cut method gives approximate ground states in a very short time  $\sim \mathcal{O}(N)$ , irrespective of the number of states  $q$ .
- The graph cuts provide an excellent approximation to the ground states for  $q = 3, 4$ . The overlap between the ground state and the final states obtained from the graph cut is very high for smaller  $q$  (e.g.,  $\gtrsim 96\%$  for  $q = 3$ ) and decreases as  $q$  is increased.
- For a fixed value of  $q = 3$ , the overlap between ground states and graph-cut configuration saturates to a very high value of about 91% for  $L \gtrsim 40$ .

The above conclusions illustrate that the graph cut method is suitable for the study of a two dimensional ( $d = 2$ ) RFPM for lower  $q$ -values with large system sizes. In particular, for  $q = 3$ , and 4, the lowest states found by the graph cut method are very close to the ground states. The  $q$ -state RFPM has not received very much attention due to the unavailability of efficient computational techniques. Although,

it has great physical significance. This study sets the stage for investigating random-field Potts model and similar disordered spin models in general, using the methods based on graph cuts.



# Chapter 6

## Spin glass with variable frustration

The basic concepts relevant for studying the phase transition in spin glasses are introduced in Chap. 2.2.3. However, the discussion there was restricted to stochastic frustration. In this chapter, we investigate the effect of changing the frustration of SG samples while keeping the fraction of anti-ferromagnetic bonds constant. The results are compared to the corresponding systems with stochastic frustration with a focus on the spin-glass phase transition.

This chapter is organised as follows. In Sec. 6.1, we introduce the concept of under-frustrated spin glass systems. The numerical method used for generating such under-frustrated system from a given stochastic system is also described. In Secs. 6.2-6.3, the physical quantities and concepts like equilibration are discussed. In Sec. 6.4 and 6.5 the results related to the scaling and phase transition are discussed for a system with Gaussian interactions and bimodal interactions, respectively. A summary of the chapter is presented in Sec. 6.6.

### 6.1 Under and over-frustrated spin glass

In the present chapter, we study the phase transitions and criticality in under-frustrated spin-glass systems. However, before one can study the criticality, it was important to have an algorithm to construct under-frustrated spin glasses. The concept of under-frustrated and over-frustrated spin glasses was described for hierarchical lattices in Ref. [212]. In this work, the same idea was used to generate under-frustrated systems. We apply Kawasaki-like dynamics to exchange the random bonds for changing the frustration at a constant bond probability  $p$ . Once the frustration content was set, and the samples are generated, Monte Carlo simulations are used to study the under-frustrated 2D Edward-Anderson spin glass system. This algorithm can be used to generate over-frustrated or under-frustrated systems as shown in Fig. 6.1. The black boxes and the green boxes represent the

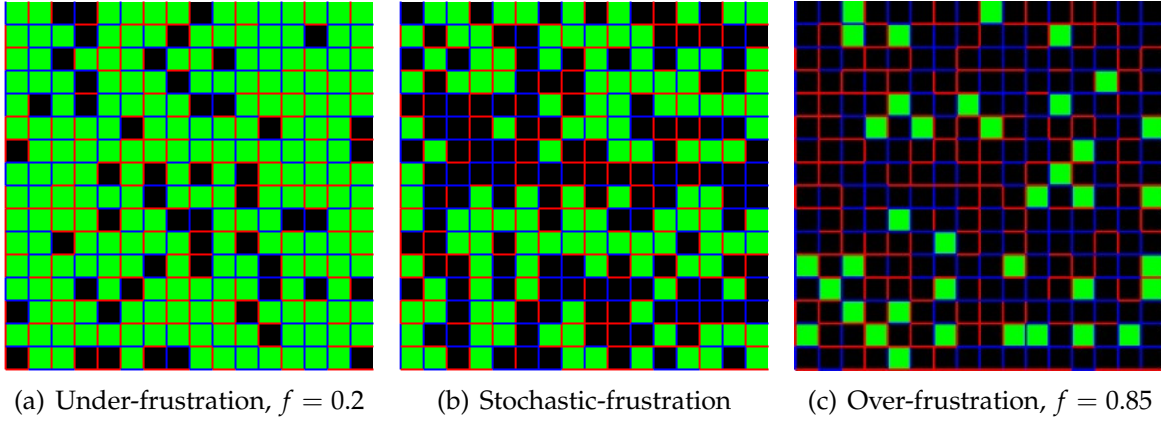


Figure 6.1: In above figures, black boxes and green boxes represent frustrated and non-frustrated plaquettes respectively.

frustrated plaquettes and non-frustrated plaquettes respectively. The product of the four bonds defines the frustration  $f_{\text{plaq}}$  of a plaquette i.e the smallest closed loop of the bonds

$$f_{\text{plaq}} = \prod_{i=0}^{k-1} J_{ij}, \quad (6.1)$$

where  $k$  is the number of total bonds forming the loop,  $J_{ij}$  is the bond connecting the sites  $i$  and  $j$  of the plaquette and  $i$  is the index of the bonds going from 0 to  $k - 1$ . A plaquette is frustrated if  $f_{\text{plaq}} < 0$  and not frustrated otherwise. Figs. 6.1(a), 6.1(b) and 6.1(c) show under-frustrated, stochastic-frustrated and over-frustrated systems respectively. We define frustration of a system with periodic boundary conditions as:

$$f = \frac{1}{dL^d} \sum_{i=0}^{dL^d} (f_{\text{plaq}})_i, \quad (6.2)$$

where  $d$  defines the dimensions of a system,  $f_{\text{plaq}} = \pm 1$  and  $i$  is the running index.

The bond concentration is fixed to a value,  $p = 0.5$ . The red edges show a negative valued and the blue edges show a positive valued bond respectively. The Gaussian case is similar to the bimodal case. The sign of the product again determines if a plaquette is frustrated or not.

### Algorithm to achieve a certain frustration

**Step 0** Generate a random disorder with anti-ferromagnetic bond concentration  $p = 0.5$  on a two-dimensional lattice.

**Step 1** Pick two bonds randomly on the lattice. If bonds have the same sign, pick another pair else go to the step 2.

**Step 2** Exchange the two bonds. Each bond affects the frustration of two plaquettes. Check if the frustration was increased or reduced by exchanging the bond. If under-frustration need to be achieved go to Step 3a and for the over-frustrated case go to step 3b.

**Step 3a** For under-frustrated case if after the exchange the frustration of the system was reduced, accept the move.

**Step 3b** For the over-frustration case if after the exchange the frustration of the system was increased, accept the move.

**Step 4** The acceptance criteria is set in a way that the bonds will also be exchanged if the desired frustration was achieved. The algorithm is similar to Kawasaki algorithm.

**Step 5** The simulation was run for a longer period of time even after achieving the required frustration content so that the system was equilibrated and there are no correlations.

This Kawasaki-like approach is a greedy algorithm. Throughout the algorithm the number of negative and positive bonds was conserved, the change only happens in the position of the bonds. However, it does not guarantee that there are no local correlations introduced to the system. Therefore, one would numerically need to test if local correlations are still present after many cycles of the algorithm. This can be tested by measuring the average distance between frustrated plaquettes. If the average distance between frustrated plaquettes stays the same as for the stochastic case that means that these plaquettes do not create clusters on the lattice. If the

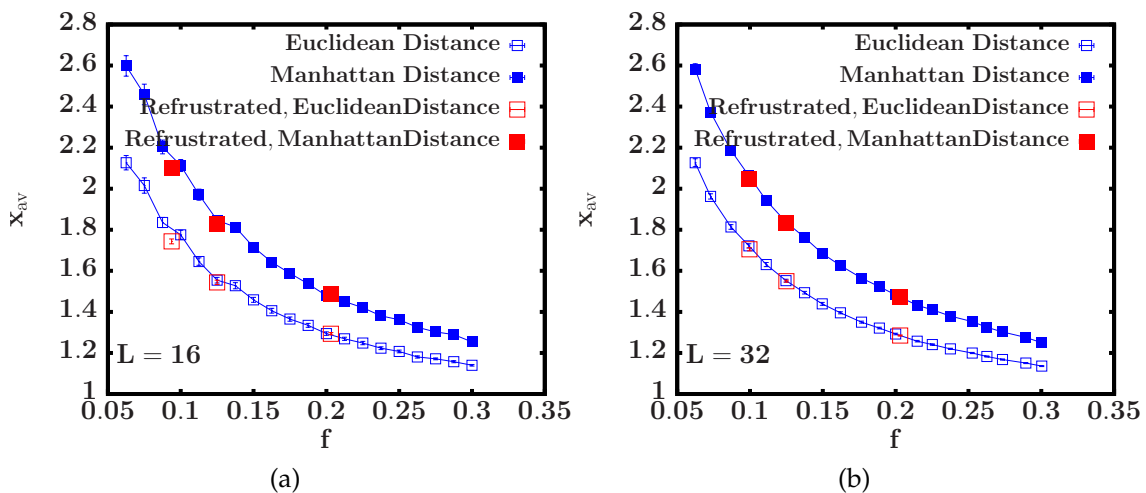


Figure 6.2: Averaged minimum distance to next frustrated plaquette: (a) minimum averaged distance for  $L = 16$  and (b) for  $L = 32$ .

average distance is increased or decreased very much, the clusters of the plaquettes are formed. The two different distances measured here are "Euclidean distance" and "Manhattan distance". These average distances are denoted as  $x_{av}$ .

We see a comparison between the stochastic frustrated system and the under-frustrated system in Fig. 6.2. The plaquettes are mapped onto the coordinates of a lattice and then the distance was calculated between the coordinates. The data represents Manhattan and Euclidean distances for both cases. Fig. 6.2(a) and 6.2(b) show the data for systems with  $L = 16$  and  $L = 32$ , respectively. It can be observed that for both systems sizes the data from under-frustrated and stochastic frustrated systems coincides with-in the error bars for both Manhattan and Euclidean distances. Therefore, we can conclude that the average distance between the plaquettes is same as in case of the stochastic system. Hence, there are no trivial correlations.

## 6.2 Observables

We are interested to understand the criticality and phase transitions in under-frustrated spin glasses. The quantities used to study critical behaviour are well studied for the stochastic spin glasses. Mainly, one was interested in the Binder cumulant, the spin glass susceptibility and the correlation length. To calculate these quantities, one has to calculate the overlap parameter  $q$  and its higher modes like  $q^2$  and  $q^4$ . The **overlap** variable was given by:

$$q = \sum_i s_i^\alpha s_i^\beta, \quad (6.3)$$

where the spins  $s_i^\alpha$  and  $s_i^\beta$  belong to two independent replicas which are simulated simultaneously at the same temperature and have the same disorder realisation  $\{J_{ij}\}$ . The **Binder cumulant**  $g$  for the spin glass was a function of the higher order of overlap parameter

$$g = \frac{1}{2} \left[ 3 - \frac{\langle q^4 \rangle}{\langle q^2 \rangle^2} \right]. \quad (6.4)$$

where the square and the angular brackets indicate the quenched average over disorder and thermal average over disorder, respectively. The wave-vector dependent spin glass susceptibility was defined as:

$$\chi_{SG}(\mathbf{k}) = \frac{1}{N} \sum_{i,j} [\langle s_i s_j \rangle^2] e^{i\mathbf{k} \cdot (\mathbf{R}_i - \mathbf{R}_j)}. \quad (6.5)$$

For  $k = 0$ , one gets the **spin-glass susceptibility**:

$$\chi_{SG}(0) = \frac{1}{N} \sum_{i,j} [\langle s_i s_j \rangle^2], \quad (6.6)$$

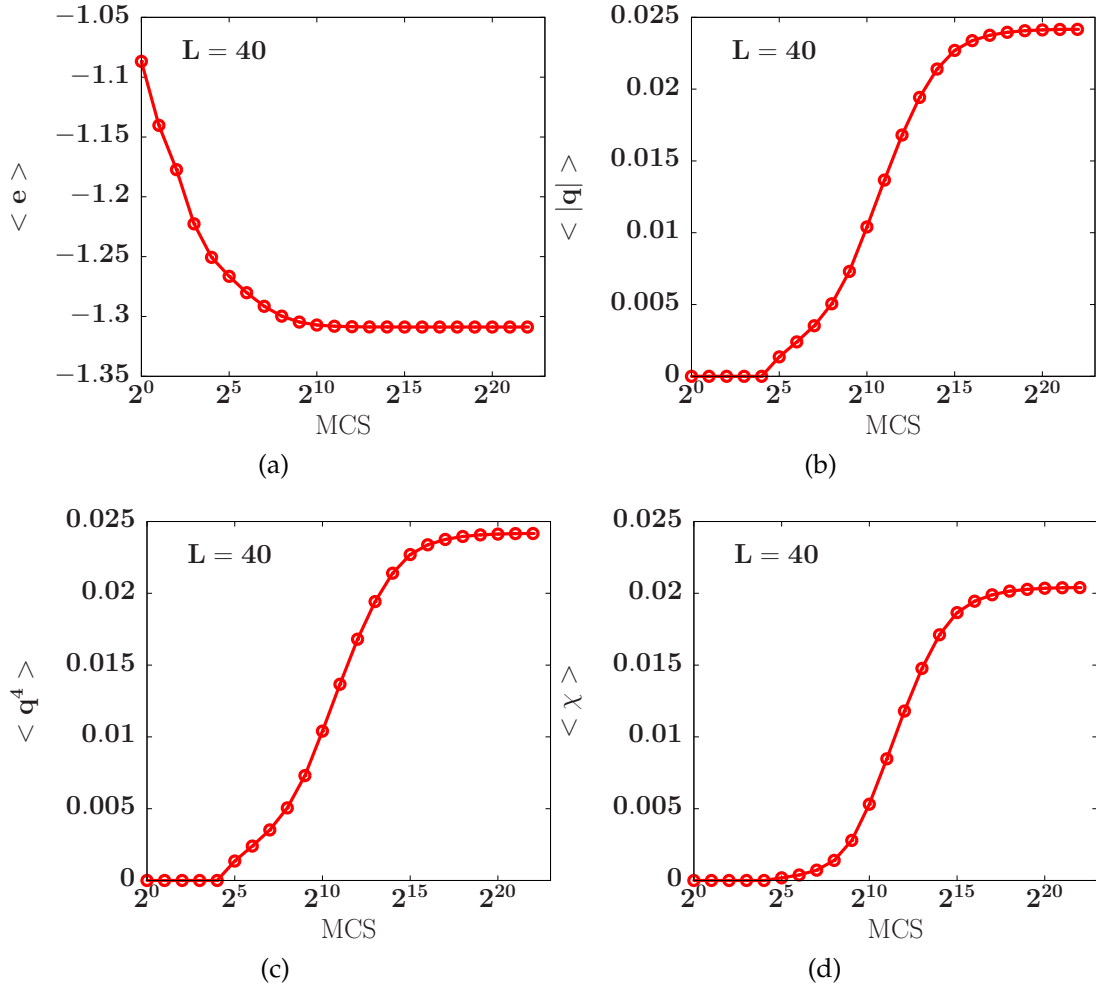


Figure 6.3: Equilibration of the physical quantities in logarithmic bins. The total number of MCS are  $MCS = 2^n$ . In the top figure, one can see that the average energy equilibrates much faster than  $q$  and  $\chi$  in the middle and bottom figures respectively.

and the second moment correlation length was defined as:

$$\tilde{\zeta}_L = \frac{1}{2 \sin(\mathbf{k}_{\min}/2)} \left[ \frac{\chi_{SG}(0)}{\chi_{SG}(\mathbf{k}_{\min})} - 1 \right]^{\frac{1}{2}}, \quad (6.7)$$

where  $\mathbf{k} = (\mathbf{k}_{\min}, 0)$ ,  $\mathbf{k}_{\min} \equiv 2\pi/L$ , and  $\chi_{SG}(k)$  was the Fourier transform of  $\chi_{SG}(x)$ .

### 6.3 Simulation parameters and equilibration

In this section, the results of Monte-Carlo simulations are discussed. MC simulations are performed on the square-lattice for bimodal and Gaussian couplings with periodic boundary conditions. The simulations are done for stochastic and underfrustrated spin glasses with several values of the lattice size  $L$ , with  $8 \leq L \leq 76$ . Length of the system is restricted  $L \leq 55$  for the spin glass with Gaussian coupling. We employ the Metropolis algorithm, parallel tempering and Houdayer cluster algorithm on GPUs as discussed in Chap. 4. For each lattice size we collect data in the range  $T_{\min} \leq T \leq T_{\max}$ . The value of  $T_{\min}$  and  $T_{\max}$  are set as 0.17 and 1.4 respectively. The logarithmic binning was done with base 2 [187]. Every  $n$ th bin has  $(2^n - 2^{n-1})$  values averaged in it. The last bin contains the data for half of the simulation. The average was calculated over  $10^4$  disorder samples for all cases. The length of the simulation was set to be  $2^{24}$  Monte Carlo steps. Every Monte Carlo step consists of  $N_T - 1$  parallel tempering trials (swaps) and  $L^2$  spin flip trials called sweeps. The logarithmic binning was used to ensure the equilibration in the test runs.

In Fig. 6.3 equilibration times for different systems are shown. The lowest temperature takes the longest time to equilibrate. Hence, the plots show the equilibration for the lowest temperatures. Fig. 6.3(a) shows the equilibration of the energy as a function of the number of bins. The MCS in each bin are exactly  $2^n$ , where  $n$  was the bin number here. In Figs. 6.3(b), 6.3(c) and 6.3(d) the equilibration curve for overlap parameter  $q$ , the fourth order of overlap parameter  $q^4$  and the spin-glass susceptibility  $\chi$  are shown.

### 6.4 Under-frustrated spin glass with Gaussian interactions

The standard two-dimensional spin glass with Gaussian couplings does not show a stable spin-glass phase at finite temperatures [213]. At any finite temperature, the paramagnetic phase and only at  $T = 0$  the spin-glass phase may exist. In Chap. 2, the  $\theta$  exponent was introduced in relation to the droplet picture. It was described that the free energy cost of the lowest excitations of linear size  $L$  has  $L^\theta$  dependency. As there was no order at finite temperature, the value of  $\theta$  was negative [214]. It was argued in multiple studies [215] that the same exponent  $\theta$  describes the energy of a somewhat different types of excitations induced by changing periodic boundary conditions to anti-periodic boundary conditions. This excitation can be calculated via domain walls of the droplets. The zero temperature algorithms such as graph-cut can determine the ground state of two-dimensional spin glasses exactly. By employing the periodic and anti-periodic boundary conditions, one can calculate

the defect energy of such system. Hence, it was possible to evaluate  $\theta$  from zero temperature studies. However, for the systems at small but finite temperature the evaluation of  $\theta$  was quite difficult [213]. The extensive Monte-Carlo simulations were required to study behaviour at the small temperatures. The correlation length diverges algebraically as the temperature approaches zero. The critical exponent  $\nu$  of the correlation length depends inversely ( $\nu = 1/\theta$ ) on the droplet exponent  $\theta$ . Many studies were confirming that the value of  $\nu \sim 3.56$  [216].

While the behaviour for the standard spin glass system with stochastic frustration is quite well understood, the under-frustrated system has not been studied on the square lattice yet. In [212], it was argued that there is a spin glass phase transition at the finite temperature for two dimensional systems. If this is true, then the value of  $\theta$  should be positive from defect energy calculation. The value of  $\theta$  is inversely proportional to the exponent  $\nu$ . Any change in this value would change the scaling behaviour of physical quantities which scale with the exponent  $\nu$ . The

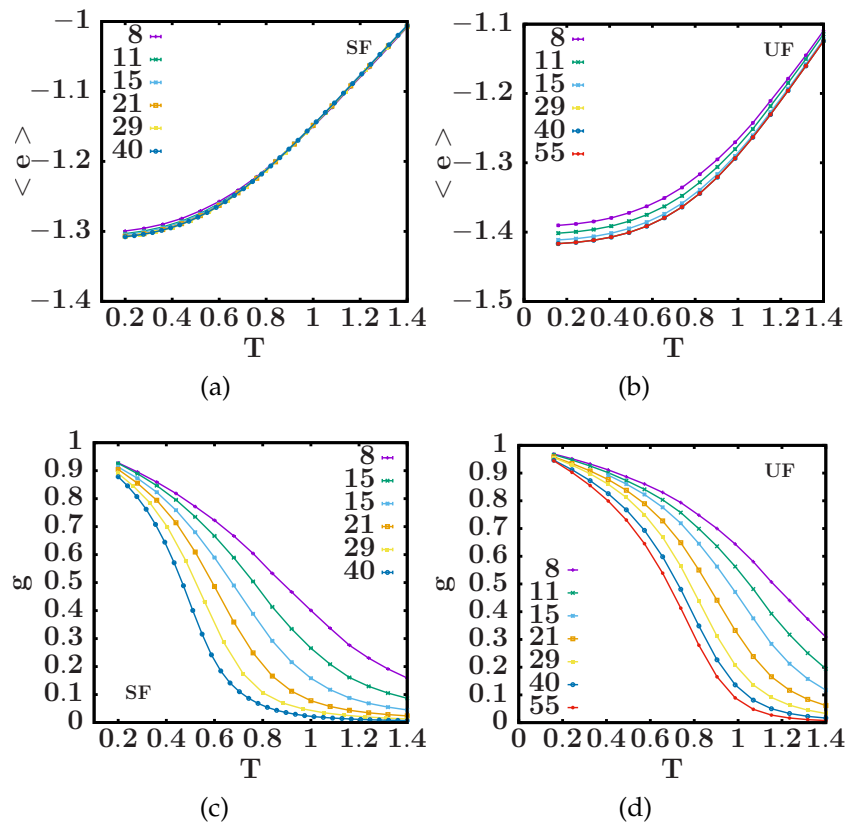


Figure 6.4: The averaged energies and the Binder cumulant as a function of temperature are shown in top and bottom rows respectively. The left column shows the data for stochastic frustrated systems and the right column shows the data for under-frustrated systems.

next section contains a comparative discussion of stochastic and under-frustrated systems.

### 6.4.1 Benchmarking the physical quantities

Few aspects of the stochastic frustrated spin glass were quite well understood. In this section, the results of stochastic frustrated system were compared to the under-frustrated system. In Fig. 6.4, we see the averaged energies and Binder cumulant as a function of temperature. The values of the averaged energies are lower for the under-frustrated case when compared with stochastic case. The Binder cumulant by definition is not large than one. However, there are some differences in Fig. 6.4(c) and 6.4(d).

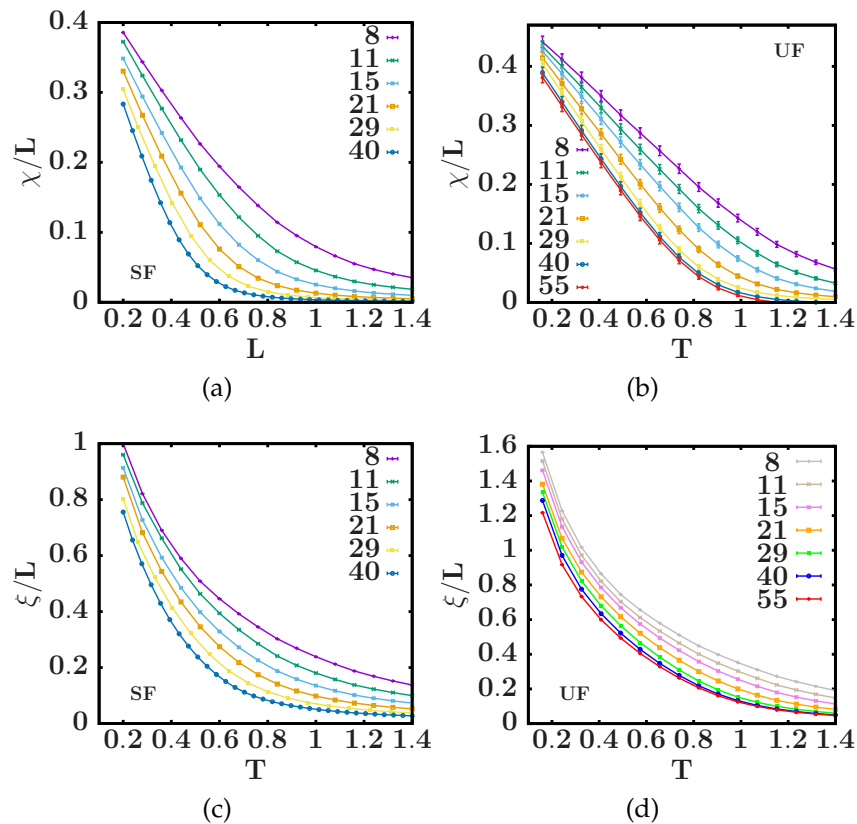


Figure 6.5: In Fig. 6.5(a) and 6.5(b), the spin glass susceptibility is shown for stochastic and underfrustrated systems, respectively. In the lower row, the data for the correlation length is plotted in Figs. 6.5(c) and 6.5(d)

Similarly, we show spin-glass susceptibility and correlation length for stochastic and under-frustrated systems in Fig. 6.5. In the left column results from [195] and from new runs for stochastic frustrated system are shown and in the right column under-frustrated are shown.

## 6.4.2 Phase transition and scaling

One primary aim of this chapter is to investigate if under-frustrated systems might show a phase transition at finite temperatures. If a spin glass phase exists, the average absolute defect energy should increase. There were no such studies performed for the under-frustrated systems. However, a mobile bond model has been studied in [217] and it is shown that there is no spin glass phase for this model. The model discussed here is related to the mobile bond disorder, but with more control over the frustration of the system.

### 6.4.2.1 Defect energy

In Fig. 6.6 defect energies for different frustrations were shown as a function of system size  $L$ . The frustration is varied between 0.0625 and 0.75. It is visible from the plot that the frustration plays no role in the qualitative behaviour and the defect energies decrease with the increasing system size. The data for stochastic frustrated system (black data points) and a system with frustration  $f = 0.5$  (blue data points) fall on top of each other. The decrease in the defect energies with increasing system size have the negative slope i.e.  $\theta < 0$ . Hence, no spin-glass phase ordering is taking place. The results here support arguments of Ref. [217] and were in contradiction with Ref. [212]. However, a more detailed scaling analysis is required to confirm this result.

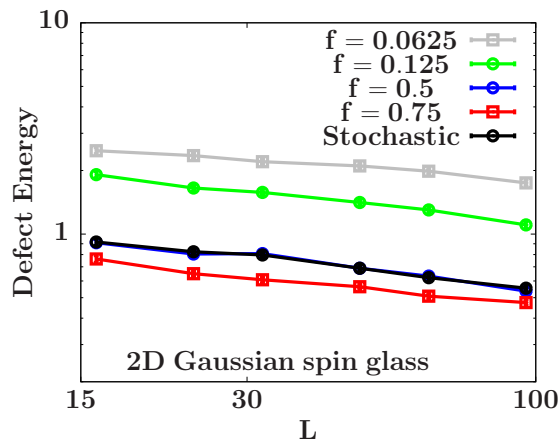


Figure 6.6: The defect energy from zero temperature study for spin glass with Gaussian interactions.

### 6.4.2.2 Finite size scaling (FSS) analysis

We discuss the universality of under-frustrated spin glass with Gaussian interactions in two-dimensions following the same methodology as in Ref. [218]. We com-

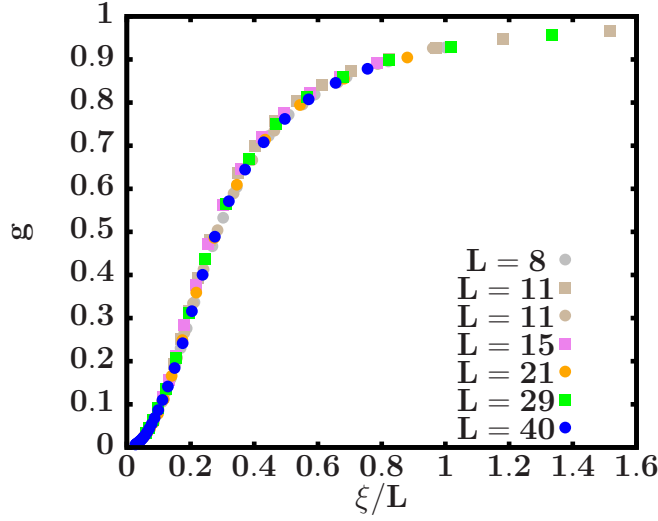


Figure 6.7: The Binder cumulant  $g$  vs correlation length  $\xi/L$ . The data is for 2d spin glass with Gaussian interactions. The circles represent the stochastic frustrated systems, and the squares represent under-frustrated systems.

pare the simulations results of the stochastic and under-frustrated systems. If both models have the same universal behaviour, then they must have the same scaling exponents.

**Universality** To study universality, first the scaling of correlation length and Binder cumulant is discussed here. The correlation length  $\xi$  diverges as it approaches the transition temperature  $T_c$  as

$$\xi \sim (T - T_c)^{-\nu}. \quad (6.8)$$

The Binder cumulant  $g$  allows us to locate the critical point. In finite size scaling, we can write it as a function of the correlation length,

$$g \sim \tilde{g}(L/\xi) = \tilde{g}(L(T - T_c)^\nu). \quad (6.9)$$

Therefore, both  $\xi/L$  and  $g$  are  $L$  independent at critical point. The plots of  $\xi/L$  vs.  $g$  are qualitatively independent of the system size, hence show universal behaviour. In Fig. 6.7, the data for under-frustrated and stochastic frustrated systems is shown. The data for both systems (stochastic and under-frustrated) shows an excellent collapse. The circles represent the under-frustrated systems and the square stochastic frustrated systems. The data represented via squares is for the stochastic systems and the data represented via circles is for the under-frustrated case. There were some deviations for the small system sizes, but the collapse gets better as the system size increases. It is obvious from the figure that both cases fall on top of each other. Hence, they belong to the same universality class. This speaks in favour of no phase transition in 2d spin glass with Gaussian interactions and supports the outcome from defect energies in the last section.

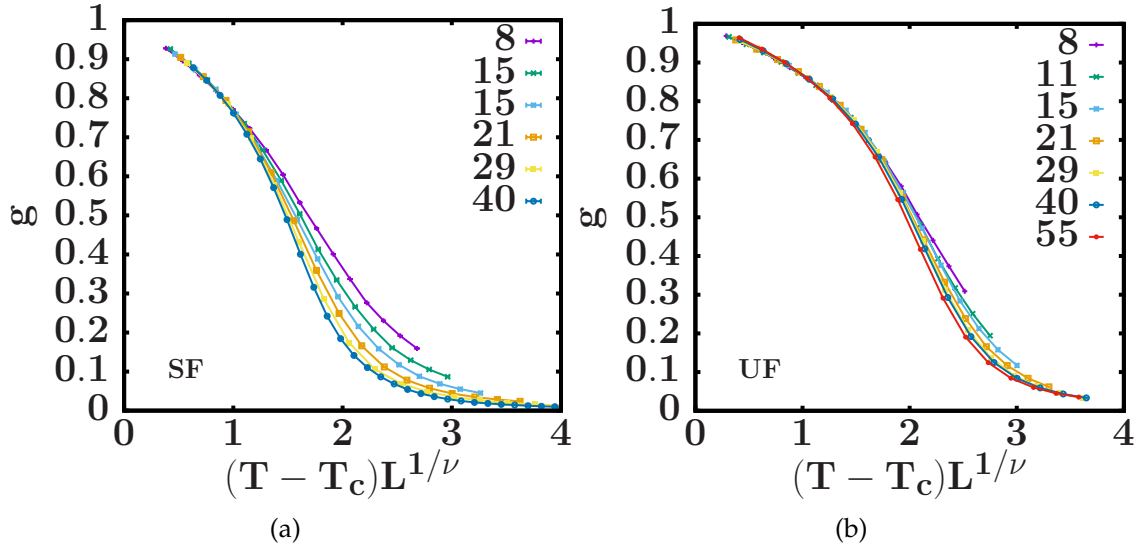


Figure 6.8: Scaling of the Binder cumulant. The fit is forced in the lower temperature regime closer to the critical point. Figs. 6.8(a) and 6.8(b) show the data for stochastic and under-frustrated systems respectively.

As discussed earlier, the value of  $\nu$  is well established for the system with frustration. Using the scaling ansatz for the Binder cumulant, the value of  $\nu$  is evaluated for both under-frustrated and stochastic frustrated spin glass systems. There is no value of  $\nu$  which allows a perfect fit for the whole range of the temperatures. This is due to the fact that the scaling relation 6.9 is only valid close to the critical point. Therefore, one has to choose the fitting range carefully. In our case we considered the range where value of the Binder cumulant is larger than 0.5 restricting ourselves to the lower values of the temperature. We use the method described in Ref. [219] to perform an automatic finite-size scaling analysis for a given set of simulated data. A scaling ansatz to optimize an initial set of scaling parameters that enforce the data to collapse is given by,

$$y(T, L) \sim f[(T - T_c)L^a]L^b. \quad (6.10)$$

In Eq. (6.10),  $y(T, L)$  is interpreted as the observables from the simulations. The exponents  $a$  and  $b$  are interpreted as  $1/\nu$  and  $2 - \eta$  respectively. Choosing a range as described above and using this ansatz, we get the following values for  $\nu$  and  $T_c$ . According to Eq. (6.10), data curves of  $y(T, L)$  for different values of  $T$  and  $L$  collapse on each other if  $y(T, L)L^{1/\nu}$  is plotted against the scaled variable  $u = (T - T_c)L^{1/\nu}$  and if the free parameters  $a$  and  $b$  of the scaling assumption were chosen properly. The quantity  $u$  is the first term of polynomial expansion of the scaling function  $f[u]$  up to lowest order in  $u$ . In the critical regime where  $u \ll 1$  this assumption holds. In Fig. 6.8, it is evident that the collapse at the left corners of both plots shows a better collapse compared to the right corner. In Fig. 6.8(a)

Quantity	Value	Error	$p$ -value
Stochastic, $\nu$	3.26	0.34	0.71
Stochastic, $T_c$	0.004	0.005	0.67
Under-frustrated, $\nu$	3.52	0.21	0.76
Under-frustrated, $T_c$	0.005	0.006	0.82

Table 6.1: Values of parameters from the collapse of the data for the Binder cumulant.

and Fig. 6.8(b) the fits for under-frustrated and stochastic frustrated systems were shown, respectively. We expect better collapse for the larger system sizes due to finite-size effects for smaller system sizes, however also the small system sizes do not deviate very much. We list the parameters determined via collapse method in Table 6.1. The collapse seem to be reasonably good as the  $p$ -value is always larger than 0.5. For both systems the phase transition happens at zero temperature as the value of  $T_c$  is zero within errorbars. The system with reduced frustration does not show a finite size phase transition as claimed in Ref. [212].

Similar to the Binder cumulant, the correlation length can be used to evaluate the value of  $\nu$ . The ansatz described in Eq. (6.10) is used again for the data collapse. The range of the fit is once again limited to the smaller temperature values, where the value of  $\xi/L$  is large. In Fig. 6.9(a), the data for the under-frustrated system is shown. The data for the stochastic frustrated system is shown in Fig. 6.9(a). The values of  $\nu$  evaluated from both systems match to the known value of the  $\nu$  in the literature (Table 6.2). It is evident from the parameters that the finite temperature phase transition does not exist for the under-frustrated case.

Quantity	Value	Error	p-value
Stochastic, $\nu$	3.41	0.18	0.61
Stochastic, $T_c$	0.0009	0.0034	0.81
Under-frustrated, $\nu$	3.48	0.13	0.69
Under-frustrated, $T_c$	0.001	0.002	0.92

Table 6.2: Collapse parameters for the correlation length.

The spin glass susceptibility  $\chi$  is another important quantity of interest. The spin glass system with Gaussian interactions has a unique ground state. The susceptibility has the following finite size behaviour at low temperatures

$$\chi \sim L^{2-\eta} \tilde{\chi}(L/\xi). \quad (6.11)$$

The value of  $\tilde{\chi}(L/\xi)$  approaches a constant value as  $T \rightarrow 0$ . Closer to the critical

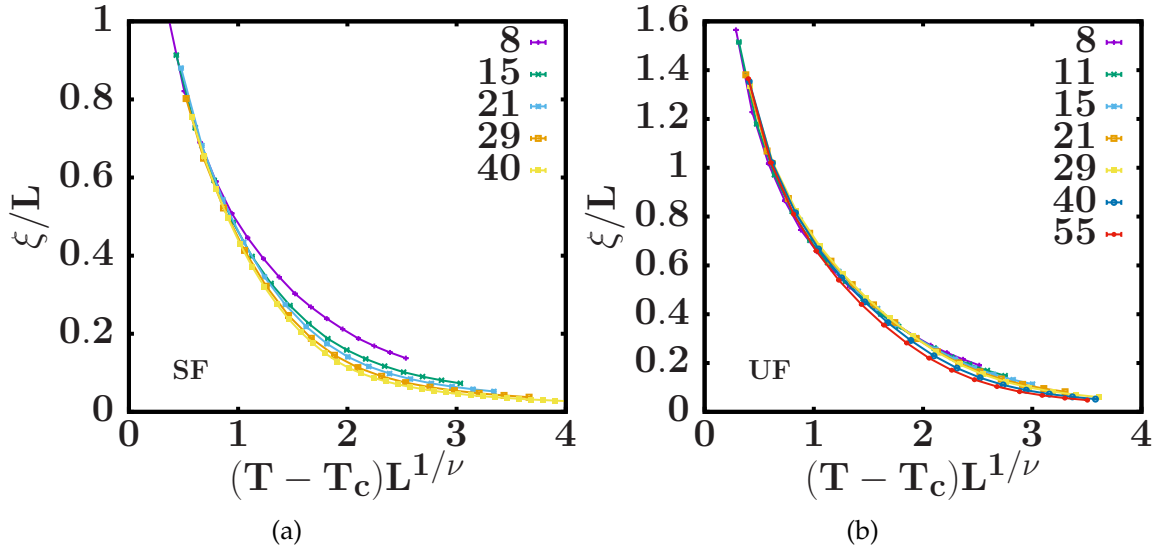


Figure 6.9: Scaling of the correlation length. The fit is forced in the lower temperature regime closer to the critical point. Figs. 6.8(a) and 6.8(b) show the data for stochastic and under-frustrated systems respectively.

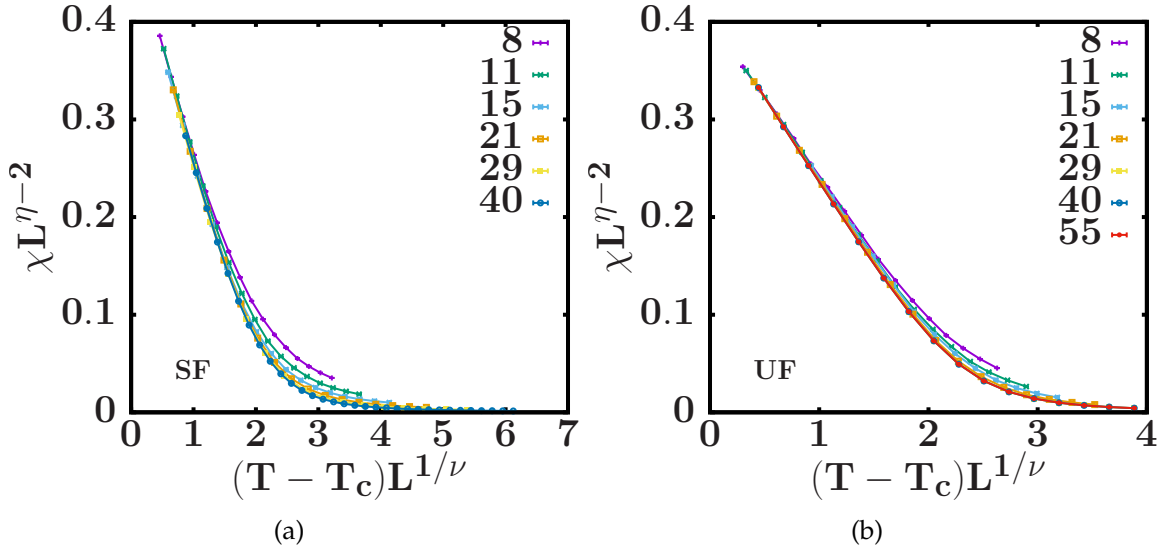


Figure 6.10: Scaling of the spin glass susceptibility. The fit is forced in the lower temperature regime closer to the critical point. Figs. 6.8(a) and 6.8(b) show the data for stochastic and under-frustrated systems respectively.

region but at finite temperatures, where the correlation length is small compared to the system size, there should be no system size dependence of the susceptibility  $\chi$ .

In Figs. 6.10(a) and 6.10(b) for both under-frustrated and stochastic frustrated

cases, the fit form is the same as expected from Eq. (6.11). If the range of collapse is restricted to the smaller temperatures, the fit within error bars give the same value for  $\nu$  as Binder cumulant or the correlation length. The only difference is the y-axis where the value of  $L^{\eta-2}\chi$  is used. The fit values were shown in Table 6.3

Quantity	Value	Error	$p$ -value
Stochastic, $\nu$	3.42	0.19	0.59
Stochastic, $T_c$	0.002	0.003	0.58
Under-frustrated, $\nu$	3.55	0.12	0.56
Under-frustrated, $T_c$	0.0007	0.004	0.61

Table 6.3: Collapse parameters for the spin glass susceptibility.

It is clear from the FSS that there is no hint of any phase transition for under-frustrated spin glass with Gaussian interactions. The value of  $\nu$  matches the standard value from the stochastic frustrated case, and both systems belong to the same universality class. The quality of the fits is always good at the lower temperatures as the  $p$  value is always larger than 0.5. In the next section, we discuss behaviour of the under-frustrated spin glass with bimodal interactions.

## 6.5 Under-frustrated spin glass with bimodal couplings

There are studies such as Ref. [213] showing that the stochastic frustrated two-dimensional spin glass with bimodal couplings does not show a stable spin-glass phase at finite temperatures. As in the case of spin glass with Gaussian interactions, at any finite temperature, such systems were in the paramagnetic phase and only at  $T = 0$  the spin-glass phase may exist. In the literature, there is an ongoing debate if the spin glass with both Gaussian and bimodal interactions belong to the same universality class [220, 216]. While there is evidence for this scenario e.g. Ref. [221], a very recent study in Ref. [222] show that different kinds of discrete models do not belong to the same universality class. Therefore, the question of universality is a very hot topic of research for the spin glass models with discrete interactions. For the Gaussian case, the droplet theory is used to describe the low-temperature behaviour, but the use of this theory is not straightforward in discrete models. Because of the gap between the ground state and first excited state, there is a freezing regime in where the studied quantities freeze and do not show the expected behaviour as  $T \rightarrow 0$ . This behaviour is a consequence that the system does not escape from the ultra-deep minima of the hierarchically disordered energy landscape. Therefore, one needs to understand the freezing regime and its relations to the FSS.

The defect energies analysis of the Gaussian case showed that there is no spin glass phase at a finite temperature. The same analogy is used here for the bimodal case. Under-frustrated spin glass systems with bimodal interactions have not been studied on Euclidean lattices using Monte-Carlo simulations yet. In [212], it is argued that there is a spin glass phase transition at the finite temperature for two dimensional systems. If this is true, then the value of  $\theta$  should be positive from defect energy calculations, and we should get a different scaling behaviour from the correlation length. In the next sections, we discuss the universality and scaling for the under-frustrated two-dimensional spin glass with bimodal interactions.

### 6.5.1 Benchmarking the physical quantities

To test the correctness of our code, the results for the stochastic frustrated system were compared to the data of Ref. [195]. These results were shown in the left column of Fig. 6.11 and Fig. 6.12. The correctness of the code is established here. The

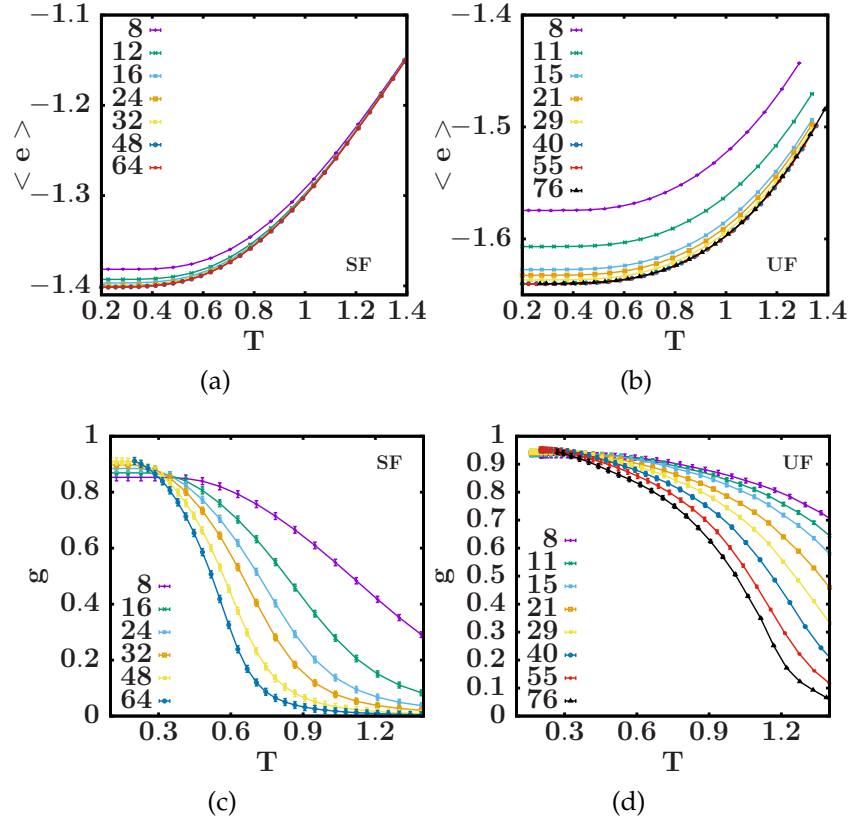


Figure 6.11: Same as Fig. 6.4 but for two dimensional spin-glass with bimodal interactions. The data from own simulations is shows as points and the literature data is plotted as lines.

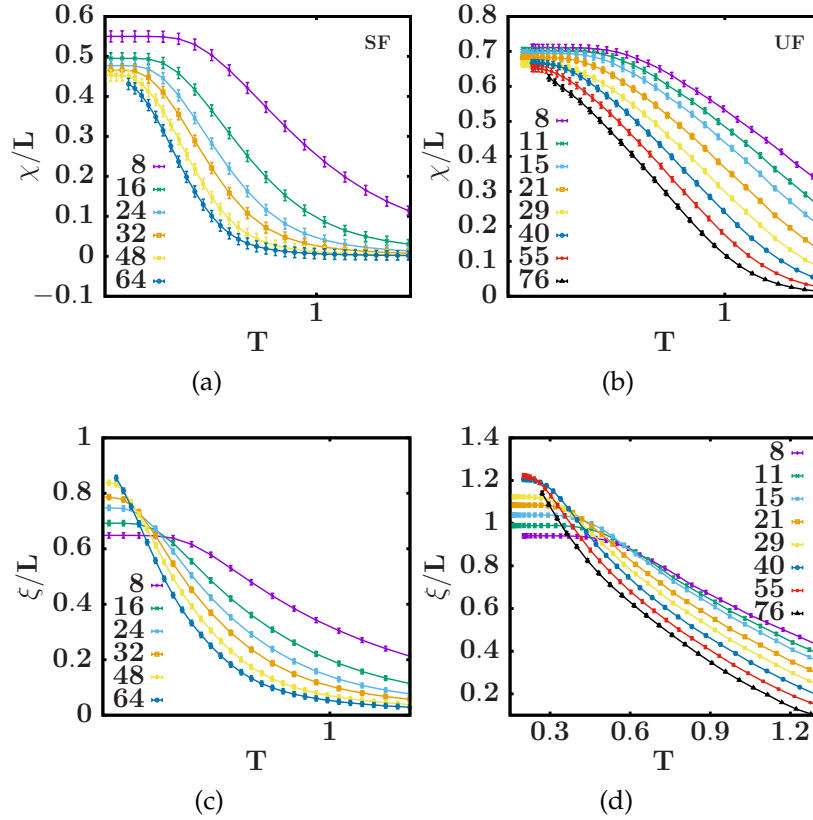


Figure 6.12: Same as Fig. 6.5 but for two dimensional spin-glass with bimodal interactions.

data from our own runs and Ref. [195] coincided within errorbars. In the right column of Fig. 6.11 and 6.12, the data for the under-frustrated system is shown. There were clear differences which can be seen between both models. In Figs. 6.11(a) and 6.11(b) the average energies for stochastic and under-frustrated systems were shown respectively. The energies for under-frustrated system were lower compared to the stochastic simulations. By lowering the frustration, the system moves in the direction of the ferromagnetic system. The zero frustration model corresponds to a ferromagnet and the energy is lower. This effect can be seen in all the quantities like spin glass susceptibility, Binder cumulant and correlation length shown in Fig. 6.11 and 6.12. The figures in the left column and right column can be clearly distinguished. The average energies decreases and the correlation length increases by lowering the frustration.

These differences were studied in detail in the next sections of this chapter when the FSS is discussed.

## 6.5.2 Phase transition and scaling

In this section, we investigate the spin-glass model with bimodal interactions with a focus on a possible phase transition. As for the Gaussian case, first of all, the defect energy of the bimodal spin glass is studied. In Ref. [217] Hartmann concluded that for the mobile bond model there seem to be no spin glass phase, however the study was not performed at finite temperatures. Using the same analogy, the defect energy is used as a parameter for zero temperature studies to establish if spin-glass phase exists for the under-frustrated spin glass model with bimodal interaction.

### 6.5.2.1 Defect energy

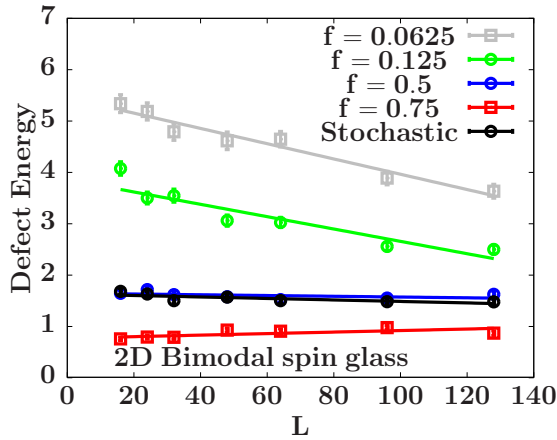


Figure 6.13: The defect energy from zero temperature study for spin-glass with bimodal interactions.

In Fig. 6.13, defect energies for different frustrations were shown as a function of system size  $L$ . The frustration is varied between 0.0625 and 0.875. The standard case of stochastic frustration is marked as unrestricted. We see that in the plot there are quantitative differences between different frustrations, however qualitatively all seem to settle down to a different constant value for the larger system sizes. The slope with increasing system size is zero. However, picture is not very clear for the smaller frustrations. Hence, for bimodal case, just from looking at the slope of the defect energies, it is not possible to predict the absence or presence of a spin glass phase. In contrast to the Gaussian system, the bimodal case has a very high degeneracy in the ground states and a large discrete spectrum (many metastable energy states). The large energy spectrum causes the freezing. Therefore, in the next section, the freezing regime and its properties were investigated. The relation to the scaling ansatz and the phase transition is established.

### 6.5.2.2 The freezing temperature

The freezing regime occurs for temperatures close to zero in any finite spin glass system with discrete interactions. Indeed, it is argued that there exist two different behaviours, which depend on how large the system size  $L$  is compared to a temperature dependent crossover length  $L_c$  [220, 216]. There were two ways to understand the freezing regime.

In the first argument, one considers the states corresponding to the two lowest energy values for a given system size  $L$ . The energy gap can be defined as

$$\Delta = E_1 - E_0 = 4. \quad (6.12)$$

The degeneracies of these energies were given by  $N_0(L)$  and  $N_1(L)$ , respectively. It is shown in [216] that  $\ln N_1/N_0 \approx 4 \ln L$ . Close to zero temperature only the states with the lowest energy contribute to the thermodynamics. This occurs when  $N_0(L) \gg N_1(L)e^{-\Delta/T}$ , i.e., for

$$T \ll \frac{\Delta}{\ln(N_1(L)/N_0(L))} \sim \frac{1}{\ln L}. \quad (6.13)$$

In the freezing regime, the observed behaviour is independent of  $T$  as the system is frozen in the ground state. However, when  $N_0(L) \ll N_1(L)e^{-\Delta/T}$ , the presence of the gap has a negligible effect, and the system is expected to have the same behaviour as models with continuous distributions. The crossover from the freezing regime to the other regime occurs at a  $L$ -dependent freezing temperature  $T_f(L)$  which according to Eq. (6.13) scales as  $1/\ln L$ . The natural definition of  $T_f(L)$  would be by requiring  $N_0(L) = N_1(L)e^{-\Delta/T_f}$ , but the implementation of this definition is difficult. In practice,  $T_f(L)$  can be estimated by identifying the value of the temperature  $T$  at which the temperature independent behaviour of the physical quantities sets in.

The freezing regime is a finite size effect, therefore multiple definitions for the freezing temperature may exist. In renormalisation group theory, these two regimes can be interpreted due to two different fixed points. One belongs to the infinite volume behaviour like for the case of Gaussian couplings, and another belongs to the low-temperature behaviour  $T < T_f(L)$ . In some studies [223, 224, 225], the droplet theory has been used to suggest that the power law behaviour of the freezing temperature

$$T_f(L) \sim T^{-1/\theta_s}, T_f(L) \sim L^{-\theta_s}. \quad (6.14)$$

The value of  $\theta_s$  has been predicted as 0.5 in Ref. [223] and simulated as 0.37 in Ref. [225, 216]. Due to the limited range of accessible system sizes, there were no conclusive studies which could discriminate between logarithmic and power law behaviour for  $T_f$ . Therefore, we consider also both approaches for the analysis for the comparative studies.

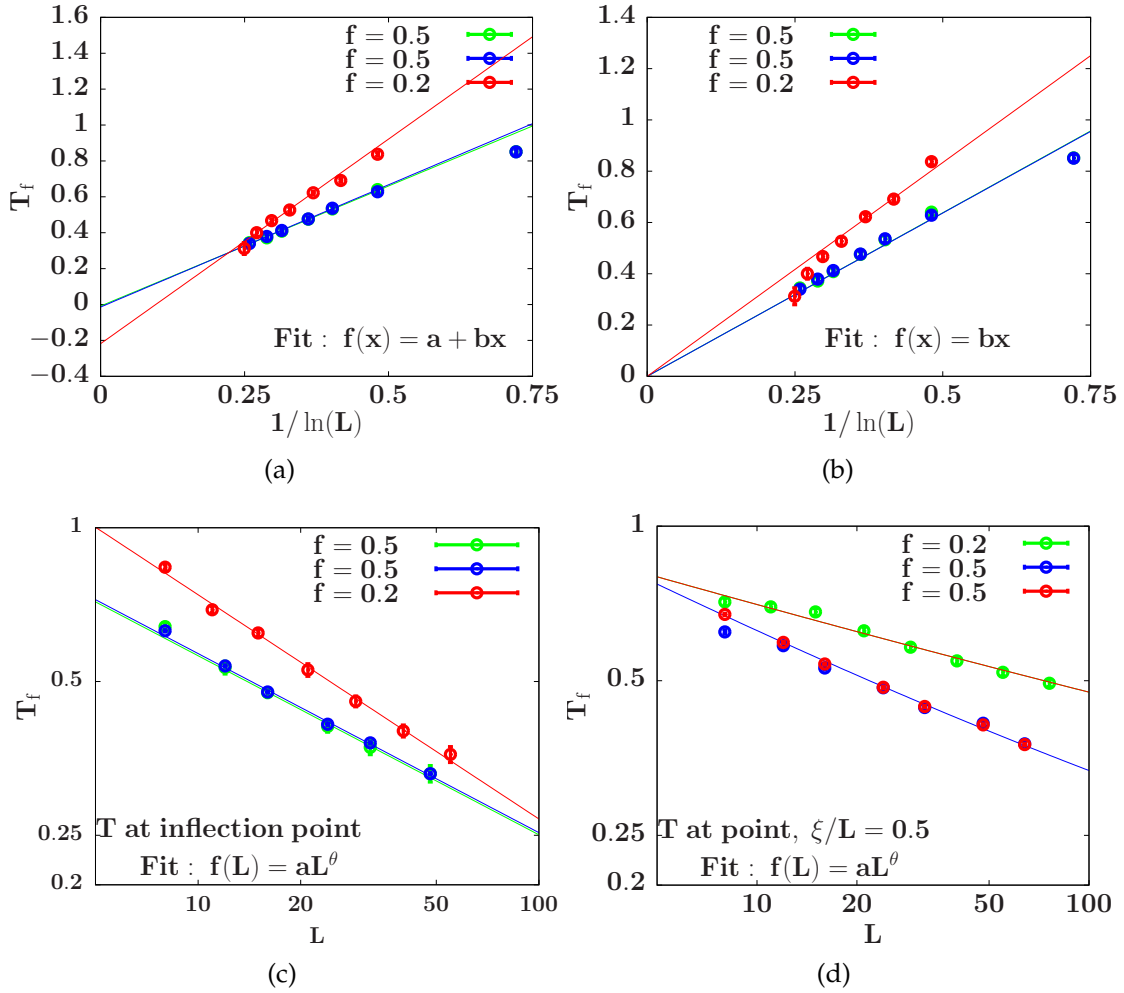


Figure 6.14: Freezing temperature  $T_f(L)$  as estimated from the inflection point of the correlation length.

In Fig. 6.14(a) an extrapolation to  $L \rightarrow \infty$  of the freezing temperature  $T_f$  is shown assuming the logarithmic form of Eq. (6.13) i.e. the x-axis shows  $1/\ln(L)$  and the y-axis shows the value of temperature at the inflection point of the correlation length  $\zeta$ . The inflection point shifts approaches zero in thermodynamic limit. The same is true also for the freezing regime. The data is fitted using a linear ansatz  $T_f(L) = T_f(0) + b/\ln(L)$ . The different values of the fit variables were listed in table 6.4.

The results of fit show that the value for under-frustrated case is much lower compared to the value of stochastic frustrated system. It is clear that either the system sizes were too small to predict something for the under-frustrated system or the logarithmic scaling of  $T_f$  is not observed. If we force our data to fit to zero for  $L \rightarrow \infty$  as shown in Fig. 6.14(b). The fit parameters were listed in the Table 6.5.

System	$T_f(0)$	$\pm\delta T_f(0)$	$b$	$\pm\delta b$	$p$ -value
Stochastic	-0.03307	0.007705	1.41593	0.02342	0.9927
Stochastic F.	-0.0364055	0.003411	1.41624	0.03421	0.8534
Under-frustrated	-0.199939	0.01221	2.22191	0.03906	0.5629

Table 6.4: Fit variables for the freezing temperature using the logarithmic ansatz.

System	$T_f(0)$	$\pm\delta T_f(0)$	$b$	$\pm\delta b$	$p$ -value
Stochastic	0	0	1.27577	0.02644	$5.10481e - 06$
Stochastic F.	0	0	1.27359	0.02582	$1.03844e - 05$
Under-frustrated	0	0	1.66749	0.03001	$2.94973e - 06$

Table 6.5: Fit variables for the freezing temperature using the logarithmic ansatz.

We can see that this fit has extremely small  $p$ -values. Hence, the quality of fit is very bad. However, the fit quality in Fig. 6.14(a) is much better than in Fig. 6.14(b).

In Fig. 6.14(c) extrapolation to  $L \rightarrow \infty$  of the freezing temperature  $T_f$  is shown using the power law ansatz. The x-axis shows  $L$  and the y-axis shows the value of temperature at the inflection point of the correlation length  $\xi$ . The data is fitted using a power-law ansatz  $T_f(L) = aL^{\theta_s}$ . The different values of the fit variables were listed in the Table 6.6.

System	$\theta_s$	$\pm\delta\theta_s$	$a$	$\pm\delta a$	$p$ -value
Stochastic	-0.350601	0.01295	1.27151	0.04165	0.92323
Stochastic Fernandez et. al.	-0.350495	0.003411	1.25863	0.04989	0.893461
Under-frustrated	-0.438957	0.01531	2.03146	0.09774	0.72041

Table 6.6: Fit variables for the freezing temperature using the power ansatz  $T_f(L) = aL^{\theta_s}$  from the temperatures at inflection point.

In Fig. 6.6 extrapolation to  $L \rightarrow \infty$  of the freezing temperature  $T_f$  is shown using the power law ansatz. The x-axis shows  $L$  and the y-axis shows the value of temperature at a point where the value of correlation length  $\xi/L = 0.5$ . For the under-frustrated case the temperatures were taken from the point where the value of  $\xi/L = 0.8$ . These values should be chosen at the middle temperature before the values get saturated at very low temperatures or at very high temperatures. This regime shifts with the frustrations towards lower temperatures. The values of  $\xi/L$  were larger for the under-frustrated system. The data is fitted using a power-law ansatz  $T_f(L) = aL^{\theta_s}$ . The different values of the fit variables at inflection point and at a point where  $\xi/L = 0.5$  were listed in table 6.6 and 6.7, respectively. In both

cases for  $L \rightarrow \infty$ ,  $T_f$  approaches zero. However, the  $p$ -values imply that the quality of the fit in Fig. 6.14(c) is much better than the quality of the fit in Fig. 6.14(d).

System $\theta_s$	$\pm\delta\theta_s$	$a$	$\pm\delta a$	$p$ -value	
Stochastic	-0.3501269	0.01295	1.18139	0.02481	$-2.69315e - 05$
Stochastic Fernandez et. al.	-0.340495	0.0118	1.01092	0.04989	0.00294872
Under-frustrated	-0.206769	0.01378	0.971973	0.04106	0.000205

Table 6.7: Fit variables for the freezing temperature using the power ansatz  $T_f(L) = aL^{\theta_s}$  from the temperatures at a point where the value of  $\xi/L$  is 0.5 for the stochastic system and 0.8 for the under-frustrated system

The values of  $\theta_s$  for the stochastic case were consistent with [216] but, the value of  $\theta_s$  for the under-frustrated case is different. However, all values were higher than the value of  $\theta = -1/\nu = 0.28$ .

### 6.5.2.3 Finite size scaling (FSS) analysis

The presence of freezing for  $T < T_f(L)$  in the spin glass with discrete interactions makes the study of the  $T = 0$  critical behaviour quite difficult. The only way to study the glassy critical behaviour in Ising glass models with a discrete distribution is to approach  $T = 0$  while keeping  $T \gg T_f(L)$  for each system size. This makes the standard FSS analysis impossible. Indeed, in the FSS limit a RG invariant quantity  $R$  should scale as

$$R = f_R(TL^{1/\nu}). \quad (6.15)$$

Under the assumption 6.13 the condition  $T \gg T_f(L)$  implies that this scaling behaviour can be only observed for

$$TL^{1/\nu} \gg T_f(L)L^{1/\nu} \sim \frac{L^{1/\nu}}{\ln L}. \quad (6.16)$$

For  $L \rightarrow \infty$ , the ratio  $L^{1/\nu} / \ln L$  diverges. Therefore, the range of values of  $TL^{1/\nu}$  which were accessible smaller and smaller as  $L$  increases [220, 216]. This implies that the standard FSS limit,  $T \rightarrow 0$ ,  $L \rightarrow \infty$  at fixed  $TL^{1/\nu}$  does not exist. However, as we shall now discuss, one can still study FSS if one uses the ratio  $\xi/L$  as basic FSS variable, i.e., if one considers the scaling form using the RG invariant quantity

$$R = g_R(\xi/L). \quad (6.17)$$

Usually, expressions (6.15) and (6.17) were equivalent. This is not the case here: only the FSS scaling form (6.17) holds in the presence of freezing.

If one assumes that the power law ansatz is the correct one, then the FSS is not governed by 6.17. In that case, again FSS is restricted to only one of the two domains, i.e. in the region where  $TL^\nu \lesssim T_c(L)L^{1/\nu}$  holds has no FSS. This region shrinks as  $L^{(1/\nu-\theta_s)}$  with increasing system size and approaches Gaussian behaviour in the thermodynamic limit ( $L \rightarrow \infty$ ). Therefore, FSS will only hold at intermediate temperatures in bimodal case.

**Universality** For the spin glass with Gaussian interactions, it is established in previous section that under-frustrated and stochastic frustrated systems belong to the same universality class. Here, the same analysis is performed for the bimodal case as for the system with Gaussian interactions. In Fig. 6.15, the data for under-frustrated and stochastic frustrated systems for bimodal system is shown. The data shows an excellent collapse. The data represented via squares is for the stochastic systems and the data represented via circles is for the under-frustrated case. It is obvious from the figure that both cases fall on top of each other. Hence, they belong to the same universality class. This is a hint in favour of no phase transition in 2d spin glass with bimodal interactions. Note that no statement could be made for the bimodal case from the defect energies. We next consider the scaling plots for the observables. Theoretically, the ansatz given by Eq. (6.10) can be used for the scaling plots, However, in contrast to the Gaussian case, the bimodal case has

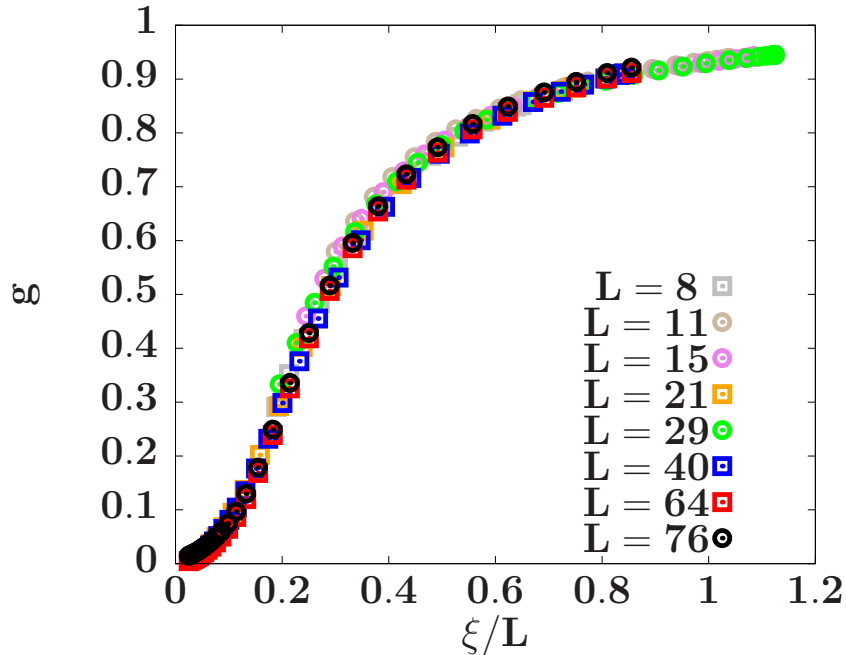


Figure 6.15: The Binder cumulant  $g$  vs correlation length  $\xi/L$ . The data is for 2d spin glass with bimodal interactions. The circles represent the under-frustrated systems, and the squares represent stochastic frustrated systems.

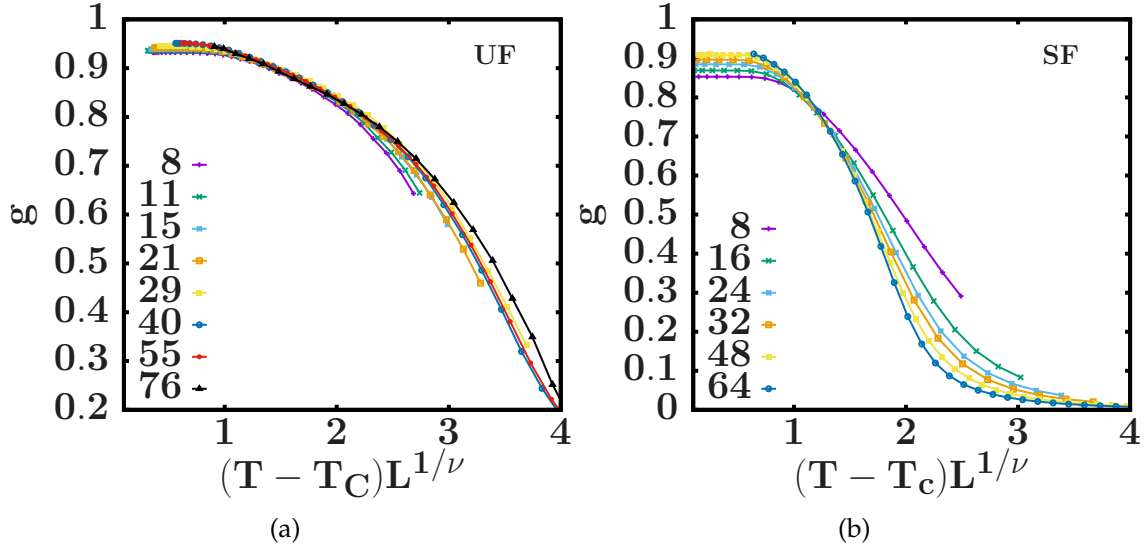


Figure 6.16: Scaling of the Binder cumulant for spin glass with bimodal interactions. The collapse is only valid at intermediate temperatures and for larger system sizes. Figs. 6.16(a) and 6.16(b) show the data for stochastic and under-frustrated systems respectively.

Quantity	Value	Error	$p$ -value
Stochastic, $\nu$	3.62	0.27	$\sim 10^{-7}$
Stochastic, $T_c$	0.062	0.009	$\sim 10^{-7}$
Under-frustrated, $\nu$	3.49	0.21	$\sim 10^{-6}$
Under-frustrated, $T_c$	0.078	0.005	$\sim 10^{-6}$

Table 6.8: Fit values from the Binder cumulant.

freezing at the lower temperatures. As a consequence the fit regime keep on moving with the system size and it is difficult to decide about the fitting range. The fits were done using the same method as for the Gaussian case. In Fig. 6.16, it is evident that the data at very low temperatures (freezing regime) and very high temperatures does not collapse. In Fig. 6.16(a) and Fig. 6.16(b) the collapse for under-frustrated and stochastic frustrated systems were shown, respectively. As expected it looks better for larger system sizes and for smaller systems there are large deviations compared to the Gaussian case. The collapse parameters are listed in the Table 6.8. It is evident from the  $p$ -values that the fits were of very bad quality. The values of the exponents match with the literature values within the errorbars. However, the errorbars can not be trusted because of the poor quality of the fits. The correlation length for the bimodal case shows again the same behaviour as the Binder cumulant. In Fig. 6.17(a), the data for the under-frustrated system

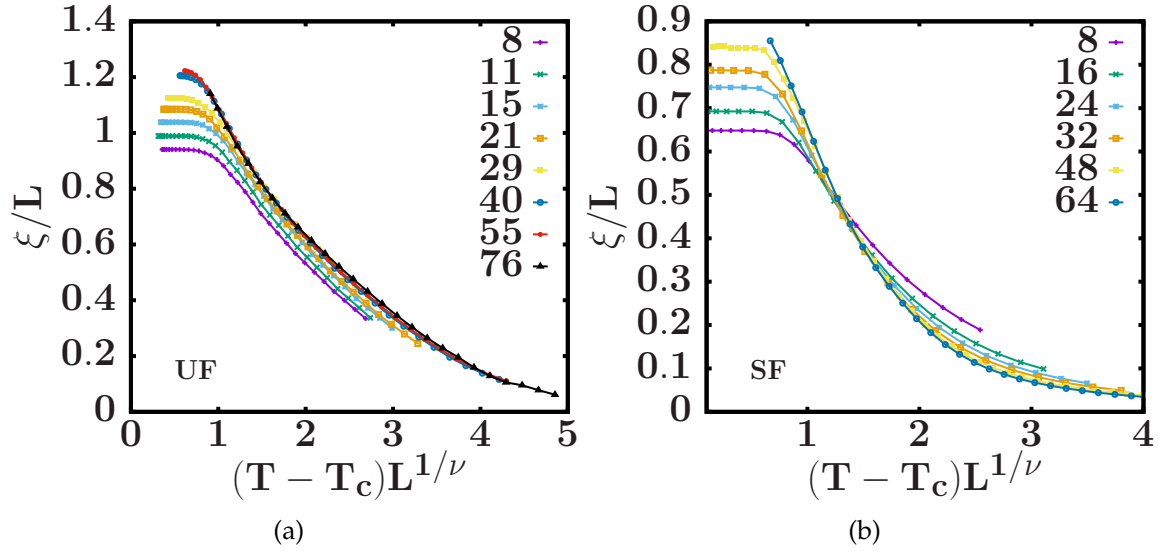


Figure 6.17: Scaling of the correlation length for the bimodal case. Figs. 6.17(a) and 6.17(b) show the data for stochastic and under-frustrated systems respectively.

Quantity	Value	Error	$p$ -value
Stochastic, $\nu$	3.361	0.12	$\sim 10^{-8}$
Stochastic, $T_c$	0.0213	0.0291	$\sim 10^{-8}$
Under-frustrated, $\nu$	3.53	0.31	$\sim 10^{-5}$
Under-frustrated, $T_c$	0.027	0.009	$\sim 10^{-5}$

Table 6.9: Fit values from the correlation length.

is shown. The data for the stochastic frustrated system is shown in Fig. 6.17(b). It is evident from these plots that the scaling behaviour for the under-frustrated case and stochastic frustrated case have same qualitative behaviour. Quantitatively, there were differences e.g. the collapse for the under-frustrated case looks better for longer temperature range when compared to the stochastic case. The collapse parameters are listed in Table 6.9. The  $p$ -values were again extremely small, hence as in the case of Binder cumulant the fits were of very bad quality. However, the values were again comparable to the literature values for the stochastic frustrated system.

The spin glass susceptibility  $\chi$  is another important quantity of interest. Unlike the spin glass system with Gaussian interactions, the bimodal system does not have a unique ground state. Similar to the Gaussian case, the susceptibility scales as Eq. (6.11). Eq. (6.11) is used to collapse the data for different system sizes for the both stochastic and under-frustrated cases. The collapse were shown in Figs. 6.10(a) and 6.10(b). In both under-frustrated and stochastic frustrated cases, the fit form is

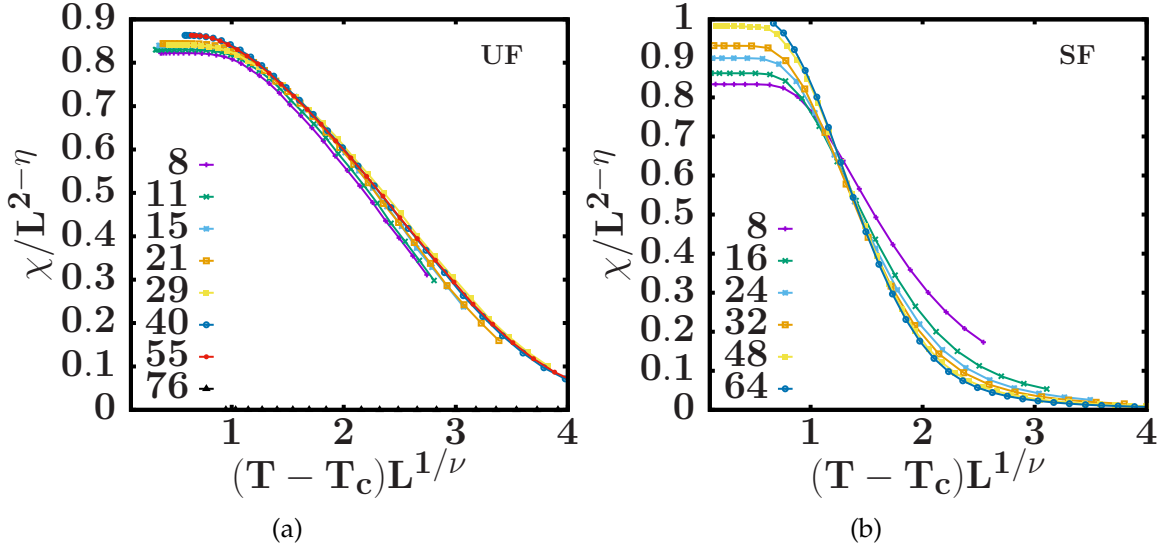


Figure 6.18: Scaling of the spin-glass susceptibility. Figs. 6.18(a) and 6.18(b) show the data for stochastic and under-frustrated systems respectively.

Quantity	Value	Error	$p$ -value
Stochastic, $\nu$	3.125	0.42	$\sim 10^{-9}$
Stochastic, $T_c$	0.0341	0.004	$\sim 10^{-8}$
Stochastic, $\eta$	0.1791	0.0326	$\sim 10^{-9}$
Under-frustrated, $\nu$	3.23	0.28	$\sim 10^{-7}$
Under-frustrated, $T_c$	0.0154	0.02	$\sim 10^{-7}$
Under-frustrated, $\eta$	0.1013	0.0241	$\sim 10^{-9}$

Table 6.10: Fit values from the spin glass susceptibility.

same. However, the value of  $\eta$  for two models differ. For the stochastic frustrated case a good fit can be seen for  $\eta = 0.18$ , but for the under-frustrated system value of  $\eta = 0.10$  gives the better fit. Therefore, the spin-glass susceptibility predicts a different universality class for the under-frustrated systems with a different  $\eta$  value. The fit parameters shown in the Table 6.10.

## 6.6 Summary

The FSS study for the under-frustrated spin glass systems with Gaussian or bimodal interactions does not indicate the existence of phase transition at finite temperature. The Gaussian under-frustrated system behaves exactly like stochastic system and the value of  $\nu$  for both systems is the same. The bimodal under-frustrated

system also have same value of  $\nu$  as for the stochastic system, however in this case the value of  $\eta$  differs for both systems. From this study it can be confirmed that under-frustrated and stochastic frustrated systems do not fall in the same universality class. The results were compatible with the outcome of a recent study [222], which confirms that the different discrete models does not lie in a single universality class. In the mentioned study the continuous distribution of different types have same values of  $\nu$  and  $\eta = 0$  for all studied distributions. In our case we have same continuous distribution, but different frustration contents. As in the above mentioned work, for spin-glass model with Gaussian interactions we also find that the value of  $\eta$  is zero and both under-frustrated and stochastic frustrated systems have same value of  $\nu$  within the errorbars. For the systems with bimodal interactions, values of  $\eta$  differ from one another giving hints towards non-universality. However, a detailed study of the type shown in Ref. [222] has to be performed to confirm the non-universality for under-frustrated bimodal systems.

# Chapter 7

## Conclusions

In Chap. 1 the research questions were described. A thorough research has been done on those questions, and the outcomes are represented in different chapters of this thesis.

After introducing the theoretical concepts of statistical physics, in particular, related to the disordered systems in Chap. 2, the computational methods were introduced in Chap. 3. The algorithms such as Metropolis, parallel tempering and Houdayer cluster algorithm were presented. A new method for tuning the numbers and positions of the temperatures in parallel tempering is introduced. It is argued that power-law ansatz can be used to tune the parameters such as number and positions of temperatures. First, by fixing the number of temperatures and using different values of the power-law exponent, it is demonstrated that there is a sharp value of this tuning exponent. This value grows linearly with the system size  $L$ . Similarly, one could fix the exponent and could vary the number of temperatures. In the second method, we found that the larger system sizes do not have a very sharp peak. This implies that there are many close to optimal values for the number of temperatures for a given value of  $\phi$  exponent. This method within the constraints of fixing one variable can be used to predict the values of the exponent for larger system sizes. However, it should be noted that in the thermodynamic limit these fits would grow to infinity. This is due to the fact that in the power-law ansatz, either the number of temperatures ( $N_T$ ) is fixed and finite-size scaling is performed for  $\phi$  or the value of  $\phi$  is fixed and the finite-size scaling is performed for  $N_T$ .

In Chap. 1, we mentioned the need for huge resources for simulating disordered systems. It is not always easy to get a sufficiently large number of CPUs for these simulations. However, GPUs give a fairly good chance to speed up some of these processes. In Chap. 4, a new algorithm to study disordered systems on GPUs was introduced. Using the parallel structure of GPUs, we could speed up the simulation by two orders of magnitude as compared to a CPU code. There already exists quite

optimized methods to simulate such systems on GPUs, but it is the first implementation of the Houdayer cluster algorithm using CUDA programming. For the Metropolis algorithm, we have speed-ups comparable with other optimized methods. An advantage of our method is its straightforward implementation by using the natural parallelization of disordered systems and simulating one disorder on each thread of the GPU. The Houdayer cluster algorithm part is not as efficient as the Metropolis algorithm. Especially the efficiency does not behave as benchmarked by the CUDA developers. Nevertheless, we also gained a decent speed-up for that case if one fills the number of blocks carefully.

In Chap. 5, the method of tuning the parallel tempering simulation introduced in Chap. 3 is used to carefully tune a set of temperatures to create a benchmark set of disorders. The ground states of this set are known with a very high probability by very long parallel tempering simulations on GPUs. The success probabilities of finding ground states for short parallel tempering simulations and for the graph-cut method were calculated using the known ground state. It is noticed that the graph-cut and parallel tempering techniques return the similar states for small  $q$  and different system sizes. But with increasing  $q$ , the quality of graph-cut results worsens rather quickly. The parallel tempering simulations are computationally much more expensive than the corresponding graph-cut runs for small  $L$  and different values of  $q$ . The code used for parallel tempering simulations is a highly efficient GPU implementation introduced in Chap. 4 but still fails to top the graph-cut performance. We observe a crossover for larger system sizes. The graph-cut method starts outperforming the parallel tempering after a certain system size. Hence, the conclusion is that asymptotically the graph-cut method is the most efficient approach. The success probability for the very efficient graph-cut method can be further increased by using repeated runs. After doing multiple graph-cut runs, and the minimum-energy state found among them can be selected. Both methods have their pros and cons. The parallel tempering guarantees ground state in the infinite run-time limit, however, infinite long simulations are not feasible. On another side, the graph cut method gives the approximate ground state in a fraction of time  $\sim \mathcal{O}(N)$ , irrespective of the number of states  $q$ . The above arguments conclude that the graph cut method is suitable for the study of the two-dimensional random-field Potts model. In particular, for  $q \leq 4$ , the returned configurations are either exact ( $q = 2$ ) or very close to the exact ground states. This model has received very little attention due to the unavailability of efficient computational methods. This method opens new possibilities for studying random-field Potts.

The FSS study for the under-frustrated spin glass systems with Gaussian or bimodal interactions does not show the existence of phase transition at finite temperature. The Gaussian under-frustrated system behaves exactly like the stochastic system, and the value of  $\nu$  for both systems is the same. The bimodal under-frustrated system also has the same value of  $\nu$  as for the stochastic system, however, in this case, the value of  $\eta$  differs for both systems. A conclusive statement about

non-universality of  $\eta$  cannot be made as the quality of collapse plots is not very good. But there are hints that under-frustrated and stochastic frustrated systems with bimodal distribution might not fall in the same universality class. These results seem compatible with the outcome of a recent study performed in Ref. [222], which confirms that the different discrete models do not lie in a single universality class. However, a more detailed study of the type shown in Ref. [222] has to be performed to confirm the non-universality for under-frustrated bimodal systems. This study shows that there is no clear evidence for a phase transition at a non-zero temperature for a two-dimensional spin glass model. The result is consistent for both models with bimodal and Gaussian interactions.



# Bibliography

- [1] Wilhelm Lenz. Beitrag zum verständnis der magnetischen erscheinungen in festen körpern. *Z. Phys.*, 21:613–615, 1920.
- [2] Ernst Ising. Beitrag zur theorie des ferromagnetismus. *Zeitschrift für Physik A Hadrons and Nuclei*, 31(1):253–258, 1925.
- [3] H Eugene Stanley. Introduction to phase transitions and critical phenomena. *Introduction to Phase Transitions and Critical Phenomena*, by H Eugene Stanley, pp. 336. Foreword by H Eugene Stanley. Oxford University Press, Jul 1987. ISBN-10: 0195053168. ISBN-13: 9780195053166, page 336, 1987.
- [4] John Cardy. *Scaling and renormalization in statistical physics*, volume 5. Cambridge university press, 1996.
- [5] James J Binney, Nigel J Dowrick, Andrew J Fisher, and Mark Newman. *The theory of critical phenomena: an introduction to the renormalization group*. Oxford University Press, Inc., 1992.
- [6] Cyril Domb. *Phase transitions and critical phenomena*, volume 19. Academic press, 2000.
- [7] Lars Onsager. Statistical hydrodynamics. *Il Nuovo Cimento (1943-1954)*, 6:279–287, 1949.
- [8] Bruria Kaufman. Crystal statistics. ii. partition function evaluated by spinor analysis. *Physical Review*, 76(8):1232, 1949.
- [9] Arthur E. Ferdinand and Michael E. Fisher. Bounded and inhomogeneous ising models. i. specific-heat anomaly of a finite lattice. *Phys. Rev.*, 185:832–846, Sep 1969.
- [10] Chen Ning Yang. The spontaneous magnetization of a two-dimensional ising model. *Physical Review*, 85(5):808, 1952.
- [11] C. H. Chang. The spontaneous magnetization of a two-dimensional rectangular ising model. *Phys. Rev.*, 88:1422–1422, Dec 1952.

- [12] W. P. Orrick, B. G. Nickel, A. J. Guttmann, and J. H. H. Perk. Critical behavior of the two-dimensional ising susceptibility. *Phys. Rev. Lett.*, 86:4120–4123, Apr 2001.
- [13] WP Orrick, B Nickel, AJ Guttmann, and JHH Perk. The susceptibility of the square lattice ising model: new developments. *Journal of Statistical Physics*, 102(3):795–841, 2001.
- [14] Rodney J Baxter. *Exactly solved models in statistical mechanics*. 1982.
- [15] Barry M McCoy and Tai Tsun Wu. *The two-dimensional Ising model*. Courier Corporation, 2014.
- [16] Robert B. Griffiths. Dependence of critical indices on a parameter. *Phys. Rev. Lett.*, 24:1479–1482, Jun 1970.
- [17] BD Josephson. Inequality for the specific heat: I. derivation. *Proceedings of the Physical Society*, 92(2):269, 1967.
- [18] BD Josephson. Inequality for the specific heat: II. application to critical phenomena. *Proceedings of the Physical Society*, 92(2):276, 1967.
- [19] GS Rushbrooke. On the thermodynamics of the critical region for the ising problem. *The Journal of Chemical Physics*, 39(3):842–843, 1963.
- [20] Robert B Griffiths. Thermodynamic inequality near the critical point for ferromagnets and fluids. *Physical Review Letters*, 14(16):623, 1965.
- [21] Michael E Fisher. Rigorous inequalities for critical-point correlation exponents. *Physical Review*, 180(2):594, 1969.
- [22] M. Palassini and A. P. Young. *Phys. Rev. Lett.*, 83:5126, 1999.
- [23] H. G. Ballesteros, A. Cruz, L. A. Fernandez, V. Martin-Mayor, J. Pech, J. J. Ruiz-Lorenzo, A. Tarancon, P. Tellez, C. L. Ullod, and C. Ungil. Critical behavior of the three-dimensional Ising spin glass. *Phys. Rev. B*, 62:14237–14245, 2000.
- [24] Yoseph Imry and Shang-keng Ma. Random-field instability of the ordered state of continuous symmetry. *Phys. Rev. Lett.*, 35:1399–1401, Nov 1975.
- [25] Amnon Aharony, Yoseph Imry, and Shang-keng Ma. Lowering of dimensionality in phase transitions with random fields. *Physical Review Letters*, 37(20):1364, 1976.
- [26] A P Young. On the lowering of dimensionality in phase transitions with random fields. *Journal of Physics C: Solid State Physics*, 10(9):L257, 1977.

- [27] S Fishman and A Aharony. Random field effects in disordered anisotropic antiferromagnets. *Journal of Physics C: Solid State Physics*, 12(18):L729, 1979.
- [28] GIORGIO Parisi and NICOLAS Sourslas. Random magnetic fields, supersymmetry, and negative dimensions. *Physical Review Letters*, 43(11):744, 1979.
- [29] John Z. Imbrie. Lower critical dimension of the random-field ising model. *Phys. Rev. Lett.*, 53:1747–1750, Oct 1984.
- [30] Michael Gofman, Joan Adler, Amnon Aharony, A. B. Harris, and Moshe Schwartz. Evidence for two exponent scaling in the random field ising model. *Phys. Rev. Lett.*, 71:1569–1572, Sep 1993.
- [31] D.P. Belanger and A.P. Young. The random field ising model. *Journal of Magnetism and Magnetic Materials*, 100(1–3):272 – 291, 1991.
- [32] Heiko Rieger. Critical behavior of the three-dimensional random-field ising model: Two-exponent scaling and discontinuous transition. *Physical Review B*, 52(9):6659, 1995.
- [33] T. Nattermann. Theory of the Random Field Ising Model. In A. P. Young, editor, *Spin glasses and random fields*. World Scientific, Singapore, 1998.
- [34] Z Slanič and DP Belanger. The random-field specific heat critical behavior at high magnetic concentration: Fe 0.93 zn 0.07 f 2. *Journal of magnetism and magnetic materials*, 186(1):65–73, 1998.
- [35] D. P. Belanger, A. R. King, V. Jaccarino, and J. L. Cardy. Random-field critical behavior of a  $d = 3$  ising system. *Phys. Rev. B*, 28:2522–2526, Sep 1983.
- [36] R. L. C. Vink, K. Binder, and H. Löwen. Critical behavior of colloid-polymer mixtures in random porous media. *Phys. Rev. Lett.*, 97:230603, Dec 2006.
- [37] Mario Alberto Annunziata and Andrea Pelissetto. Colloids and polymers in random colloidal matrices: Demixing under good-solvent conditions. *Phys. Rev. E*, 86:041804, Oct 2012.
- [38] Elbio Dagotto. Complexity in strongly correlated electronic systems. *Science*, 309(5732):257–262, 2005.
- [39] J. Burgy, M. Mayr, V. Martin-Mayor, A. Moreo, and E. Dagotto. Colossal effects in transition metal oxides caused by intrinsic inhomogeneities. *Phys. Rev. Lett.*, 87:277202, Dec 2001.
- [40] John Cardy and Jesper Lykke Jacobsen. Critical behavior of random-bond potts models. *Phys. Rev. Lett.*, 79:4063–4066, Nov 1997.

- [41] L. A. Fernández, A. Gordillo-Guerrero, V. Martín-Mayor, and J. J. Ruiz-Lorenzo. First-order transition in a three-dimensional disordered system. *Phys. Rev. Lett.*, 100:057201, Feb 2008.
- [42] L. A. Fernandez, A. Gordillo-Guerrero, V. Martin-Mayor, and J. J. Ruiz-Lorenzo. Numerical test of the cardy-jacobsen conjecture in the site-diluted potts model in three dimensions. *Phys. Rev. B*, 86:184428, 2012.
- [43] James P. Sethna, Karin Dahmen, Sivan Kartha, James A. Krumhansl, Bruce W. Roberts, and Joel D. Shore. Hysteresis and hierarchies: Dynamics of disorder-driven first-order phase transformations. *Phys. Rev. Lett.*, 70:3347–3350, May 1993.
- [44] Olga Perković, Karin A. Dahmen, and James P. Sethna. Disorder-induced critical phenomena in hysteresis: Numerical scaling in three and higher dimensions. *Phys. Rev. B*, 59:6106–6119, Mar 1999.
- [45] D. M. Silevitch, G. Aeppli, and T. F. Rosenbaum. Switchable hardening of a ferromagnet at fixed temperature. *Proceedings of the National Academy of Sciences*, 107(7):2797–2800, 2010.
- [46] J. Villain. Nonequilibrium "critical" exponents in the random-field ising model. *Phys. Rev. Lett.*, 52:1543–1546, Apr 1984.
- [47] A J Bray and M A Moore. Scaling theory of the random-field ising model. *Journal of Physics C: Solid State Physics*, 18(28):L927, 1985.
- [48] Daniel S. Fisher. Scaling and critical slowing down in random-field ising systems. *Phys. Rev. Lett.*, 56:416–419, Feb 1986.
- [49] A. Nihat Berker and Susan R. McKay. Modified hyperscaling relation for phase transitions under random fields. *Phys. Rev. B*, 33:4712–4715, Apr 1986.
- [50] J. Bricmont and A. Kupiainen. Lower critical dimension for the random-field ising model. *Phys. Rev. Lett.*, 59:1829–1832, Oct 1987.
- [51] M. E. J. Newman, B. W. Roberts, G. T. Barkema, and J. P. Sethna. Real-space renormalization group for the random-field ising model. *Phys. Rev. B*, 48:16533–16538, Dec 1993.
- [52] J. Machta, M. E. J. Newman, and L. B. Chayes. Replica-exchange algorithm and results for the three-dimensional random field ising model. *Phys. Rev. E*, 62:8782–8789, Dec 2000.
- [53] M. E. J. Newman and G. T. Barkema. *Phys. Rev. E*, 53:393, 1996.

- [54] M. Itakura. Phase diagram of the three-dimensional gaussian random field ising model: A monte carlo renormalization-group study. *Phys. Rev. B*, 64:012415, Jun 2001.
- [55] N. G. Fytas and A. Malakis. Phase diagram of the 3d bimodal random-field ising model. *The European Physical Journal B*, 61(1):111–120, 2008.
- [56] Amnon Aharony. Tricritical points in systems with random fields. *Phys. Rev. B*, 18:3318–3327, Oct 1978.
- [57] Nikolaos G Fytas, Víctor Martín-Mayor, Marco Picco, and Nicolas Sourlas. Restoration of dimensional reduction in the random-field ising model at five dimensions. *Physical Review E*, 95(4):042117, 2017.
- [58] G. Parisi. *Field Theory, Disorder and Simulations*. World Scientific, 1994.
- [59] Giorgio Parisi and Nicolas Sourlas. Scale invariance in disordered systems: The example of the random-field ising model. *Phys. Rev. Lett.*, 89:257204, Dec 2002.
- [60] Matthieu Tissier and Gilles Tarjus. Supersymmetry and its spontaneous breaking in the random field ising model. *Phys. Rev. Lett.*, 107:041601, Jul 2011.
- [61] Z. Slanič, D. P. Belanger, and J. A. Fernandez-Baca. Equilibrium random-field ising critical scattering in the antiferromagnet  $\text{Fe}_{0.93}\text{Zn}_{0.07}\text{F}_2$ . *Phys. Rev. Lett.*, 82:426–429, Jan 1999.
- [62] F Ye, M Matsuda, S Katano, H Yoshizawa, D.P Belanger, E.T Seppälä, J.A Fernandez-Baca, and M.J Alava. Percolation fractal dimension in scattering line shapes of the random-field ising model. *Journal of Magnetism and Magnetic Materials*, 272–276, Part 2:1298 – 1299, 2004. Proceedings of the International Conference on Magnetism (ICM 2003).
- [63] DP Belanger. Experiments on the random field ising model. pages 251–275, 1998.
- [64] Heiko Rieger. Nonequilibrium dynamics and aging in the three-dimensional ising spin-glass model. *Journal of Physics A: Mathematical and General*, 26(15):L615, 1993.
- [65] U. Nowak, K.D. Usadel, and J. Esser. Modified scaling relation for the random-field ising model. *Physica A: Statistical Mechanics and its Applications*, 250(1–4):1 – 7, 1998.
- [66] L. A. Fernandez, V. Martin-Mayor, and D. Yllanes. Critical behavior of the dilute antiferromagnet in a field. *Phys. Rev. B*, 84:100408(R), 2011.

- [67] N. G. Fytas, A. Malakis, and K. Eftaxias. First-order transition features of the 3d bimodal random-field ising model. *Journal of Statistical Mechanics: Theory and Experiment*, 2008(3):P03015, 2008.
- [68] R. L. C. Vink, T. Fischer, and K. Binder. *Phys. Rev. E*, 82:051134, 2010.
- [69] Björn Ahrens, Jianping Xiao, Alexander K. Hartmann, and Helmut G. Katzgraber. Diluted antiferromagnets in a field seem to be in a different universality class than the random-field ising model. *Phys. Rev. B*, 88:174408, Nov 2013.
- [70] M. Picco and N. Surlas. Diluted antiferromagnetic 3d ising model in a field. *EPL (Europhysics Letters)*, 109(3):37001, 2015.
- [71] Andrew T. Ogielski. Integer optimization and zero-temperature fixed point in ising random-field systems. *Phys. Rev. Lett.*, 57:1251–1254, Sep 1986.
- [72] A.K. Hartmann and K.D. Usadel. Exact determination of all ground states of random field systems in polynomial time. *Physica A: Statistical Mechanics and its Applications*, 214(2):141 – 152, 1995.
- [73] Hartmann, A. K. and Nowak, U. Universality in three dimensional random-field ground states. *Eur. Phys. J. B*, 7(1):105–109, 1999.
- [74] A. K. Hartmann and A. P. Young. Specific-heat exponent of random-field systems via ground-state calculations. *Phys. Rev. B*, 64:214419, Nov 2001.
- [75] A. Alan Middleton. Critical slowing down in polynomial time algorithms. *Phys. Rev. Lett.*, 88:017202, Dec 2001.
- [76] A. Alan Middleton and Daniel S. Fisher. Three-dimensional random-field ising magnet: Interfaces, scaling, and the nature of states. *Phys. Rev. B*, 65:134411, Mar 2002.
- [77] I. Dukovski and J. Machta. Ground-state numerical study of the three-dimensional random-field ising model. *Phys. Rev. B*, 67:014413, Jan 2003.
- [78] Yong Wu and Jonathan Machta. Ground states and thermal states of the random field ising model. *Phys. Rev. Lett.*, 95:137208, Sep 2005.
- [79] Nicolas Surlas. Universality in random systems: the case of the 3d random field ising model. *Computer Physics Communications*, 121:183 – 187, 1999. Proceedings of the Europhysics Conference on Computational Physics {CCP} 1998.
- [80] J.-C. Anglès d’Auriac and N. Surlas. The 3d random field ising model at zero temperature. *EPL (Europhysics Letters)*, 39(5):473, 1997.

- [81] M. R. Swift, A. J. Bray, A. Maritan, M. Cieplak, and J. R. Banavar. Scaling of the random-field ising model at zero temperature. *EPL (Europhysics Letters)*, 38(4):273, 1997.
- [82] Serge Galam and Joseph L. Birman. Random-field distributions and tricritical points. *Phys. Rev. B*, 28:5322–5322, Nov 1983.
- [83] V. K. Saxena. Low-temperature phase transitions in a random-field ising model. *Phys. Rev. B*, 30:4034–4036, Oct 1984.
- [84] Miron Kaufman, Philip E. Klunzinger, and A. Khurana. Multicritical points in an ising random-field model. *Phys. Rev. B*, 34:4766–4770, Oct 1986.
- [85] Rafael M. Sebastianes and V. K. Saxena. Phase diagram of the random-field ising model with a trimodal distribution. *Phys. Rev. B*, 35:2058–2060, Feb 1987.
- [86] A. S. de Arruda, W. Figueiredo, R. M. Sebastianes, and V. K. Saxena. Field distributions and tricritical points in a random-field ising model: Mean-field renormalization-group approach. *Phys. Rev. B*, 39:4409–4417, Mar 1989.
- [87] A. Houghton, A. Khurana, and F. J. Seco. Fluctuation-driven first-order phase transition, below four dimensions, in the random-field ising model with a gaussian random-field distribution. *Phys. Rev. Lett.*, 55:856–858, Aug 1985.
- [88] Nikolaos G. Fytas and Víctor Martín-Mayor. Universality in the three-dimensional random-field ising model. *Phys. Rev. Lett.*, 110:227201, May 2013.
- [89] Marco Picco and Nicolas Sourlas. On the phase transition of the 3d random field ising model. *Journal of Statistical Mechanics: Theory and Experiment*, 2014(3):P03019, 2014.
- [90] Fa-Yueh Wu. The potts model. *Reviews of modern physics*, 54(1):235, 1982.
- [91] Renfrey Burnard Potts. Some generalized order-disorder transformations. In *Mathematical proceedings of the cambridge philosophical society*, volume 48, pages 106–109. Cambridge University Press, 1952.
- [92] K Binder and JD Reger. Theory of orientational glasses models, concepts, simulations. *Advances in Physics*, 41:547–627, 1992.
- [93] KH Michel. Theory of the orientational glass state in mixed crystals  $m(\text{cn}) \times x_1 - x_2$ . ii. dynamics. *Physical Review B*, 35(3):1414, 1987.
- [94] Amnon Aharony, KA Müller, and W Berlinger. Trigonal-to-tetragonal transition in stressed  $\text{SrTiO}_3$ : A realization of the three-state potts model. *Physical Review Letters*, 38(1):33, 1977.

- [95] E Domany, Y Shnidman, and D Mukamel. Type i fcc antiferromagnets in a magnetic field: a realisation of the  $q=3$ - and  $q=4$ -state potts models. *Journal of Physics C: Solid State Physics*, 15(14):L495, 1982.
- [96] Daniel Blankschtein, Yonathan Shapir, and Amnon Aharony. Potts models in random fields. *Physical Review B*, 29(3):1263, 1984.
- [97] Hidetoshi Nishimori. Potts model in random fields. *Physical Review B*, 28(7):4011, 1983.
- [98] Klaus Eichhorn and Kurt Binder. Monte carlo investigation of the three-dimensional random-field three-state potts model. *Journal of Physics: Condensed Matter*, 8(28):5209, 1996.
- [99] K Eichhorn and K Binder. The three-dimensional three-state potts ferromagnet exposed to random fields: evidence for a second order transition. *Zeitschrift für Physik B Condensed Matter*, 99(1):413–423, 1995.
- [100] P Reed. The potts model in a random field: a monte carlo study. *Journal of Physics C: Solid State Physics*, 18(20):L615, 1985.
- [101] Rodney J Baxter. Potts model at the critical temperature. *Journal of Physics C: Solid State Physics*, 6(23):L445, 1973.
- [102] Yadin Y Goldschmidt and Gu Xu. Phase diagrams of the random-field potts model in three dimensions. *Physical Review B*, 32(3):1876, 1985.
- [103] J. Owen, M. Browne, W. D. Knight, and C. Kittel. Electron and nuclear spin resonance and magnetic susceptibility experiments on dilute alloys of mn in cu. *Phys. Rev.*, 102:1501–1507, Jun 1956.
- [104] J. de Nobel and F.J. Chatenier. Specific heats of dilute alloys of manganese in silver and copper at low temperatures and in magnetic fields. *Physica*, 25:969–979, January 1959.
- [105] J.E. Zimmerman. Low-temperature specific heat of dilute cu-mn alloys. *J. Phys. Chem. Solids*, 17:52–56, December 1960. An additional author, F.E. Hoare, appears in Edwards' citation of this article.
- [106] W. Marshall. Specific heat of dilute alloys. *Phys. Rev.*, 118:1519–1523, Jun 1960.
- [107] C. Zener. Interaction between the  $d$  shells in the transition metals. *Phys. Rev.*, 81:440–444, Feb 1951.
- [108] Clarence Zener. Interaction between the  $d$ -shells in the transition metals. ii. ferromagnetic compounds of manganese with perovskite structure. *Phys. Rev.*, 82:403–405, May 1951.

- [109] Clarence Zener. Interaction between the  $d$ -shells in the transition metals. iii. calculation of the weiss factors in fe, co, and ni. *Phys. Rev.*, 83:299–301, Jul 1951.
- [110] T. Kasuya. *Prog. Theor. Phys.*, 16:45, 1956.
- [111] K. Yosida. Magnetic properties of cu-mn alloys. *Phys. Rev.*, 106:893–898, Jun 1957.
- [112] M.A. Ruderman and C. Kittel. *Phys. Rev.*, 96:99, 1954.
- [113] R. Brout. Statistical mechanical theory of a random ferromagnetic system. *Phys. Rev.*, 115:824–835, Aug 1959.
- [114] Michael W. Klein and Robert Brout. Statistical mechanics of dilute copper manganese. *Phys. Rev.*, 132:2412–2426, Dec 1963.
- [115] C. G. Montgomery, J. I. Krugler, and R. M. Stubbs. Green's-function theory of a disordered heisenberg ferromagnet. *Phys. Rev. Lett.*, 25:669–672, Sep 1970.
- [116] P.W. Anderson. Localisation theory and cumn problems - spin glasses. *Materials Research Bulletin*, 5:549, 1970.
- [117] S. F. Edwards and P. W. Anderson. Theory of spin glasses. *Journal of Physics F: Metal Physics*, 5:965, 1975.
- [118] S. F. Edwards and P. W. Anderson. Theory of spin glasses. ii. *J. Phys. F*, 6(10):1927, 1976.
- [119] M. Mézard, G. Parisi, and M. Virasoro. *Spin-Glass Theory and Beyond*. World Scientific, Singapore, 1987.
- [120] G. Parisi. Order parameter for spin glasses. *Phys. Rev. Lett.*, 50:1946, 1983.
- [121] D Sherrington and W Southern. Spin glass versus ferromagnet. *Journal of Physics F: Metal Physics*, 5(5):L49, 1975.
- [122] K. H. Fischer. Static properties of spin glasses. *Phys. Rev. Lett.*, 34:1438–1441, Jun 1975.
- [123] David Sherrington and Scott Kirkpatrick. Solvable model of a spin-glass. *Phys. Rev. Lett.*, 35:1792–1796, Dec 1975.
- [124] J. R. L. de Almeida and D. J. Thouless. Stability of the Sherrington-Kirkpatrick solution of a spin glass model. *J. Phys. A: Math. Gen.*, 11:983, 1978.
- [125] A. J. Bray and M. A. Moore. Replica-symmetry breaking in spin-glass theories. *Phys. Rev. Lett.*, 41:1068–1072, Oct 1978.

- [126] A.J. Bray and M.A. Moore. Replica symmetry and massless modes in the ising spin glass. *Journal of Physics C: Solid State Physics*, 12(1):79, 1979.
- [127] A. B. Harris, T. C. Lubensky, and Jing-Huei Chen. Critical properties of spin-glasses. *Phys. Rev. Lett.*, 36:415–418, Feb 1976.
- [128] A P Young and R B Stinchcombe. Real-space renormalization group calculations for spin glasses and dilute magnets. *Journal of Physics C: Solid State Physics*, 9(24):4419, 1976.
- [129] B W Southern and A P Young. Real space rescaling study of spin glass behaviour in three dimensions. *Journal of Physics C: Solid State Physics*, 10(12):2179, 1977.
- [130] D. J. Thouless, P. W. Anderson, and R. G. Palmer. Solution of 'solvable model of a spin glass'. *Phil. Mag.*, 35(3):593–601, 1977.
- [131] Scott Kirkpatrick and David Sherrington. Infinite-ranged models of spin-glasses. *Phys. Rev. B*, 17:4384–4403, Jun 1978.
- [132] G. Parisi. Toward a mean field theory for spin glasses. *Phys. Lett.*, 73A:203, 1979.
- [133] G. Parisi. The order parameter for spin glasses: a function on the interval 0-1. *J. Phys. A: Math. Gen.*, 13:1101, 1980.
- [134] G Parisi. Magnetic properties of spin glasses in a new mean field theory. *Journal of Physics A: Mathematical and General*, 13(5):1887, 1980.
- [135] G. Parisi. A sequence of approximated solutions to the s-k model for spin glasses. *J. Phys. A: Math. Gen.*, 13:L115–L121, 1980.
- [136] M. Mézard, G. Parisi, N. Sourlas, G. Toulouse, and M.A. Virasoro. Nature of the spin-glass phase. *Phys. Rev. Lett.*, 52:1156, 1984.
- [137] M. Mézard and M.A. Virasoro. On the microstructure of ultrametricity. *J. Physique*, 46:1293–1307, 1985.
- [138] R. Rammal, G. Toulouse, and M. A. Virasoro. Ultrametricity for physicists. *Rev. Mod. Phys.*, 58:765–788, Jul 1986.
- [139] A.J. Bray and M.A. Moore. Metastable states in spin glasses. *Journal of Physics C: Solid State Physics*, 13(19):L469, 1980.
- [140] C. de Dominicis, Gabay, M., Garel, T., and Orland, H. White and weighted averages over solutions of thouless anderson palmer equations for the sherrington kirkpatrick spin glass. *J. Phys. France*, 41(9):923–930, 1980.

- [141] A.P. Young. The tap equations revisited: a qualitative picture of the sk spin glass model. *Journal of Physics C: Solid State Physics*, 14(34):L1085, 1981.
- [142] N. D. Mackenzie and A. P. Young. Lack of ergodicity in the infinite-range ising spin-glass. *Phys. Rev. Lett.*, 49:301–304, Aug 1982.
- [143] Bernard Derrida. Random-energy model: An exactly solvable model of disordered systems. *Phys. Rev. B*, 24:2613–2626, Sep 1981.
- [144] Francesco Guerra and Fabio Lucio Toninelli. The thermodynamic limit in mean field spin glass models. *Communications in Mathematical Physics*, 230(1):71–79, 2002.
- [145] F. Guerra. Broken replica symmetry bounds in the mean field spin glass model. *Comm. Math. Phys.*, 233:1–12, 2003.
- [146] M. Talagrand. The Parisi formula. *Ann. of Math.*, 163:221, 2006.
- [147] A. J. Bray and M. A. Moore. Critical behavior of the three-dimensional ising spin glass. *Phys. Rev. B*, 31:631–633, Jan 1985.
- [148] W. L. McMillan. Domain-wall renormalization-group study of the three-dimensional random ising model at finite temperature. *Phys. Rev. B*, 31:340–341, Jan 1985.
- [149] W. L. McMillan. *J. Phys. C: Solid State Phys.*, 17:3179, 1984.
- [150] D. S. Fisher and D. A. Huse. Ordered phase of short-range ising spin-glasses. *Phys. Rev. Lett.*, 56:1601, Apr 1986.
- [151] D. S. Fisher and D. A. Huse. Absence of many states in realistic spin glasses. *J. Phys. A: Math. Gen.*, 20:L1005, 1987.
- [152] David A. Huse and Daniel S. Fisher. Dynamics of droplet fluctuations in pure and random ising systems. *Phys. Rev. B*, 35:6841–6846, May 1987.
- [153] D. S. Fisher and D. A. Huse. *Phys. Rev. B*, 38:373, 1988.
- [154] D. S. Fisher and D. A. Huse. *Phys. Rev. B*, 38:386, 1988.
- [155] A.A. Migdal. Phase transitions in gauge and spin-lattice systems. *Zhurnal Eksperimentalnoi i teoreticheskoi fiziki*, 1975.
- [156] L.P. Kadanoff. *Annals of Physics*, 100:359–394, 1976.
- [157] P. W. Anderson and C. M. Pond. Anomalous dimensionalities in the spin-glass problem. *Phys. Rev. Lett.*, 40:903–906, Mar 1978.

- [158] M. A. Moore and A. J. Bray. Disappearance of the de Almeida-Thouless line in six dimensions. *Phys. Rev. B*, 83:224408, 2011.
- [159] G. Parisi and T. Temesvári. Replica symmetry breaking in and around six dimensions. *Nucl. Phys. B*, 858:293, 2012.
- [160] J. Yeo and M. A. Moore. *Phys. Rev. E*, 86:052501, 2012.
- [161] B. Yucesoy, Helmut G. Katzgraber, and J. Machta. Evidence of non-mean-field-like low-temperature behavior in the edwards-anderson spin-glass model. *Phys. Rev. Lett.*, 109:177204, Oct 2012.
- [162] A. Billoire, L. A. Fernandez, A. Maiorano, E. Marinari, V. Martin-Mayor, G. Parisi, F. Ricci-Tersenghi, J. J. Ruiz-Lorenzo, and D. Yllanes. Comment on “evidence of non-mean-field-like low-temperature behavior in the edwards-anderson spin-glass model”. *Phys. Rev. Lett.*, 110:219701, 2013.
- [163] B. Yucesoy, Helmut G. Katzgraber, and J. Machta. Reply to comment. *Phys. Rev. Lett.*, 110:219702, 2013.
- [164] Nicholas Metropolis, Arianna W Rosenbluth, Marshall N Rosenbluth, Augusta H Teller, and Edward Teller. Equation of state calculations by fast computing machines. *The journal of chemical physics*, 21(6):1087–1092, 1953.
- [165] Robert H Swendsen and Jian-Sheng Wang. Replica monte carlo simulation of spin-glasses. *Physical Review Letters*, 57(21):2607, 1986.
- [166] Koji Hukushima and Koji Nemoto. Exchange monte carlo method and application to spin glass simulations. *Journal of the Physical Society of Japan*, 65(6):1604–1608, 1996.
- [167] E Marinari, G Parisi, and JJ Ruiz-Lorenzo. Spin glasses and random fields. *Directions in Condensed Matter Physics, edited by A. Young*, 12, 1998.
- [168] David J Earl and Michael W Deem. Parallel tempering: Theory, applications, and new perspectives. *Physical Chemistry Chemical Physics*, 7(23):3910–3916, 2005.
- [169] Helmut G Katzgraber. Introduction to monte carlo methods. *arXiv preprint arXiv:0905.1629*, 2009.
- [170] Martin Hasenbusch, Andrea Pelissetto, and Ettore Vicari. Critical behavior of three-dimensional ising spin glass models. *Physical Review B*, 78(21):214205, 2008.
- [171] Giacomo Ceccarelli, Andrea Pelissetto, and Ettore Vicari. Ferromagnetic-glassy transitions in three-dimensional ising spin glasses. *Physical Review B*, 84(13):134202, 2011.

- [172] A Billoire, LA Fernandez, A Maiorano, E Marinari, V Martin-Mayor, and D Yllanes. Finite-size scaling analysis of the distributions of pseudo-critical temperatures in spin glasses. *Journal of Statistical Mechanics: Theory and Experiment*, 2011(10):P10019, 2011.
- [173] Koji Hukushima, Hajime Takayama, and Hajime Yoshino. Exchange monte carlo dynamics in the sk model. *Journal of the Physical Society of Japan*, 67(1):12–15, 1998.
- [174] HG Ballesteros, A Cruz, LA Fernandez, V Martin-Mayor, J Pech, JJ Ruiz-Lorenzo, A Tarancon, P Tellez, CL Ullod, and C Ungil. Critical behavior of the three-dimensional ising spin glass. *Physical Review B*, 62(21):14237, 2000.
- [175] Helmut G Katzgraber, Matteo Palassini, and AP Young. Monte carlo simulations of spin glasses at low temperatures. *Physical Review B*, 63(18):184422, 2001.
- [176] Helmut G Katzgraber, Mathias Körner, and AP Young. Universality in three-dimensional ising spin glasses: A monte carlo study. *Physical Review B*, 73(22):224432, 2006.
- [177] Helmut G Katzgraber, Simon Trebst, David A Huse, and Matthias Troyer. Feedback-optimized parallel tempering monte carlo. *Journal of Statistical Mechanics: Theory and Experiment*, 2006(03):P03018, 2006.
- [178] Elmar Bittner, Andreas Nußbaumer, and Wolfhard Janke. Make life simple: Unleash the full power of the parallel tempering algorithm. *Physical review letters*, 101(13):130603, 2008.
- [179] David A Kofke. On the acceptance probability of replica-exchange monte carlo trials. *The Journal of chemical physics*, 117(15):6911–6914, 2002.
- [180] Aminata Kone and David A Kofke. Selection of temperature intervals for parallel-tempering simulations. *The Journal of chemical physics*, 122(20):206101, 2005.
- [181] Cristian Predescu, Mihaela Predescu, and Cristian V Ciobanu. The incomplete beta function law for parallel tempering sampling of classical canonical systems. *The Journal of chemical physics*, 120(9):4119–4128, 2004.
- [182] Dubravko Sabo, Markus Meuwly, David L Freeman, and JD Doll. A constant entropy increase model for the selection of parallel tempering ensembles. *The Journal of chemical physics*, 128(17):174109, 2008.
- [183] JP Neirotti, F Calvo, David L Freeman, and JD Doll. Phase changes in 38-atom lennard-jones clusters. i. a parallel tempering study in the canonical ensemble. *The Journal of Chemical Physics*, 112(23):10340–10349, 2000.

- [184] F Calvo. All-exchanges parallel tempering. *The Journal of chemical physics*, 123(12):124106, 2005.
- [185] Paul Brenner, Christopher R Sweet, Dustin VonHandorf, and Jesús A Izaguirre. Accelerating the replica exchange method through an efficient all-pairs exchange. *The Journal of chemical physics*, 126(7):074103, 2007.
- [186] J. Houdayer. A cluster monte carlo algorithm for 2-dimensional spin glasses. *The European Physical Journal B - Condensed Matter and Complex Systems*, 22(4):479–484, 2001.
- [187] Zheng Zhu, Andrew J Ochoa, and Helmut G Katzgraber. Efficient cluster algorithm for spin glasses in any space dimension. *Physical review letters*, 115(7):077201, 2015.
- [188] Gordon E Moore. Cramming more components onto integrated circuits, reprinted from electronics, volume 38, number 8, april 19, 1965, pp. 114 ff. *IEEE Solid-State Circuits Society Newsletter*, 20(3):33–35, 2006.
- [189] Martin Weigel. Simulating spin models on gpu. *Computer Physics Communications*, 182(9):1833–1836, 2011.
- [190] Jason Sanders and Edward Kandrot. *CUDA by example: an introduction to general-purpose GPU programming*. Addison-Wesley Professional, 2010.
- [191] Martin Weigel and Taras Yavorskii. Gpu accelerated monte carlo simulations of lattice spin models. *Physics Procedia*, 15:92–96, 2011.
- [192] Taras Yavorskii and Martin Weigel. Optimized gpu simulation of continuous-spin glass models. *The European Physical Journal Special Topics*, 210(1):159–173, 2012.
- [193] Ye Fang, Sheng Feng, Ka-Ming Tam, Zhifeng Yun, Juana Moreno, Jagannathan Ramanujam, and Mark Jarrell. Parallel tempering simulation of the three-dimensional edwards–anderson model with compact asynchronous multispin coding on gpu. *Computer Physics Communications*, 185(10):2467–2478, 2014.
- [194] Matteo Lulli, Massimo Bernaschi, and Giorgio Parisi. Highly optimized simulations on single-and multi-gpu systems of the 3d ising spin glass model. *Computer Physics Communications*, 196:290–303, 2015.
- [195] Helmut G Katzgraber, LW Lee, and AP Young. Correlation length of the two-dimensional ising spin glass with gaussian interactions. *Physical Review B*, 70(1):014417, 2004.

- [196] Lev Yu Barash, Martin Weigel, Michal Borovský, Wolfhard Janke, and Lev N Shchur. Gpu accelerated population annealing algorithm. *Computer Physics Communications*, 220:341–350, 2017.
- [197] Manoj Kumar, Ravinder Kumar, Martin Weigel, Varsha Banerjee, Wolfhard Janke, and Sanjay Puri. Approximate ground states of the random-field potts model from graph cuts. *Physical Review E*, 97(5):053307, 2018.
- [198] A Peter Young. *Spin glasses and random fields*, volume 12. World Scientific, 1998.
- [199] Yuri Boykov, Olga Veksler, and Ramin Zabih. Fast approximate energy minimization via graph cuts. *IEEE Transactions on pattern analysis and machine intelligence*, 23(11):1222–1239, 2001.
- [200] Martin Weigel and Michel JP Gingras. Ground states and defect energies of the two-dimensional x y spin glass from a quasiexact algorithm. *Physical review letters*, 96(9):097206, 2006.
- [201] Martin Weigel. Genetic embedded matching approach to ground states in continuous-spin systems. *Physical Review E*, 76(6):066706, 2007.
- [202] Scott Kirkpatrick, C Daniel Gelatt, and Mario P Vecchi. Optimization by simulated annealing. *science*, 220(4598):671–680, 1983.
- [203] CJ Geyer et al. Computing science and statistics: Proceedings of the 23rd symposium on the interface. *American Statistical Association, New York*, 156, 1991.
- [204] Koji Hukushima and Koji Nemoto. Exchange monte carlo method and application to spin glass simulations. *Journal of the Physical Society of Japan*, 65(6):1604–1608, 1996.
- [205] Wenlong Wang, Jonathan Machta, and Helmut G Katzgraber. Comparing monte carlo methods for finding ground states of ising spin glasses: Population annealing, simulated annealing, and parallel tempering. *Physical Review E*, 92(1):013303, 2015.
- [206] Jonathan Machta. Population annealing with weighted averages: A monte carlo method for rough free-energy landscapes. *Physical Review E*, 82(2):026704, 2010.
- [207] Michal Borovský, Martin Weigel, Lev Yu Barash, and Milan Žukovič. Gpu-accelerated population annealing algorithm: Frustrated ising antiferromagnet on the stacked triangular lattice. In *EPJ Web of Conferences*, volume 108, page 02016. EDP Sciences, 2016.

- [208] Hamid Khoshbakht and Martin Weigel. Domain-wall excitations in the two-dimensional ising spin glass. *Physical Review B*, 97(6):064410, 2018.
- [209] K Binder. Random-field induced interface widths in ising systems. *Zeitschrift für Physik B Condensed Matter*, 50(4):343–352, 1983.
- [210] ET Seppälä, V Petäjä, and Mikko J Alava. Disorder, order, and domain wall roughening in the two-dimensional random field ising model. *Physical Review E*, 58(5):R5217, 1998.
- [211] Gaurav P Shrivastav, Manoj Kumar, Varsha Banerjee, and Sanjay Puri. Ground-state morphologies in the random-field ising model: Scaling properties and non-porod behavior. *Physical Review E*, 90(3):032140, 2014.
- [212] Efe Ilker and A Nihat Berker. Overfrustrated and underfrustrated spin glasses in  $d=3$  and 2: Evolution of phase diagrams and chaos including spin-glass order in  $d=2$ . *Physical Review E*, 89(4):042139, 2014.
- [213] Jérôme Houdayer and Alexander K Hartmann. Low-temperature behavior of two-dimensional gaussian ising spin glasses. *Physical Review B*, 70(1):014418, 2004.
- [214] Alexander K Hartmann and AP Young. Lower critical dimension of ising spin glasses. *Physical Review B*, 64(18):180404, 2001.
- [215] Alexander K Hartmann and Heiko Rieger. *Optimization algorithms in physics*, volume 2. Wiley-Vch Berlin, 2002.
- [216] Francesco Parisen Toldin, Andrea Pelissetto, and Ettore Vicari. Finite-size scaling in two-dimensional ising spin-glass models. *Phys. Rev. E*, 84:051116, Nov 2011.
- [217] Alexander K Hartmann. No spin-glass transition in the mobile-bond model. *Physical Review B*, 67(21):214404, 2003.
- [218] Francesco Parisen Toldin, Andrea Pelissetto, and Ettore Vicari. Finite-size scaling in two-dimensional ising spin-glass models. *Physical Review E*, 84(5):051116, 2011.
- [219] Oliver Melchert. autoscale. py-a program for automatic finite-size scaling analyses: A user’s guide. *arXiv preprint arXiv:0910.5403*, 2009.
- [220] Francesco Parisen Toldin, Andrea Pelissetto, and Ettore Vicari. Universality of the glassy transitions in the two-dimensional  $\pm j$  ising model. *Phys. Rev. E*, 82:021106, Aug 2010.

- [221] LA Fernandez, E Marinari, V Martin-Mayor, G Parisi, and JJ Ruiz-Lorenzo. Universal critical behavior of the two-dimensional ising spin glass. *Physical Review B*, 94(2):024402, 2016.
- [222] Per-Håkan Lundow and IA Campbell. Ising spin glasses in two dimensions: Universality and nonuniversality. *Physical Review E*, 95(4):042107, 2017.
- [223] Creighton K Thomas, David A Huse, and A Alan Middleton. Zero-and low-temperature behavior of the two-dimensional  $\pm j$  ising spin glass. *Physical review letters*, 107(4):047203, 2011.
- [224] Creighton K Thomas and A Alan Middleton. Numerically exact correlations and sampling in the two-dimensional ising spin glass. *Physical Review E*, 87(4):043303, 2013.
- [225] T. Jörg and F. Krzakala. The nature of the different zero-temperature phases in discrete two-dimensional spin glasses: entropy, universality, chaos and cascades in the renormalization group flow. *J. Stat. Mech. Theor. Exp.*, page L01001, January 2012.